UNIVERSITÀ DEGLI STUDI DI PADOVA

Sede Amministrativa: Università degli Studi di Padova
Dipartimento di Fisica Galileo Galilei

SCUOLA DI DOTTORATO DI RICERCA IN FISICA
CICLO XX

STUDY OF EDGE TURBULENCE IN MAGNETICALLY CONFINED FUSION PLASMAS

Direttore della scuola: Ch.mo Prof. Attilio Stella

Supervisore: Ch.mo Prof. Antonio Buffa

Tutor: Dr. Paolo Scarin

Dottorando: Matteo Agostini

DATA CONSEGNA DELLA TESI
31 Gennaio 2008

Contents

Abstract

Understanding turbulent transport in magnetised plasmas is a subject of great importance for comprehending and optimising experiments and for designing a future fusion rector. In fact turbulence has since long been found to be the dominant reason for the observed limited confinement especially in the edge of fusion devices.

The edge of all fusion experiments, reversed field pinches, tokamaks and stellerators, is characterised by the flow of plasma toward material surfaces and by the outflow of heat and particles from the plasma core through transport. In particular this transport cannot be explained in the framework of classical theory, and understanding its underlying physics remains the outstanding critical issue of thermonuclear fusion physics. Nowadays it is commonly recognised that the main cause of this anomalous transport in the plasma edge is due to turbulence, both electrostatic and magnetic, and many progresses in its understanding have been done experimentally using electrostatic Langmuir probes and optical diagnostics like the gas puff imaging, and theoretically by the development of simulation codes. Experimental measurements have pointed out that most of the outward transport in the edge is due to coherent structures such as blobs ejected from the edge.

In this thesis the characterisation of the edge turbulence in fusion experiments is carried out mainly by means of the optical diagnostic called gas puff imaging (GPI). Also Langmuir probes and fast magnetic pick-up coils are used. I studied the spectral and statistical properties of the turbulent signals, showing their *universal* behaviour independently from the magnetic configuration, indicating that the responsible mechanism should be common. The edge fluctuations are not self similar, i.e. their statistical properties depend on the time scale of the fluctuations themselves.

By comparing the data from the gas puff imaging optical diagnostic and the ones from Langmuir probes, the structure of density-potential blobs is characterised. Then, using the new gas puff imaging diagnostic, through the tomographic algorithm I have developed, I have directly shown the presence in the edge of RFX-mod device of coherent structures propagating along the toroidal direction and responsible for the greatest part of the anomalous transport. The link between these blobs and high frequency magnetic fluctuations can be explained if the edge structures are related to current filaments extending along the magnetic field lines.

Beyond the interaction with the magnetic field, also the link between the edge turbulence and the kinetic pressure is studied, as its gradient is normally considered one of the sources of free energy for the development of the turbulence. I made this studies in particular on the NSTX tokamak, and the results are compatible with the picture of blobs born near the separatrix (in the region of maximum radial gradient of electron pressure) and moving outward while becoming larger

and larger.

In NSTX tokamak, also the relation between the edge turbulence and the transition from L-mode to the better confinement mode (H-mode) has been studied. This transition is always observed to be accompained by the development of a transport barrier in the edge, which is commonly correlated with edge turbulence suppression. With the gas puff imaging diagnostic I observed a drastic reduction in the linear density of edge structures during the transition to the H-mode. Differences between the two plasma regimes are also observed in the perpendicular k-spectrum, which can be interpreted in the L-mode with the presence of an inverse energy cascade toward the small k that is not observed in the H-mode. All these studies highlight the importance of the reduction of the edge turbulence in the development of the edge transport barrier and in the consequent formation of the H-mode.

All the data presented in this thesis have been collected in RFX-mod and TPE-RX reversed field pinch (RFP) experiments and in the NSTX spherical tokamak. RFX-mod is the largest RFP in the world, and operates at Consorzio RFX in Padova, Italy. The device is managed according to an agreement between CNR, ENEA, Euratom, INFN, University of Padova and Acciaierie Venete. RFX-mod began its plasma operation in 2004, after the upgrade of the RFX experiment that operated from 1991 to 1999.
TPE-RX is the Japanese RFP experiment working in the National Institute of Advanced Industrial and Science Technology (AIST) at Tsukuba. The GPI of RFX-mod has been installed in this experiment in 2004, before the plasma operation in RFX-mod.
NSTX is the spherical tokamak operating at the Princeton Plasma Physics Laboratory (PPPL) at Princeton, US. Here I spent 3 months during 2006, analyzing the data collected by the GPI diagnostic.

The thesis is organised as follows:

Chapter 1: Introduces the concepts of plasma and thermonuclear fusion. The MHD equations governing the magnetised plasmas are described in different plasma equilibria. The three devices of this thesis (RFX-mod, TPE-RX and NSTX) are described. A brief introduction on the properties of the plasma edge are given.

Chapter 2: Introduces the main concepts of the turbulence theory. The Navier-Stokes equation and the Kolmogorov theory of the fully developed turbulence are described. A modern approach based on the application of the Renormalisation Group theory to the Navier Stokes is introduced. Then the turbulence theory for magnetised plasmas is described; the concept of *intermittency* is explained with some experimental examples, and a brief description of the electrostatic turbulence and its relation to the main plasma flows is given.

Chapter 3: Is dedicated to the Gas Puff Imaging (GPI) diagnostic. It gives the historical evolution of the optical diagnostic and it describes in detail the three GPI equipments used in the experiments.

Chapter 4: Is dedicated to the mathematical tools used for analysing the data of the turbulent plasma collected by the GPI. In particular the tomographic algorithm developed to obtain a 2 dimensional image of the edge plasma is described, with examples of its applications.

Chapter 5: Describes the main spectral and statistical properties of edge plasma fluctuations. The common characteristics between the three different experiments are pointed out, revealing the universal behaviour of the edge turbulence: in all the devices the non self similar behaviour of the fluctuations is underlined. The size and number of the edge structures are characterised for the two RFPs, and in NSTX the relation between them and the electron pressure is described. A possible driving mechanism for the edge turbulence is studied.

Chapter 6: Describes the interaction of the edge turbulence with the magnetic fluctuations in RFX-mod experiment. The magnetic structure of the edge blobs are investigated, revealing the possibility for them to be linked to filaments of current that flows parallel to the magnetic field.

Chapter 7: Studies the link between the L-H transition in NSTX and the edge structures: in the transition a reduction in the edge turbulent level has been observed, with a possible different energy exchange process between different spatial scales in the two regimes.

Chapter 8: Gives a summary of the results obtained and the conclusions of the thesis.

Riassunto

Capire il trasporto turbolento nei plasmi magnetizzati è un argomento di grande importanza per capire e ottimizzare gli esperimenti per la fusione termonucleare controllata e per la realizzazione di un futuro reattore a fusione. Infatti la turbolenza, specialmente quella che caratterizza il bordo dei plasmi magneticamente confinati, è da lungo tempo considerata la causa dominante delle ridotte proprietà di confinamento osservate.

La regione esterna di tutti gli esperimenti per la fusione controllata, reversed field pinch, tokamak e stellerator, è caratterizata da flussi di plasma verso i materiali della parete e da flussi di particelle e calore dal centro del plasma verso l'esterno attraverso fenomeni di trasporto. In particolare, questo trasporto non può essere spiegato da teorie classiche, e uno dei punti fondamentali e critici nella ricerca sulla fusione termonucleare controllata rimane il capire le cause fisiche di questo trasporto anomalo. Oggi è comunemente riconosciuto che la causa principale del trasporto anomalo nella regione di bordo di un plasma è la turbolenza, sia di natura magnetica che elettrostatica; sono stati fatti molti progressi verso la comprensione di questo fenomeno, sperimentalmente usando sonde elettrostatiche di Langmuir, diagnostiche ottiche come la gas puff imaging e dal punto di vista teorico con lo sviluppo di diversi codici numerici per la simulazione. Misure sperimentali hanno evidenziato che la maggior parte del trasporto radiale nella regione di bordo è dovuto a strutture coerenti, i cosiddetti *blob*.

In questa tesi si caratterizza la turbolenza di bordo degli esperimenti per la fusione termonucleare controllata tramite la diagnostica ottica denominata *gas puff imaging* (GPI). Inoltre sono state utilizzate anche sonde elettrostatiche di Langmuir e sonde magnetiche. Ho analizzato le proprietà spettrali e statistiche dei segnali turbolenti, mostrandone il loro carattere *universale*, e indicando così che il loro meccanismo di generazione potrebbe essere comune. Ho mostrato che le fluttuazioni di bordo non sono autosimili, cioè le loro proprietà statistiche dipendono dalla scala temporale delle fluttuazioni stesse.

Correlando i segnali della diagnostica ottica gas puff imaging con quelli delle sonde di Langmuir, è stato caratterizzato il legame tra densità e potenziale dei blob. Inoltre, attraverso l'algoritmo di inversione tomografica che ho sviluppato per la diagnostica ottica, ho evidenziato la presenza nella regione di bordo di RFX-mod di strutture coerenti che si propagano lungo la direzione toroidale e che sono considerate la causa della maggior parte del trasporto anomalo di particelle. Il legame tra questi blob e le fluttuazioni magnetiche di alta frequenza che ho misurato può essere spiegato se le strutture coerenti sono legate a filamenti di corrente che si estendono lungo le linee di campo magnetico.

Oltre all'interazione con il campo magnetico, si è studiato anche il legame tra le

fluttuazioni di bordo e il profilo radiale della pressione elettronica, dato che il suo gradiente è normalmente considerato una delle fonti di energia libera disponibile per lo sviluppo della turbolenza. Questo tipo di analisi è stata eseguita essenzialmente per l'esperimento NSTX, e i risultati ottenuti sono compatibili con i modelli che prevodono la nascita dei blob nella regione vicino alla separatrice (dove è massimo il gradiente radale di pressione elettronica) e il loro successivo moto verso l'esterno.

Inoltre, nel tokamak NSTX si è studiato il legame tra la turbolenza della regione di bordo e la transizione dal modo L alla configurazione di miglior confinamento (modo H). Questa transizione è sempre accompagnata dalla formazione di una barriera di trasporto al bordo, correlata ad una riduzione della turbolenza. Con la diagnostica gas puff imaging ho misurato una drastica diminuzione della densità lineare di strutture coerenti durante la transizione verso il modo H. Differenze tra i due regimi di plasma sono state evidenziate anche nello spettro dei numeri d'onda k, che nel modo L può essere interpretato con la presenza di una cascata inversa di energia verso i piccoli numeri d'onda che invece non è osservata per il modo H. Tutte queste analisi evidenziano l'importanza della riduzione della turbolenza di bordo per lo sviluppo della barriera di trasporto e la conseguente formazione del modo H.

Tutti i dati presentati nella tesi riguardano gli esperimenti reversed field pinch (RFP) RFX-mod e TPE-RX, e il tokamak sferico NSTX.

RFX-mod è il più grande esperimento RFP nel mondo, e opera presso il Consorzio RFX a Padova, Italia. RFX-mod è gestito da una collaborazione tra CNR, ENEA, Euratom, INFN, Università di Padova e Acciaierie Venete. L'esperimento ha iniziato ad operare con plasma nel 2004, dopo le modifiche apportate al precedente RFX, che ha operato dal 1991 al 1999.
TPE-RX è l'esperimento RFP giapponese, presso il National Institute of Advance Industrial and Science Technology (AIST) a Tsukuba. La GPI utilizzata in RFX-mod è stata installata a TPE-RX nel 2004, prima delle operazioni con plasma in RFX-mod.
NSTX è il tokamak sferico che opera presso i Princeton Plasma Physics Laboratory a Princeton, Stati Uniti. Qui ho trascorso 3 mesi nel 2006, analizzando i dati della GPI.

La tesi è organizzata in questo modo:

Capitolo 1: Vengono introdotti i concetti di plasma e fusione termonucleare; si descrivono le equazioni MHD che governano i plasmi magnetizzati in diversi equilibri e i tre esperimenti analizzati in questa tesi (RFX-mod, TPE-RX, NSTX). Viene data anche una breve introduzione delle proprietà del plasma di bordo.

Capitolo 2: Si introducono i concetti essenziali della teoria dei fluidi turbolenti. Si descrivono le equazioni di Navier-Stokes, la teoria di Kolmogorov per la turbolenza completamente sviluppata e l'applicazione del Gruppo di Rinormalizzazione alla equazione di Navier-Stokes. Si passa quindi alla turbolenza nei plasmi magnetizzati, spiegando il concetto di *intermittenza* anche con

alcuni esempi sperimentali. Alla fine viene data una breve descrizione della turbolenza elettrostatica e della sua relazione con il flusso medio di plasma.

Capitolo 3: È dedicato alla diagnostica gas puff imaging (GPI). Si descrive l'evoluzione storica di questo strumento e vengono dati i dettagli delle tre GPI utilizzate nei diversi esperimenti.

Capitolo 4: È dedicato agli strumenti matematici utilizzati per analizzare la turbolenza misurata con la GPI. In particolare si descrive l'algoritmo di inversione tomografica sviluppato per ottenere una immagine bidimensionale del plasma di bordo e la sua applicazione.

Capitolo 5: Vengono descritte le principali proprietà delle fluttuazioni della regione esterna del plasma. Si sottolineano le caratteristiche comuni tra i tre esperimenti analizzati, rivelando il comportamento universale della turbolenza di bordo: in tutti gli esperimenti si è dimostrata la non autosimilarità delle fluttuazioni. Inoltre si riportano le misure riguardanti dimensioni e numero delle strutture coerenti di bordo per i due esperimenti RFP, e per NSTX si descrive la relazione tra queste e il gradiente radiale di pressione elettronica. Si discute anche un possibile meccanismo di generazione delle strutture.

Capitolo 6: Si descrive l'interazione tra le strutture turbolente e le fluttuazioni di campo magnetico in RFX-mod. Si studia la struttura magnetica dei blob, mostrando come questi siano legati a filamenti di corrente allungati parallelamente alle linee di campo magnetico.

Capitolo 7: Si studia il legame tra la transizione L-H in NSTX e le strutture coerenti: nella transizione si osserva una riduzione dei livelli delle fluttuazioni nel plasma di bordo, con un possibile diverso meccanismo di scambio di energia tra le diverse scale spaziali nei due regimi.

Capitolo 8: Viene dato un riassunto dei principali risultati ottenuti con uno sguardo ai possibili proggetti per futuri lavori.

1

Plasma and thermonuclear fusion

1.1 Introduction

Thermonuclear fusion is the process of union of two nuclei, with the formation of a heavier nucleus and the production of energy. The most attractive fusion reaction that would be used in a reactor is the Deuterium-Tritium one:

$$ {}^{2}_{1}D + {}^{3}_{1}T \rightarrow {}^{4}_{2}He(3.5\text{Mev}) + {}^{1}_{0}n(14.1\text{Mev}) \tag{1.1} $$

This reaction is the most attractive because the cross section is higher with respect to other possible reactions (see fig. 1.1) and so the self-sustained plasma can be realised at the lowest plasma temperature [1, 2]. Deuterium is abundant in nature, instead Tritium can be produced on bombarding Lithium with the neutrons produced by the fusion reaction itself:

$$ {}^{6}_{3}Li + {}^{1}_{0}n \rightarrow {}^{4}_{2}He + {}^{3}_{1}T \tag{1.2} $$

To get a controlled fusion reactor the most promising solution proposes the particle thermal energy to get the sufficient conditions to overcome the Coulomb barrier between the reactants. At these values of temperature matter is in a state of ionised gas. In particular we define the *plasma* as an *ionised gas in globally neutral condition which exhibits collective properties.*

In the next paragraphs the principles of the thermonuclear fusion will be described, together with the Magnetohydrodynamics (MHD) theory. The MHD equilibria will be introduced, describing in particular the Reversed Field Pinch and Tokamak configurations, with three examples of experimental machines. The three experiments are the devices in which edge turbulence has been studied in this thesis.

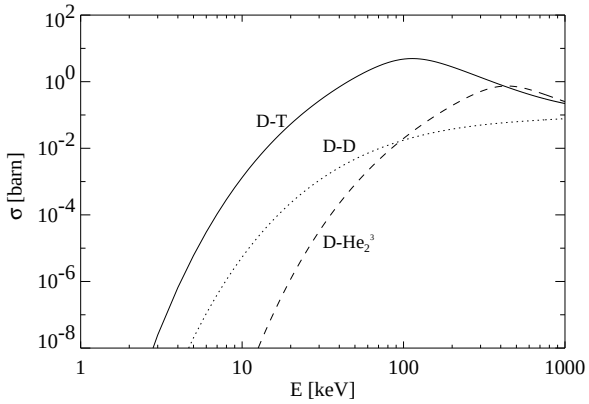

Figure 1.1: *Cross section for three fusion reactions as a function of the energy.*

1.2 Thermonuclear fusion: principles

The goal of the fusion research is to obtain temperature and density of the plasma so that the fusion reaction 1.1 is energetically favorable. From figure 1.1 we observe that the D-T cross section reaches a maximum for energies of order of $80 \div 90\, keV$. Nevertheless, the optimal temperature for fusing nuclei is of about $10\, keV$. The reason resides on properties related to the alpha production rate and on stability limits. Actually it is believed that the power given by alpha particles can be large enough to sustain the reaction, without any external heating. The alpha production rate is given by:

$$\frac{\partial n_\alpha}{\partial t} = n_D n_T \left\langle \sigma_F v \right\rangle \tag{1.3}$$

where n_D and n_T are the density of Deuterium and Tritium respectively, while $\langle \sigma_F v \rangle$ is the fusion reaction rate averaged over velocity distribution. By assuming equal density for the two species, the power of the alpha particle P_α is proportional to the particle fusion reaction energy ε_α, which is:

$$P_\alpha = \frac{1}{4} n^2 \left\langle \sigma_F v \right\rangle \varepsilon_\alpha \tag{1.4}$$

We define now the parameter β:

$$\beta = \frac{p}{B^2/2\mu_0} \tag{1.5}$$

which represents the ratio between the kinetic and magnetic pressure. This parameter gives an indication of the confinement properties.

Introducing equation 1.5 in 1.4 we obtain [3]:

$$P_\alpha = \left(\frac{1}{8\mu_0}\right)^2 \beta^2 B^4 \left[\frac{\langle \sigma_F v \rangle}{T^2}\right] \varepsilon_\alpha \tag{1.6}$$

Since $\langle \sigma_F v \rangle \sim T^2$ for temperature between 8 and 18 keV, P_α has a pronounced flat maximum for $10\, keV$.

In a general fusion reactor there will be a balance between heating and losses, or cooling caused for example by *Bremsstrahlung* radiation:

$$\frac{\partial W}{\partial t} = P_{heat} + P_{\alpha} - P_{loss} \tag{1.7}$$

where the plasma energy density W is given, assuming $n_e \approx n_i$ and $T_e \approx T_i$, by $W \sim 3nT$. Without any heating method, the energy decreases almost exponentially $\frac{\partial W}{\partial t} = -\frac{W}{\tau_E}$ with a characteristic energy confinement time τ_E. The *ignition* condition, defined as the state for which the alpha particle power exceeds the energy losses, gives a condition for the product $n\tau_E$:

$$n\tau_E > \frac{12T}{\varepsilon_{\alpha}} \cdot \frac{1}{\langle \sigma_F v \rangle} \tag{1.8}$$

The product $n\tau_E$ exhibits a minimum at value close to $20\,keV$ so that the ignition condition gives $n\tau_E > 1.5 \cdot 10^{20} m^{-3} s$. Considering the almost constant ratio $\langle \sigma_F v \rangle / T^2$ in the range $8 \div 18\,keV$, a different compact expression to define fusion conditions is the use of the so-called *fusion triple product*:

$$n\tau_E T > 5 \cdot 10^{21} m^{-3}\, s\, keV \tag{1.9}$$

1.3 Thermonuclear fusion: developments

In order to develop a viable fusion reactor that satisfies the triple product condition of eq. 1.9 there are three basic physics requirements which must be satisfied. (1) A sufficient density of plasma mast be (2) confined for a sufficiently long time at (3) a sufficient high temperature to produce net thermonuclear power.

From an oversimplified view of the physics, the problem of maximizing $n\tau_E$ separates into two relatively independent parts. First, the maximum energy confinement time τ_E is determined by the microscopic behaviour of the plasma. This behaviour ultimately leads to macroscopic transport, which can be either classical or anomalous depending on the processes involved. In particular, in all the magnetic devices the neoclassical transport theory predicts electron and ion confinement times up to two orders of magnitude larger than those experimentally measured [4]. Plasma turbulence is probably the major cause of this transport. Therefore, the real problem of understanding anomalous transport (and so to find method to control and reduce it) is understanding plasma turbulence. In experiments, plasma confinement is strongly affected by edge physics, that is an important field of study from years.

Second, the maximum density n is almost always determined, not by microscopic kinetic processes, but rather by macroscopic equilibrium and stability limits set by the magnetic geometry [5].

Actually, a great progress has been made in the understanding of plasma transport that allows a great progress in the thermonuclear experiment performances. In tokamaks, the main line of experimental research in the world program, reactor-level plasma conditions have been achieved (see figure 1.2).

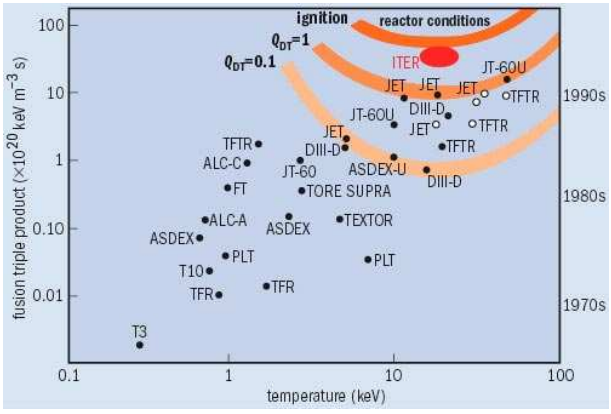

Figure 1.2: *Triple product $n\tau_E T$ obtained in tokamak experiments, showing the great progress obtained during the last years.*

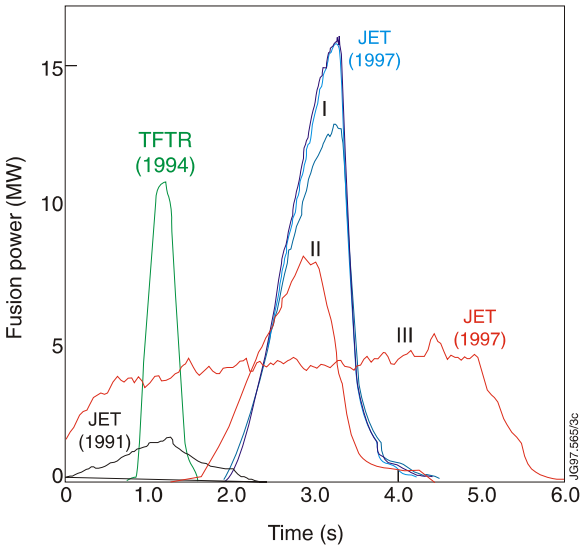

Figure 1.3: *Fusion power produced in D-T experiments in JET and TFTR devices (from ref. [6]).*

Tests with Deuterium-Tritium fuel in JET tokamak led to the generation of 16 MW of fusion power, and of 10 MW in TFTR tokamak [6] (see figure 1.3).

The characteristic time scale of plasma sustainment typical of the 1970s experiments was 1 s. Tokamak and stellerator plasma parameters improved well above those attained in the 70s and have now been sustained for tens of seconds. The development of non-inductive current drive has opened the route to the steady-state operation: the record discharge of Tore Supra tokamak is of 6 min [7] and the small superconducting tokamak TRIAM-1M has been operated for 3 hours and 10 minutes [8].

All these successes with the tokamak configuration has led to the design and construction of ITER (International Thermonuclear Experimental Reactor).[1] ITER

[1]See *www.iter.org* for the latest news about ITER, its design and characteristics.

is designed to demonstrate the scientific and technological feasibility of fusion energy for peaceful purposes. Its operation is expected to produce significant fusion power ($\sim 500\,MW$) through the D-T reaction with high fusion gain $Q \sim 10$ (the ratio between the fusion power and the external heating power) for $3000\,s$ [9]. In other words, the majority of the heating power will be provided by alpha particle heating.

1.4 Magneto Hydro Dynamic description of plasma

The ideal magnetohydrodynamics (MHD) model provides a single-fluid description of long-wavelength, low-frequency, macroscopic plasma behaviour [5, 10, 11]. The equations of ideal MHD are given by:

$$\frac{\partial \rho}{\partial t} + \nabla \cdot (\rho \mathbf{v}) = 0 \tag{1.10}$$

$$\rho \frac{d\mathbf{v}}{dt} = \mathbf{J} \times \mathbf{B} - \nabla p \tag{1.11}$$

$$\frac{d}{dt}(p/\rho^{\gamma}) = 0 \tag{1.12}$$

$$\mathbf{E} + \mathbf{v} \times \mathbf{B} = 0 \tag{1.13}$$

$$\nabla \times \mathbf{E} = -\frac{\partial \mathbf{B}}{\partial t} \tag{1.14}$$

$$\nabla \times \mathbf{B} = \mu_0 \mathbf{J} \tag{1.15}$$

$$\nabla \cdot \mathbf{B} = 0 \tag{1.16}$$

In these equations, the electromagnetic variables are the electric field $\mathbf{E}$, the magnetic field $\mathbf{B}$, and the current density $\mathbf{J}$. The fluid variables are the mass density ρ, the fluid velocity $\mathbf{v}$ and the pressure p. Also $\gamma = 5/3$ is the ratio of specific heats, and $d/dt = \partial/\partial t + \mathbf{v} \cdot \nabla$ is the convective derivative.

Equations 1.14-1.16 indicate that in ideal MHD the electromagnetic behaviour is governed by low-frequency, pre-Maxwell equations. Equations 1.10-1.12 govern the time evolution of mass, momentum and energy respectively. The basic physics of the momentum equation corresponds to that of a fluid with three interacting forces, the pressure gradient force ∇p, the magnetic force $\mathbf{J} \times \mathbf{B}$ and the inertial force $\rho d\mathbf{v}/dt$. The energy equation expresses an adiabatic evolution characterised by a ration of specific heats $\gamma = 5/3$. The remaining equation 1.13 is the Ohm's law, which implies that in a reference frame moving with the plasma the electric field is zero; that is, the plasma is a perfect conductor. In fact it is the perfect-conductivity assumption of Ohm's law that give rise to the name "ideal" MHD.

There are three independent conditions which must be satisfied for ideal MHD to be valid. They are:

1. Small gyroradius;
2. Large collisionality;
3. Small resistivity.

For a fusion plasma with:

$$\begin{aligned} 10^{18} m^{-3} < n < 10^{22} m^{-3} \\ 0.1\, keV < T < 10\, keV \end{aligned} \tag{1.17}$$

the conditions of small gyroradius and small resistivity are well satisfied. However the large collisionality condition is not satisfied [5]. Thus, strictly speaking, the ideal MHD model is not valid for plasma of fusion interest. However there is overwhelming empirical evidence that the ideal MHD provides a rather accurate description of a wide variety of macroscopic plasma behaviour. This happens because in fusion plasmas the magnetic field plays the role of the collision: perpendicular to the field, particles stay in the vicinity of a given magnetic field line if their gyroradius is much smaller than the characteristic plasma length. Consequently, it is appropriate to treat the perpendicular behaviour of the plasma with a fluid model.

1.5 MHD equilibria

The goal of MHD equilibrium theory is the discovery of magnetic geometries which simultaneously

1. Confine and isolate hot plasma from material walls;
2. Have good stability properties at sufficient values of β to be promising for use in potential fusion reactors.

Considering the ideal MHD with $\mathbf{v} = 0$, the MHD equilibrium equations are given by:

$$\mathbf{J} \times \mathbf{B} = \nabla p \tag{1.18}$$

$$\nabla \times \mathbf{B} = \mu_0 \mathbf{J} \tag{1.19}$$

$$\nabla \cdot \mathbf{B} = 0 \tag{1.20}$$

In fusion devices of interest, the magnetic field lines lie in general on a set of closed nested toroidal surfaces. This follows from the equilibrium relation

$$\mathbf{B} \cdot \nabla p = 0 \tag{1.21}$$

The most obvious common geometry in current magnetic fusion concept is *toroidal* (see fig 1.4). The intent is to create a configuration in which magnetic field lines remain contained within the toroidal volume; lines should not intersect the external current-carrying conductors or even the vacuum chamber, which is usually somewhat closer to the plasma.

For well confined equilibria the pressure in most configurations is maximum near the center of poloidal cross section and is approximately constant as a function of toroidal angle (fig. 1.5).

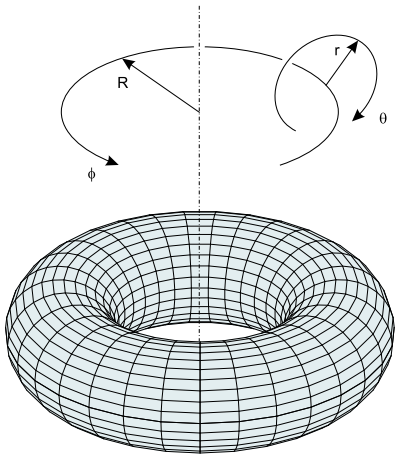

Figure 1.4: *Toroidal geometry for magnetic fusion devices. R: major radius; r:minor radius; θ: poloidal angle; ϕ: toroidal angle.*

For such profiles the contours of constant pressure are nested toroidal surfaces. From equation 1.21 it follows that the magnetic lines lie on the $p = const$ contours, and consequently these contours are usually referred as either magnetic surfaces or flux surfaces. The limiting magnetic surface, which approaches a single magnetic line where the pressure is maximum, is called the magnetic axis.

In the next paragraphs two common toroidal magnetic configurations for fusion experiments are described, the Reversed Field Pinch and the Tokamak.

1.5.1 Reversed Field Pinch configuration

The *Reversed Field Pinch* (RFP) magnetic configuration is a toroidal equilibrium characterised by toroidal and poloidal magnetic field with similar intensity: $B_\theta^2 \sim B_\phi^2$ [5, 12]. The particularity of this configuration is that the toroidal magnetic field at the edge has the opposite sign respect to the center, in order to achieve the stability at high β; the name "reversed" derives from this characteristic. The

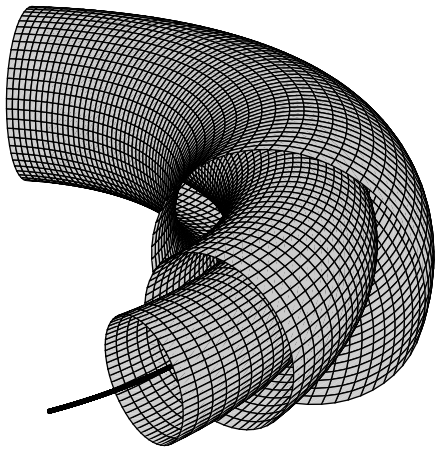

Figure 1.5: *Contours of constant pressure in a well confined toroidal equilibrium.*

radius at which the toroidal field is zero is called *reversal radius*.

In the limit of large aspect ratio (R/a), where a is the minor radius of the torus, and so when the cylindrical approximation can be considered valid, the magnetic fields of a RFP experiment are described by these equations:

$$B_\phi = B_0 J_0(\mu r) \quad B_\theta = B_0 J_1(\mu r) \quad B_r = 0 \tag{1.22}$$

where J_0 and J_1 are the Bessel functions, B_0 is the magnetic field in the axis and μ is a parameter linked to the plasma current and to magnetic field. The theoretical radial profiles of the magnetic fields for this model called *Bessel Function Model* [12] are shown in fig. 1.6.

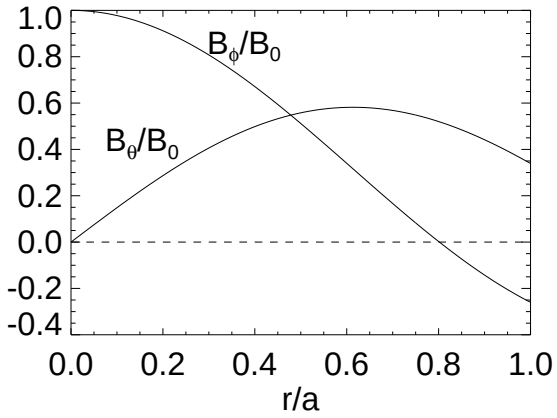

Figure 1.6: *Radial profiles of the toroidal and poloidal magnetic field for a RFP equilibrium in the Bessel function model*

To describe the RFP equilibria, the *reversal parameter* F and the *pinch parameter* Θ are used:

$$F = \frac{B_\phi(a)}{\langle B_\phi \rangle} \quad \Theta = \frac{B_\theta(a)}{\langle B_\phi \rangle} \tag{1.23}$$

In order to have a RFP plasma, the reversal parameter is less then zero.

As example of the RFP configuration, we describe the two devices studied in this thesis: RFX-mod and TPE-RX.

1.5.1.1 RFX-mod experiment

> Rivuoi la scelta, rivuoi il
> controllo, rivoglio le mie ali nere,
> il mio mantello
>
> Afterhours

The RFX-mod (**R**eversed **F**ield e**X**periment modified) is born after the modification of the RFX experiment, at Consorzio RFX, Padova. RFX [13] operated form 1992 to 1999. Then it has been improved and the first plasma of RFX-mod has

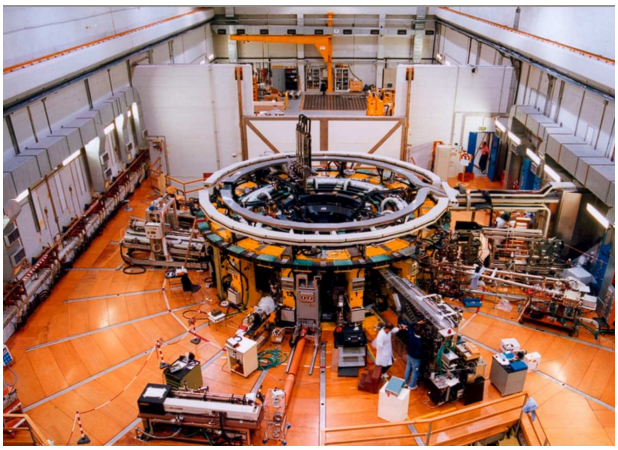

Figure 1.7: *Photograph of the RFX-mod experiment, surrounded by the plasma diagnostics.*

been obtained in 2004. The main characteristic of RFX-mod (fig. 1.7) is reported in table 1.1.

The modifications of RFX [14] were aimed at improving the plasma boundary in terms of both plasma facing components and passive magnetic boundary, and at introducing an active MHD mode control capability [15]. The first set of modifications entails a new conducting shell, which is thin (3 mm Cu) and has one overlapped poloidal gap and one toroidal gap. Newly designed graphite tiles improve plasma-wall interaction by reducing the heat flux peaking on leading edges.

As for the plasma control, RFX-mod is equipped with a full coverage of 192 external saddle coils for MHD control and more flexible power supply for the toroidal field circuit. The saddle coils are arranged in a regular mesh of 48 toroidal $\times$ 4 poloidal stations, each one independently powered.

RFX-mod is also equipped with a great number of diagnostics, to study the behaviour of the plasma. In particular, the plasma edge is well diagnosed with a large set of electrostatic and magnetic probes located inside the Vacuum Vessel (ISIS system [16, 17]), with rectractable Langmuir probes, spectroscopy measurements and the Gas Puff Imaging system described in chapter 3.

RFX-mod	
Major radius	2 m
Minor radius	0.46 m
Plasma current	$<$ 2 MA
Toroidal magnetic field	$<$ 0.7 T
Plasma discharge duration	up to 0.5 s

Table 1.1: *Main parameters of the RFX-mod experiment.*

TPE-RX	
Major radius	1.7 m
Minor radius	0.45 m
Plasma current	< 1 MA
Plasma discharge duration	up to 0.1 s

Table 1.2: *Main parameters of the TPE-RX experiment.*

1.5.1.2 TPE-RX experiment

TPE-RX is a large size RFP machine at AIST, Tsukuba [18, 19]. The main parameters are described in table 1.2, and a photo of the experiment is shown in figure 1.8. The first plasma has been obtained in 1997.

Figure 1.8: *Photograph of the TPE-RX experiment. Unlike RFX-mod, TPE-RX has an iron-core flux swing.*

Unlike RFX-mod, TPE-RX is characterised by an all-metal first wall, with 244 limiters made of Molybdenum which are mushroom shaped.

The plasma edge has been diagnosed by means of the GPI diagnostic and two arrays of Langmuir probes (see section 3.3.1).

1.5.2 Tokamak configuration

Tokamak configuration was proposed by the Russian physicists, Tamm and Sakharov in the year 1952 and realised by Artsimovich. The Tokamak concept is outlined in figure 1.9. The toroidal magnetic field is provided by simple coils and the necessary twist is produced by the plasma itself, by means of the electric current in the plasma which gives rise to the poloidal component of the twisted magnetic field. The current also serves for plasma build-up and heating. This current, as in the case of RFP devices, is produced by induction, the plasma acting as the secondary winding of a transformer. Tokamaks have proved to be very successful in improving the desired fusion plasma conditions and today's best experiments are

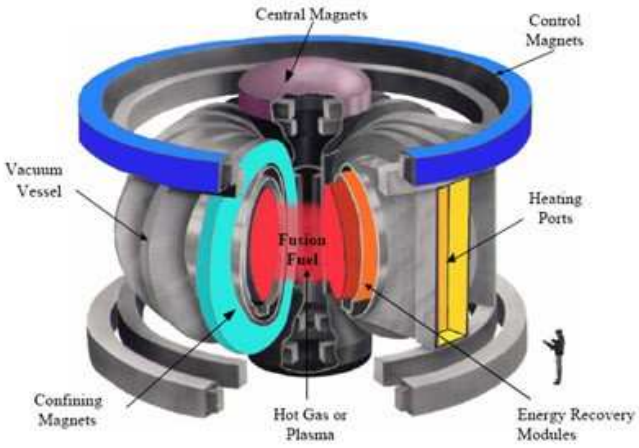

Figure 1.9: *Tokamak concept. The innermost cylindrical coil is the transformer coil for inducing the plasma current. The toroidal coils above and below the machine create a vertical field for plasma shaping an position control.*

based on the tokamak principle. Of course, a transformer can induce the dc plasma current only for a finite time duration; for truely continuous operation, alternative current drive methods are being developed, such us Neutral Beam Injection or plasma-waves interactions.

A complete description of the tokamak configuration and its physics can be found in [1].

1.5.2.1 NSTX experiment

The **N**ational **S**pherical **T**orus E**X**periment (NSTX) is a spherical torus (ST) experiment, i.e. an axis-symmetric toroidal device characterised by a low aspect ratio compared to that of traditional tokamak experiment [20] (see fig. 1.10 for a scheme and a photo of the device). It operates on the Princeton Plasma Physics Laboratory at Princeton, U.S.A., and the first plasma has been obtained in 1999.

The primary factor leading the strong interest in ST configuration is its ability to operate with relatively high ratio of plasma pressure to magnetic field pressure (β) [21]. Since the power density in a fusion reactor is proportional to β^2, a signif-

NSTX	
Major radius	0.85 m
Minor radius	0.65 m
Plasma current	$<$ 1 MA
Toroidal magnetic field	$<$ 0.6 T
Plasma discharge duration	up to 1 s

Table 1.3: *Main parameters of the NSTX spherical torus.*

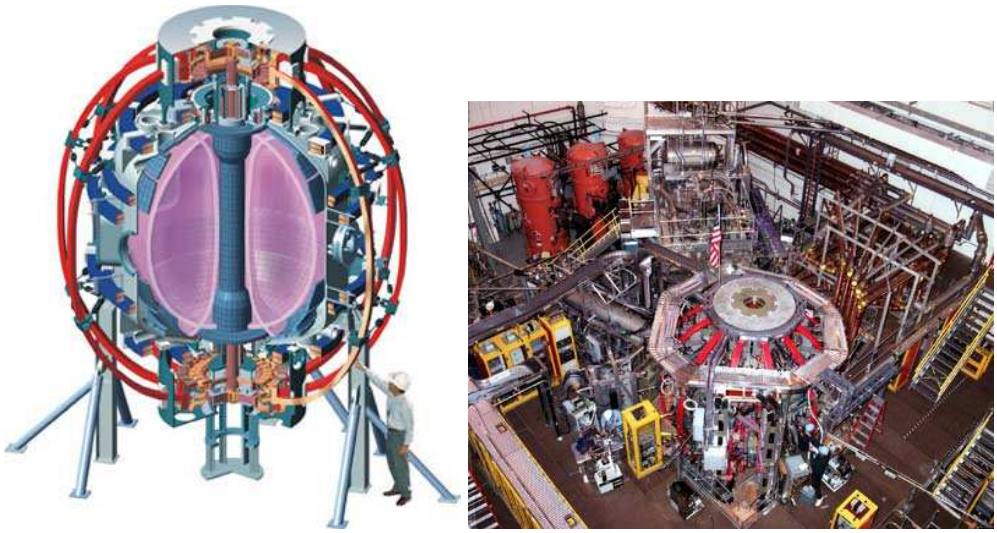

(a) (b)

Figure 1.10: *Scheme (a) and photograph (b) of the NSTX experiment at Princeton Plasma Physics Laboratory.*

icant increase in this factor over that obtainable in high aspect ratio devices could dramatically improve the prospects for realisation of practical magnetic confinement fusion power. The aim of the NSTX experiment is to assess and quantify the physics performance of the ST on a moderate scale and provide a database for the design of future machines based on ST configurations. The principal parameters of NSTX device are reported in table 1.3. Like the nowadays tokamak experiments, rather than the inductive current drive, NSTX is equipped with a neutral beam injector to obtain long non inductive pulses. The first wall facing directly the plasma is made by 3760 individual tiles of graphite and carbon fiber composite, like RFX-mod experiment.

A review of the most recent results in NSTX experiment is reference [22].

1.6 The edge region of fusion experiments

The edge regions in RFP and tokamak experiments have many similarities despite the different magnetic configurations. In all the devices the vacuum vessel is protected by the plasma with limiters (as TPE-RX), divertors (as NSTX) and a full armour of tiles. The last closed flux surface (LCFS) can be defined which separates the scrape-off layer (SOL) from the rest of the plasma. The SOL region, created by limiters or plasma-column displacement reveals properties similar in the two magnetic configurations.

The structure of the edge plasma is characterised essentially by means of Langmuir probes. The plasma potential V_p at the edge of RFPs and tokamaks, measured in different devices, reveals that the radial electric field is directed outward just inside the LCFS and inward in the region near the wall (see [23] and references

cited there). Measurements in RFP experiments have shown that the plasma potential has a minimum in the edge region right inside the LCFS with a potential drop proportional to the local temperature and a halfwidth proportional to the ion Larmor radius [24]. This behaviour close to the LCFS has been interpreted as due to finite Larmor radius (FLR) losses in analogy to some models proposed for tokamaks.

It is known that radial electric fields are the plasma response to intrinsic non-ambipolar transport processes. In particular, parallel transport of electrons in the region inside the reversal surface in the RFPs (a region which is expected to be stochastic to some extent) and perpendicular transport of ions in the edge region due to FLR losses could determine the peculiar structure of the radial electric field at the edge of RFPs.

At the edge the structure of the radial electric field results in a naturally $\mathbf{E} \times \mathbf{B}$ velocity shear layer. In RFP edge the $\mathbf{E} \times \mathbf{B}$ velocity is along the toroidal direction as the main component of the magnetic field is poloidal; instead in tokamak devices the magnetic field is mainly toroidal, with a consequent poloidal $\mathbf{E} \times \mathbf{B}$ velocity. A remarkable feature of the RFP is a second velocity-shear layer occurring where the radial electric field changes sign which has some analogy to the velocity shear layer observed in other devices [24, 25, 26].

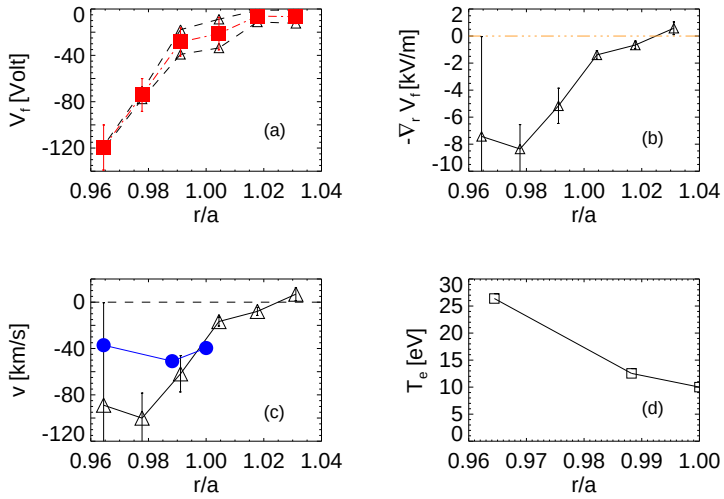

Figure 1.11: *Radial profiles, from TPE-RX of: (a) floating potential V_f; (b) radial gradient of the floating potential; (c) $\mathbf{v}_{\nabla_r V_f \times B}$ drift velocity (triangles) computed from the radial gradient of the floating potential and the poloidal magnetic field B_θ compared with the toroidal velocity $\mathbf{v}_{\phi Lang}$ obtained from cross-correlation (blue circles); (d) deduced electron temperature. From ref. [27].*

In TPE-RX the first measurement of the edge radial profiles of $\mathbf{E} \times \mathbf{B}$ velocity and of the gradient of the electron temperature has been obtained with the Gas Puff Imaging Diagnostic described, developed and used for this PhD thesis, and the results [27] are shown in figure 1.11. In particular, in figure 1.11 (b) and (c) the

first velocity shear layer is clearly detected as reported in the other RFP machines. From these measurements it is difficult to see if there is also the second velocity-shear layer: in fact there is only one radial point beyond the minimum of $\nabla_r V_f$; but the profiles suggest this behaviour also in TPE-RX.

Both in RFP and tokamak machines, the edge has a great importance in the particle and energy transport: transport is mainly fluctuation driven, and these fluctuations contribute a significant fraction to the anomalous radial particle transport in the SOL [28, 29]. It has been found since long time to be the dominant reason for the observed limited confinement, especially in the edge of fusion device.

2

Turbulence and transport: hydrodynamics and magnetohydrodynamics

2.1 Introduction to turbulence

The word *turbulence* is used in everyday experience to indicate something which is not regular. The behaviour of a flow which does not follow the deterministic rules of classical dynamics is called turbulent. Instead, the *laminar* flow is a regular streaming motion.

Turbulence observed in fluid flows appears as a very complicated state of motion, and at first sight it looks strongly irregular and chaotic, both in space and time. The only dynamical rule seems to be the impossibility to predict any future state of the motion. However, it is interesting to recognise that when we take a picture of a turbulent flow at a given time, we see the presence of a lot of different turbulent structures of all sizes which are actively present during the motion. The presence of these structures was well recognised long time ago, as testified by the picture of *vortices* observed and reproduced by Leonardo da Vinci (see fig. 2.1). Turbulence features can be recognised also in atmospheric flow, and one of the best example is the atmosphere of Jupiter, shown in figure 2.2. Today turbulent flows are studied also in superfluids, where quantum turbulence is observed [30]. Even charged fluids can became turbulent, for example laboratory plasmas and the solar wind [31, 32].

Turbulence became an experimental science since Osborne Reynolds who, at the end of XIX century, observed and investigated experimentally the transition from laminar to turbulent flow. He noticed that the flow inside a pipe becomes turbulent every time a single parameter, a combination of the viscosity coefficient ν, a characteristic velocity V and a length L, would increase. This parameter $R_e = VL/\nu$ is called the *Reynolds number*. At lower R_e the flow is regular (laminar), but when R_e increases beyond a certain threshold, the flow becomes turbulent.

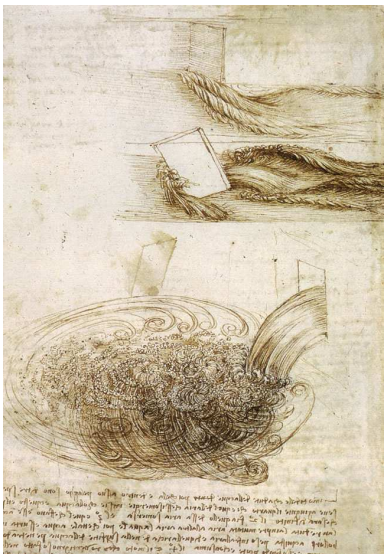

Figure 2.1: *Picture of a turbulent vortex from Leonardo da Vinci's Studies of Water Passing Obstacles and Falling, 1508-09.*

Understanding turbulence is one of the most challenging problems in classical nonlinear dynamics, and the approaches used so far in understanding, describing and modeling it are very interesting even from a historical point of view, as it clearly appears when reading, for example, the references [33, 34]. The characteristics of a turbulent flow are different from the laminar case: turbulence increases the properties of transport in a flow. For example, without atmospheric turbulence, the urban pollution would not spread in a relatively short time. On the other hand, in laboratory plasmas designed to achieved controlled thermonuclear fusion, anomalous transport driven by turbulent fluctuations is the main cause for the degradation of particle confinement [35].

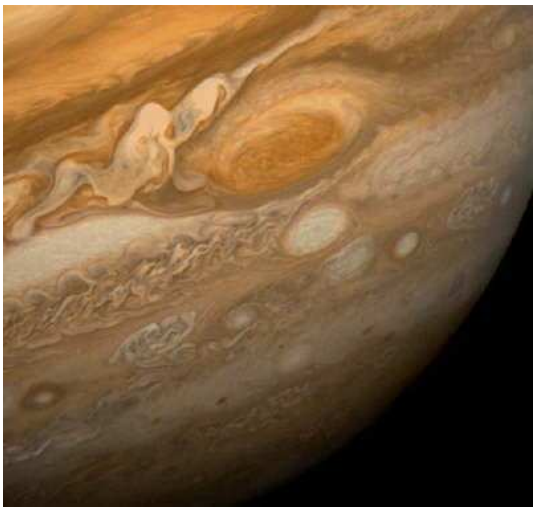

Figure 2.2: *Turbulence in the atmosphere of Jupiter.*

2.2 The Navier-Stokes Equation

Fluids obey the general laws of continuum mechanic: conservation of mass, energy and linear momentum. The equation that describes the fluid is the Navier-Stokes (NS) equation [36]:

$$\rho \left[\frac{\partial \mathbf{v}}{\partial t} + (\mathbf{v} \cdot \nabla)\, \mathbf{v} \right] = -\nabla P + \nu \nabla^2 \mathbf{v} + \mathbf{f} \tag{2.1}$$

where $\mathbf{v}(\mathbf{x}, t)$ is the velocity at the position $\mathbf{x}$ and at time t, P is the pressure, ν is the kinematic viscosity and $\mathbf{f}$ is the external force. If the fluid is incompressible ($\rho = const$) then the conservation of mass gives the divergence free equation:

$$\nabla \cdot \mathbf{v} = 0 \tag{2.2}$$

These two equations describe completely the dynamics of a *viscous, incompressible* and *homogeneous* flow.

The Navier-Stokes equation 2.1 exhibits transition from laminar to turbulent regime as the value of a control parameter, which measures the ratio between the non-linear term $(\mathbf{v} \cdot \nabla)\, \mathbf{v}$ and the linear viscous damping $\nu \nabla^2 \mathbf{v}$, increases. This parameter is the *Reynolds number*:

$$R_e = \frac{|\, (\mathbf{v} \cdot \nabla)\, \mathbf{v}|}{\nu \nabla^2 \mathbf{v}} = \frac{LV}{\nu} \tag{2.3}$$

where L and V are the characteristic length scale and velocity of the fluid. A fluid with low R_e manifests a laminar behaviour and becomes turbulent for higher R_e.

The equation 2.1 satisfies various symmetries [33]:

Space translation: $t,\ \mathbf{x},\ \mathbf{v} \longrightarrow t,\ \mathbf{x} + \mathbf{l},\ \mathbf{v} \qquad \mathbf{l} \in \mathbb{R}^3$

Time translation: $t,\ \mathbf{x},\ \mathbf{v} \longrightarrow t + \tau,\ \mathbf{x},\ \mathbf{v} \qquad \tau \in \mathbb{R}^3$

Galilean transformation: $t,\ \mathbf{x},\ \mathbf{v} \longrightarrow t,\ \mathbf{x},\ \mathbf{v} + \mathbf{u} \qquad \mathbf{u} \in \mathbb{R}^3$

Parity: $t,\ \mathbf{x},\ \mathbf{v} \longrightarrow -t,\ -\mathbf{x},\ -\mathbf{v}$

Rotation[1]***:*** $t,\ \mathbf{x},\ \mathbf{v} \longrightarrow t,\ A\mathbf{x},\ A\mathbf{v} \qquad A \in SO(\mathbb{R}^3)$

Scaling[2]***:*** $t,\ \mathbf{x},\ \mathbf{v} \longrightarrow \lambda^{1-h} t,\ \lambda \mathbf{x},\ \lambda^h \mathbf{v}, \qquad \lambda \in \mathbb{R}^3,\ h \in \mathbb{R}_+$

For the scaling transformations, when t is changed into $\lambda^{1-h} t$, $\mathbf{r}$ into $\lambda \mathbf{r}$, and $\mathbf{v}$ into $\lambda^h \mathbf{v}$, all the terms in the Navier-Stokes equation are multiplied by λ^{2h-1}, except the viscous term, which is multiplied by λ^{h-2}. Thus, for finite viscosity, only $h = -1$ is permitted. The corresponding symmetry is then equivalent to the similarity principle of fluid dynamics, because the scaling transformation are

[1] Only in the limit $L \to \infty$
[2] Only in the limit $\nu = 0$

then seen to keep the Reynolds number unchanged. If we ignore the viscous term ($\nu = 0$, $R_e \to \infty$), then there are infinitely many scaling groups, labeled by their scaling exponent h, which can be any real number.
Increasing the Reynolds number these symmetries tend to be more satisfied. In any case, at very high R_e they are recovered in a statistical meaning: this condition is defined as *fully developed turbulence*.

2.3 Probabilistic description of turbulence

In turbulent fluid the field variables are typically random both in space and time. However statistical averages and probability distribution functions are reproducible in experiments under steady state, and they shed important light on the dynamics of turbulence. Such observations, which have been known for a long time, have induced theoreticians to look for a *probabilistic description* of turbulence. The idea is to use the tools of statistical physics to understand turbulence (for the use of statistical approach to MHD turbulence see [37, 38]).

The statistical description of the turbulent flow starts by dividing the field variables into mean and fluctuating part. Then the averages of various functions of fluctuating fields are computed. There are three types of averages: ensemble, temporal and spatial. Ensemble averages are computed by considering a large number of identical systems and taking averages over all these systems. Temporal averages are computed by measuring the quantity of interest at a point over a long period and then averaging. This make sense for steady state flows. Spatial averages are computed by measuring the quantity at various spatial points at given time, and then averaging. Clearly, spatial averages are meaningful for homogeneous system. Steady state turbulent systems are generally assumed to be *ergodic*, for which the temporal average is equal to the ensemble one [33].

As discussed above, certain symmetries like homogeneity help us in statistical description. Formally, homogeneity indicates that the average properties do not vary with absolute position in a particular direction, but depends only on the separation between points. For example, a homogeneous two-point correlation function is:

$$\langle \mathbf{v}_i(\mathbf{x}) \mathbf{v}_j(\mathbf{x}+\mathbf{r}) \rangle \; = \; C_{ij}(\mathbf{r}) \tag{2.4}$$

Intuitively this property implies that turbulence dynamical properties may be studied scale by scale. Therefore, it is quite convenient to use Fourier basis for the representation of turbulent fields. This is what we will do in the next section.

2.4 Energy cascade

Let us consider homogeneous isotropic turbulent flow within a cubic box of size L with periodic boundary condition. Fluctuating quantities can be Fourier decomposed as:

$$f(\mathbf{x}) = \sum_k \hat{f}(\mathbf{k}) e^{i\mathbf{k}\cdot\mathbf{x}} \qquad \mathbf{k} \in \frac{2\pi}{L}\mathbb{Z}^3 \tag{2.5}$$

where $\hat{f}$ is the Fourier transform of f. Applying the Fourier transform to the equation 2.1, we obtain the Navier-Stokes equation in Fourier space [36]:

$$\left(\frac{\partial}{\partial t} + \nu k^2\right) \hat{v}_i(\mathbf{k}, t) = -ik_m D_{ij} \int_{\mathbf{p}+\mathbf{q}=\mathbf{k}} \hat{v}_j(\mathbf{p}, t)\hat{v}_j(\mathbf{q}, t)d\mathbf{p} + \hat{f}_i(\mathbf{k}) \tag{2.6}$$

where

$$D_{ij} = \delta_{ij} - \frac{k_i k_j}{k^2} \tag{2.7}$$

and δ_{ij} is the Kronecker delta.
The first term on the right hand side of eq. 2.6 represents the non-linear interactions between the three wave vector such that $\mathbf{k} = \mathbf{p} + \mathbf{q}$. An analysis of the coupling term $k_m D_{ij}$ shows that the local interaction with $\mathbf{k} \sim \mathbf{p} \sim \mathbf{q}$ are the most relevant in the integration [39].

Now it is possible to show that the nonlinear term redistributes energy among the various scales of motion without affecting the global energy budget.
We can define the *total kinetic energy*:

$$E(t) = \frac{1}{2} \langle \mathbf{v}(\mathbf{x}, t) \cdot \mathbf{v}(\mathbf{x}, t) \rangle \tag{2.8}$$

If isotropy and homogeneity conditions are satisfied kinetic energy may be written as:

$$E(t) = \int_0^{+\infty} k^2 E(k, t)dk \tag{2.9}$$

where $E(k, t)$ is the spectral energy.
From the N.S. equation in Fourier space (eq. 2.6), the balance equation for the temporal evolution of kinetic energy E can be derived [36]:

$$\left(\frac{\partial}{\partial t} + 2\nu k^2\right) E(k, t) = F(k, t) + T(k, t) \tag{2.10}$$

This equation expresses the balance between $F(k, t)$, that is the input energy per unit time on the wave vector k, $T(k, t)$ that is the net transfer of energy on k due to the nonlinear term, and the dissipation $2\nu k^2 E(k, t)$. Then the kinetic-energy flux through wave number k is consequently defined as:

$$\Pi(k, t) = \int_k^{+\infty} T(k', t)dk' \tag{2.11}$$

and it can be demonstrated that [36]:

$$\int_0^{+\infty} T(k', t)dk' = 0 \tag{2.12}$$

Actually a forcing term necessarily introduces inhomogeneities: we can assume that the term $F(k, t)$ is not zero only for wave vector $k_0 = 1/L$ that is the input energy scale. As high wave number are dynamically separated from small ones, turbulence at small scales results isotropic and homogeneous. From this consideration another important result can be derived. Let us consider a stationary solution of equation 2.10:

$$2\nu k^2 E(k) = T(k) + F(k) \tag{2.13}$$

for $k \neq k_0$ we obtain:

$$T(k) = 2\nu k^2 E(k) \tag{2.14}$$

so that at fixed value of k, $lim_{\nu \to 0} T(k) = 0$. Defining the *input energy rate* ε:

$$\varepsilon = \int_0^{+\infty} F(k) dk \tag{2.15}$$

and by integrating equation 2.13 from 0 to $+\infty$ and using eq. 2.12, we obtain:

$$\varepsilon = 2\nu \int_0^{+\infty} k^2 E(k) dk \tag{2.16}$$

This equation shows that the kinetic energy is balanced by fluid viscosity. Finally integration of equation 2.13 from 0 to $k \neq k_0$ yields [36]:

$$\begin{aligned} \lim_{\nu \to 0} \Pi(k) &= 0 \quad k < k_0 \\ \lim_{\nu \to 0} \Pi(k) &= \varepsilon \quad k > k_0 \end{aligned} \tag{2.17}$$

The very simple but important conclusion is the exists a spectral range extending beyond the injection range where at vanishing viscosity the kinetic energy transfer is identically zero and the energy flux is constant and equal to the injection rate. For this reason the subsequent spectral ranges may be identified:

- **Input energy range:** $k \ll k_0 \approx 1/L$;
- **Inertial range:** $k_0 \ll k \ll k_d$ (k_d is the dissipative wave vector) where the energy is mainly transferred toward higher wave number without production or dissipation;
- **Dissipative range:** $k > k_d$ where energy is dissipated.

This is the *Richardson cascade* [40, 41], schematically reproduced in figure 2.3 and summarised by Richardson's words: "*Big whorls have little whorls, which feed on their velocity; and little whorls have lesser whorls, and so on to viscosity*".

An ordinary turbulent fluid is made up of vortices of different size: energy enters the system from the injection scale k_0 feeding big eddies; then it flows without dissipation toward smaller scales (inertial scale) up to the dissipation scale where it is dissipated by the viscosity.
These results are the major ingredients of the Kolmogorov theory.

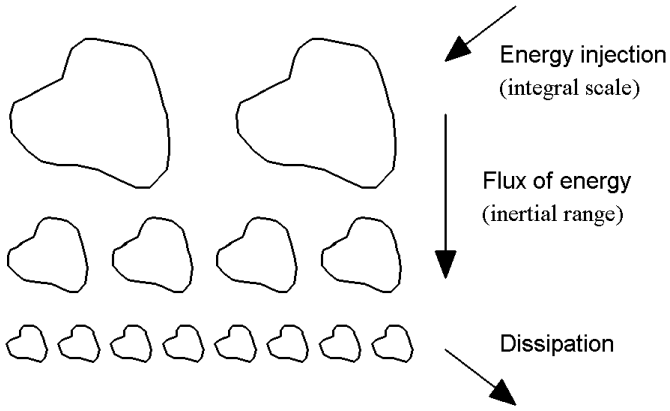

Figure 2.3: *The Richardson energy cascade. The energy is injected in the injection range feeding big eddies; then it flows toward smaller ones up to the dissipation range where it is dissipated by the viscosity.*

2.5 The Kolmogorov K41 theory

The turbulence theory developed in 1941 by Kolmogorov (K41 theory) [42, 43] is certainly one of the most famous theories of isotropic turbulence. We have just seen that for stationary isotropic turbulence forced at a rate ε in a narrow spectral range around k_0, and in the limit of infinite Reynolds number, the energy flux $\Pi(k)$ is independent from k and equal to ε for $k > k_0$, ε being also the dissipation rate. This shows that ε is an extremely important parameter which controls the energy flux from the large scales where it is injected to the small ones where it is dissipated by viscosity: this is the scheme of the Richardson cascade previously described.

Starting from this phenomenology, Kolmogorov makes two assumptions:

- **First hypothesis of similarity:** At very high, but not infinite Reynolds number, all the small-scale statistical properties are uniquely and universally determined by the scale l, the mean energy dissipation rate ε and the viscosity ν;
- **Second hypothesis of similarity:** In the limit of infinite Reynolds number, or equivalently in the inertial range where dissipation is negligible, all the small-scale statistical properties are uniquely and universally determined by the scale l and the energy dissipation rate ε.

By adopting this phenomenological point of view the typical life time of an eddy in the inertial range can be estimated as:

$$\tau_l \approx \frac{l}{\delta v_l} \tag{2.18}$$

where $\delta v_l = v(x + l) - v(x)$ is the typical fluctuation of the velocity field at scale l. The time τ_l is often referred to as *eddy turnover time*, and corresponds to

the time necessary to transfer the energy δv^2. As a consequence, the energy flux can be written as:

$$\varepsilon = \frac{\delta v_l^2}{\tau_l} \approx \frac{\delta v_l^3}{l} \tag{2.19}$$

From the above relations the expression for the energy spectrum can be obtained:

$$\begin{aligned} \left\langle |\delta v_l^2| \right\rangle &\sim (\varepsilon l)^{2/3} \sim kE(k) \\ E(k) &\approx C_K \varepsilon^{2/3} k^{-5/3} \end{aligned} \tag{2.20}$$

This is the famous power-law for the energy spectrum of the fluid turbulence, the so-called "$-5/3\,law$" (see also [44]).

The inertial range of the spectrum is limited by dissipation phenomena, and the highest wave number of the inertial range $k = k_d$ can be estimated as [33]:

$$k_d = \left(\frac{\varepsilon}{\nu^3}\right)^{1/4} \tag{2.21}$$

Finally we want to demonstrate that under Kolmogorov's assumptions equation 2.19 is valid in all the turbulent fluids. As previously mentioned the existence of self-similar solutions is a direct consequence of the scale invariance of the Navier-Stokes equation. For instance, by assuming the scale transformation:

$$\begin{aligned} l &\to l' = \lambda l \\ \mathbf{v} &\to \mathbf{v}' = \lambda^h \mathbf{v} \\ P &\to P' = \lambda^\chi P \\ \rho &\to \rho' = \lambda^\mu \rho \\ t &\to t' = \lambda^{1-h} t \end{aligned} \tag{2.22}$$

it is possible to write eq. 2.1 for the re-scaled variables:

$$\lambda^{-\mu} \lambda^{1-2h} \rho' \left[\frac{\partial \mathbf{v}'}{\partial t} + (\mathbf{v}' \cdot \nabla') \mathbf{v}' \right] = -\nabla' P' \lambda^{1-\chi} \tag{2.23}$$

Scaling transformation invariance requires that:

$$1 - 2h - \mu = 1 - \chi \tag{2.24}$$

Taking into account incompressibility condition ($\mu = 0$) the previous equation needs $\chi = 2h$. The Kolmogorov's hypothesis of constant energy flux fixes without ambiguity the value of h. The scale variation of energy flux is written:

$$\varepsilon \to \varepsilon' = \lambda^{3h-1} \varepsilon \tag{2.25}$$

so that $\varepsilon = cost$ causes h to be identically equal to $1/3$. Consequently $\frac{\delta v_l}{l^{1/3}}$ is a motion invariant and equation 2.19 is valid in all the turbulent fluid.

2.6 The Renormalisation Group in fluid turbulence

There are a number of problems in science which have, as a common characteristic, that complex microscopic behaviour underlies macroscopic effects. In simple cases the microscopic fluctuations average out when larger scales are considered, and the averaged quantities satisfy classical continuum equations. Unfortunately there is a much more difficult class of problems where fluctuations persist out to macroscopic wavelengths, and fluctuations on all intermediate length scales are important too.

In this last category are the problems of critical phenomena, elementary particle physics and of fully developed turbulence.

In fully developed turbulence of atmosphere, global air circulation becomes unstable, leading to eddies on a scale of thousands of kilometers. These eddies break down (like the Richardsons cascade) into smaller eddies, which in turn break down, until chaotic motions on all length scales down to millimeters have been excited.

The *Renormalisation Group* (RG) approach is a strategy for dealing with problems involving many length scales [45, 46, 47]. The strategy is to tackle the problem in steps, one step for each scale. In case of critical phenomena, the problem, technically, is to carried out statistical averages over thermal fluctuations on all size scales. The RG approach consists in integrating out the fluctuations in sequence, starting with fluctuations on atomic scales until fluctuations on all scales have been averaged out.

In this section we apply the RG method to the Navier Stokes equation, obtaining the energy spectrum of the fully developed turbulence following the reference [48].

2.6.1 Formulation of the problem

The application of the RG theory to the Navier Stokes equations to study the turbulence is linked with the presence of the Richardson cascades: as previously seen, in turbulent fluids there is a hierarchy of scales that interact which each other. Here we will show that with the application of the RG theory the energy spectrum of the turbulence can be recovered, and in particular the power law decay (Kolmogorov spectrum). We'll describe the *Forster-Nelson-Stephen* (FNS) theory [48], that is one of the first application of the Renormalisation Group to the NS equations.

Let us re-write the NS equation 2.1 in this way:

$$\left(\frac{\partial}{\partial t} - \nu\nabla^2\right) v_\alpha = -\frac{\partial P}{\partial x_\alpha} - \frac{\partial v_\alpha v_\beta}{\partial x_\beta} + f_\alpha$$
$$\frac{\partial v_\alpha}{\partial x_\alpha} = 0 \tag{2.26}$$

By expanding the velocity in time and space:

$$v_\alpha(\mathbf{x}, t) = \sum_{\mathbf{k}} \sum_{\omega} v_\alpha(\mathbf{k}, \omega) \exp\left(i\mathbf{k}\cdot\mathbf{x} + i\omega t\right) \tag{2.27}$$

and substituting in the previous equation, we obtain [39]:

$$(i\omega + \nu k^2)v_\alpha(\mathbf{k},\omega) = \lambda M_{\alpha\beta\gamma}(\mathbf{k}) \sum_j \sum_{\omega'} v_\beta(\mathbf{j},\omega')v_\gamma(\mathbf{k}-\mathbf{j},\omega-\omega') + \\ + D_{\alpha\beta}(\mathbf{k})f_\beta(\mathbf{k},\omega) \tag{2.28}$$

where λ is the parameter that weighs the non-linear term of the equation. The other terms are defined:

$$D_{\alpha\beta}(\mathbf{k}) = \delta_{\alpha\beta} - \frac{k_\alpha k_\beta}{|\mathbf{k}|^2} \tag{2.29}$$

$$M_{\alpha\beta\gamma}(\mathbf{k}) = \frac{1}{2i}\left(k_\alpha D_{\alpha\gamma}(\mathbf{k}) + k_\gamma D_{\alpha\beta}(\mathbf{k})\right) \tag{2.30}$$

The solution of equation 2.28 without the non-linear term is the velocity field at zero order [39]:

$$v_\alpha^{(0)}(\mathbf{k},\omega) = D_{\alpha\beta}(\mathbf{k})G_0(k,\omega)f_\beta(\mathbf{k},\omega) \tag{2.31}$$

where $G_0(\mathbf{k},\omega)$ is the zero-order propagator:

$$G_0(\mathbf{k},\omega) = \frac{1}{i\omega + \nu k^2} \tag{2.32}$$

Then the perturbation expansion of the velocity can be defined as:

$$v_\alpha(\mathbf{k},\omega) = v_\alpha^0(\mathbf{k},\omega) + \lambda v_\alpha^1(\mathbf{k},\omega) + \lambda^2 v_\alpha^2(\mathbf{k},\omega) + \cdots \tag{2.33}$$

2.6.2 Perturbation theory

The FNS theory is developed in a d-dimensional space. A maximum wavevector Λ is defined (ultra violet cut off), very much smaller than the dissipation wavenumber. This means that the Fourier decomposition of the velocity field in the wavenumber-frequency domain, as given by equation 2.27 should be written as:

$$v_\alpha(\mathbf{k},t) = \left(\frac{1}{2\pi}\right)^{d+1} \int_{k\le\Lambda} d^d k \int d\omega\, v_\alpha(\mathbf{k},\omega)\exp\left(i\mathbf{k}\cdot\mathbf{x} + i\omega t\right) \tag{2.34}$$

Similarly, the equation of motion 2.28 should be modified to:

$$(i\omega + \nu_0 k^2)v_\alpha(\mathbf{k},\omega) = D_{\alpha\beta}(\mathbf{k})f_\beta(\mathbf{k},\omega) + \\ + \lambda_0 M_{\alpha\beta\gamma}(\mathbf{k}) \int_{j\le\Lambda} d^d j \int d\Omega\, u_\beta(\mathbf{j},\Omega)u_\gamma(\mathbf{k}-\mathbf{j},\omega-\Omega) \tag{2.35}$$

where ν_0 is the unrenormalised viscosity and λ_0 is the unrenormalised expansion parameter. The stirring force is specified by its autocorrelation:

$$\langle f_\alpha(\mathbf{k},\omega) f_\beta(\mathbf{k}',\omega')\rangle = 2W(k)(2\pi)^{d+1} D_{\alpha\beta}(\mathbf{k})\delta(\mathbf{k}+\mathbf{k}')\delta(\omega+\omega') \tag{2.36}$$

where $W(k)$ is a measure of the rate at which the stirring force does work on the fluid. A power law form of $W(k)$ is assumed:

$$W(k) = W_0 k^{-y} \tag{2.37}$$

Now we divide up the velocities into low-frequency and high-frequency parts as follows:

$$v_\alpha(\mathbf{k},\omega) = \begin{cases} v_\alpha^<(\mathbf{k},\omega) & 0 < k < \Lambda\exp(-l) \\ v_\alpha^>(\mathbf{k},\omega) & \Lambda\exp(-l) < k < \Lambda \end{cases} \tag{2.38}$$

and the same for the stirring force.

The corresponding decomposition of the NS equation can be obtained by substituting 2.38 and the correspondent for the stirring force into equation 2.35:

$$\begin{aligned} (i\omega + \nu_0 k^2) v_\alpha^<(\mathbf{k},\omega) = \\ = f_\alpha^<(\mathbf{k},\omega) + \lambda_0 M^<_{\alpha\beta\gamma}(\mathbf{k}) \int_{j\le\Lambda} d^d j \int d\Omega \{ v_\beta^<(\mathbf{j},\Omega) v_\gamma^<(\mathbf{k}-\mathbf{j},\omega-\Omega) + \\ 2 v_\beta^<(\mathbf{k}-\mathbf{j},\omega-\Omega) + v_\beta^>(\mathbf{j},\Omega) v_\gamma^>(\mathbf{k}-\mathbf{j},\omega-\Omega)\} \end{aligned} \tag{2.39}$$

and the similar one for $v_\alpha^>$.

Then the zero order velocity field can be written as:

$$v_0^>(k) = G_0(k) f^>(k) \tag{2.40}$$

and the associated perturbation expansion is:

$$v^>(k) = v_0^>(k) + \lambda_0 v_1^>(k) + \lambda_0^2 v_2^>(k) + \cdots \tag{2.41}$$

Now the expansion of the velocity field 2.41 is substituted in equations 2.39 and then we average out the effect of the high frequencies. The final result is this equation (see ref. [39]):

$$\begin{aligned} \{ i\omega + \nu_0 k^2 + \Delta\nu_0(k) k^2 \} v_\alpha^<(\mathbf{k},\omega) = \\ = f_\alpha^<(\mathbf{k},\omega) + \lambda_0 M^<_{\alpha\beta\gamma}(\mathbf{k}) \int_{j\le\Lambda} d^d j \int d\Omega v_\beta^<(\mathbf{j},\Omega) v_\gamma^<(\mathbf{k}-\mathbf{j},\omega-\Omega) \end{aligned} \tag{2.42}$$

This equation is identical to the non rescaled NS equation, but now it is defined only in $0 < k < \Lambda e^{-l}$ as we averaged out the small scales, with the *re-scaled viscosity* $\nu_1 = \nu_0 + \Delta\nu_0(k)$. To obtain the value of $\Delta\nu_0(k)$ we have to compare the rescaled and not rescaled NS equation, taking the limits $\omega \to 0$ and $k \to 0$ and integrating in the space of the wavevector. The result is:

$$\Delta\nu_0(0) = \frac{K(d)\lambda_0^2 W_0 \exp(\epsilon l) - 1}{\nu_0^2 \lambda^\epsilon \epsilon} \tag{2.43}$$

where:

$$\epsilon = 4 + y - d \tag{2.44}$$

$$K(d) = \frac{A(d)S_d}{(2\pi)^d} \tag{2.45}$$

$$A(d) = \frac{d^2 - d - \epsilon}{2d(d+2)} \tag{2.46}$$

and S_d is the volume of a sphere in d-dimension:

$$S_d = \frac{2\pi^{d/2}}{\Gamma(d/2)} \tag{2.47}$$

Thus the total viscosity ν_1 after the elimination of the modes in the band $\Lambda \exp(-l) < k < \Lambda$ is given by:

$$\nu_1 = \nu_0 + \Delta\nu_0(0) = \nu_0 \left\{ 1 + K(d)\bar{\lambda_0^2} \frac{\exp(\epsilon l) - 1}{\epsilon} \right\} \tag{2.48}$$

where the modified strength parameter $\bar{\lambda_0}$ is given by:

$$\bar{\lambda_0} = \frac{\lambda_0 W_0^{1/2}}{\nu_0^{3/2} \Lambda^{\epsilon/2}} \tag{2.49}$$

This last step highlights the fact that this is a different way of performing perturbation theory. In renormalised perturbation theory λ plays the part of a bookkeeping parameter. The procedure there was to sum certain classes of terms to all orders and then put $\lambda = 1$ at the end of the calculation. Here, however, the strength parameter becomes renormalised, as a consequence of the viscosity's being renormalised. And the process leading to this is the combination of the iteration with rescaling.

2.6.3 Recursion relation

The aim is now to make eq. 2.42 look as much as possible like the original Navier-Stokes equation. We do this by scaling all the variables of the problem. For instance, in eq. 2.42 the wavenumber k is now defined in the interval $0 < k < \Lambda \exp(-l)$. If we divide k by the scaling factor $\exp(-l)$, then we obtain a new variable which is defined on the original interval. Thus we introduce

$$\tilde{k} = k \exp(l) \tag{2.50}$$

where $\tilde{k}$ is defined now on $0 < \tilde{k} < \Lambda$. Accordingly, we introduce the more general scaling:

$$\begin{aligned} \tilde{\omega} &= \omega \exp\{a(l)\} \\ \tilde{v} &= v \exp\{-c(l)\} \end{aligned} \tag{2.51}$$

where $a(l)$ and $c(l)$ are to be determined.

With these considerations in mind, eq. 2.42 can be rewritten with the replacement $\nu_1 = \nu_0 + \Delta\nu_0$ and using the rescaled variables. The stirring force, viscosity and strength parameter must then satisfy the following relationship:

$$\begin{aligned} \tilde{f}_\alpha(\tilde{\mathbf{k}}, \omega) &= f_\alpha^<(\mathbf{k}, \omega) \exp(a - c) \\ \nu(l) &= \nu_0 \exp(a - 2l) \\ \lambda(l) &= \lambda_0 \exp\{c - (d+1)l\} \end{aligned} \tag{2.52}$$

Now, to evaluate the two parameters $a(l)$ and $c(l)$ we substitute in the equation for the stirring force 2.36 the rescaled variables, obtaining:

$$2c = a + l(y - d) \tag{2.53}$$

Forster *et. al* [48] carried out their iteration using infinitesimal wavenumber bands at each step. This means that the recursion relations can be turned into differential equations with l as a continuous independent variable. At the end these differential equations are obtained:

$$\begin{aligned} \frac{d\nu}{dl} &= \nu(l)\{z - 2 + K(d)\bar{\lambda}^2\} \\ \frac{dW_0}{dl} &= 0 \\ \frac{d\lambda}{dl} &= \lambda(l)\left(\frac{3z}{2} - 1 - \frac{d-y}{2}\right) \end{aligned} \tag{2.54}$$

where z is defined by:

$$z = \frac{da}{dl} \tag{2.55}$$

Also, by an obvious analogy with equation 2.49, the modified strength parameter $\bar{\lambda}$ is defined as:

$$\bar{\lambda}^2 = \frac{\lambda^2 W_0}{\nu^3 \Lambda^\epsilon} \tag{2.56}$$

The recursion relation for $\bar{\lambda}$ can be obtained from equations 2.54, and takes the form:

$$\frac{d\bar{\lambda}}{dl} = \frac{\bar{\lambda}}{2}\{\epsilon - 3K(d)\bar{\lambda}^2\} \tag{2.57}$$

2.6.4 Behaviour near the fixed point

Equation 2.57 is one of the most important result of the FNS treatment, as it shows how the strength parameter rescales.

For $\epsilon > 0$, $\bar{\lambda}$ tends to a fixed point $\bar{\lambda}^*$, and we want to study what happens in proximity of this fixed point.

The fixed point of the transformation is:

$$\bar{\lambda}^* = \left\{ \frac{\epsilon}{3K(d)} \right\}^{1/2} \tag{2.58}$$

as $l \to \infty$. In particular we would like to obtain the energy spectrum near $\bar{\lambda}^*$. It can be defined as [48]:

$$E(k) = \left(\frac{1}{2} \frac{S_d}{(2\pi)^{d-1}} \right) k^{d-1} \int_{-\infty}^{+\infty} Tr G_{ij}(\mathbf{k}, \omega) d\omega \tag{2.59}$$

where G_{ij} is the velocity-velocity correlation function:

$$G_{ij} = \frac{\langle v_i(\mathbf{k}, \omega) v_j(\mathbf{k}', \omega') \rangle}{(2\pi)^{d+1} \delta(\mathbf{k} + \mathbf{k}') \delta(\omega - \omega')} \tag{2.60}$$

Introducing the different scaling law in this equation, we obtain that:

$$G_{ij} \sim e^{-2c-dl-a} \tag{2.61}$$

and so, as $E(k) \sim k^{d-1} G_{ij} \omega$:

$$E(k) \sim e^{(d-1)l} e^{-2c-ld-a} e^{a} \tag{2.62}$$

Remembering that $2c = a - ly - ld$, $z = 2 - \frac{4+y-d}{3}$ and that $da = z(l)dl$, integrating this last equation we obtain for the energy spectrum:

$$E(k) \sim k^{-5/3+(2/3)(d-y)} \tag{2.63}$$

For $d = y$ we obtain the Kolomgorov spectrum.

2.7 MHD turbulence

A theory similar to the Kolmogorov one have been developed for MHD fluids and it will be reviewed in this section.

We have seen that nonmagnetic fluids are known to become turbulent at sufficiently high Reynolds number: similarly plasmas, as electrically conducting magnetised fluids, are expected to become turbulent at increasing value of *magnetic Reynolds number* $R_m = \frac{Lv}{\lambda}$, where $\lambda = \frac{\nu}{\mu_0}$ is the resistive coefficient and v is the fluid velocity.
The MHD equations, in the incompressible case, can be written in terms of the *Elsässer variables* $\mathbf{z}^{\pm} = \mathbf{v} \pm \mathbf{v}_A = \mathbf{v} \pm \mathbf{B}/\sqrt{\mu_0 \rho}$ [49], as a unique equation which is formally similar to the Navier-Stokes one [50]:

$$\begin{aligned} \frac{\partial \mathbf{z}^{\pm}}{\partial t} \mp (\mathbf{v}_A \cdot \nabla)\mathbf{z}^{\pm} + (\mathbf{z}^{\mp} \cdot \nabla)\mathbf{z}^{\pm} = \\ = -\nabla(P + B^2/2) + \frac{\nu + \lambda}{2} \nabla^2 \mathbf{z}^{\pm} + \frac{\nu - \lambda}{2} \nabla^2 \mathbf{z}^{\pm} \end{aligned} \tag{2.64}$$

where $\mathbf{v}_A$ is the *Alfvén velocity*. Equation 2.64 indicates that small scale turbulence may be considered as an ensemble of Alfvén waves propagating along the average

field $\mathbf{B}_0$ with interactions occurring only between modes traveling in opposite directions.

In the ideal ($\nu = 0$) 3D MHD there are three invariants [50]:

$$\begin{aligned} E = \frac{1}{2}\int (v^2 + B^2)\, d^3x = \frac{1}{2}\sum_{\mathbf{k}} (|v_{\mathbf{k}}|^2 + |B_{\mathbf{k}}|^2) \qquad &= \\ = E^V + E^M \qquad &\text{Total Energy} \\ K = \frac{1}{2}\int \mathbf{v}\cdot B\, d^3x = \frac{1}{2}\sum_{\mathbf{k}} \mathbf{v}_{\mathbf{k}}\cdot\mathbf{B}_{-\mathbf{k}} \qquad &\text{Cross helicity} \\ H = \frac{1}{2}\int \mathbf{A}\cdot\mathbf{B}\, d^3x = \frac{1}{2}\sum_{\mathbf{k}} \mathbf{A}_{\mathbf{k}}\cdot\mathbf{B}_{-\mathbf{k}} \qquad &\text{Magnetic helicity} \end{aligned} \tag{2.65}$$

Our porpouse is to show the existence of a scaling law for the energy spectrum also in MHD turbulence, quite similar to what found in ordinary fluid.

The first two equations of 2.65 correspond to the conservation of the *pseudo energies*:

$$E^{\pm}(t) = \frac{1}{2V}\int |\mathbf{z}^{\pm}(\mathbf{r},t)|^2\, d^3x \tag{2.66}$$

A time evolution balance equation, formally similar to fluid one defined in eq. 2.10 may be written also for the pseudo energies [50]:

$$\frac{\partial E^{\pm}(k,t)}{\partial t} = F^{\pm}(k,t) + T^{\pm}(k,t) - 2\nu k^2 E^{\pm}(k,t) \tag{2.67}$$

As in the case of fluid turbulence, local interaction between wave vectors $\mathbf{k}+\mathbf{q}+\mathbf{p} = 0$ is assumed. We now demonstrate that the presence of magnetic field strongly influence the energy decay spectrum. This phenomenon is well known as the *Alfvénic effect*.

Let us consider the interactions between alfvénic fluctuations of same scale $l \sim 1/k$. Two characteristic times may be defined:

$$\tau_A \approx \frac{l}{v_A} \qquad \tau^{\pm} \approx \frac{l}{z_l^{\mp}} \tag{2.68}$$

where τ_A is the alfvénic time which is determined by the velocity of propagation of fluctuations along the field lines. The second characteristic time $\tau_l^{\pm}$ corresponds to the life time of the fluctuating eddies. Generally $\tau_A \ll \tau_l^{\pm}$ so that $N^{\pm}$ interactions between similar eddies will be necessary to obtain a variation $\Delta z^{\pm}$ equivalent to $z^{\pm}$. Taking into account the stochasticity of the process $N^{\pm} \approx \left(\frac{\tau^{\pm}}{\tau_A}\right)^2$ [51], the main energy transfer time will be:

$$T_l^{\pm} = N^{\pm}\tau_A \approx \frac{(\tau_l^{\pm})^2}{\tau_A} \gg \tau_l^{\pm} \tag{2.69}$$

The Alfvénic effect makes energy transfer process slower with respect to non-magnetised fluid. Let us assume $|\delta z_l^{+}| \sim |\delta z_l^{-}| \sim |\delta z_l|$ and consider the energy

flux $\Phi \sim (\delta z)^2/T$. Using eq. 2.69 we obtain that energy $\varepsilon \approx (\delta z)^4/(v_A l)$. Writing now $(\delta z)^2 \sim kE(k)$ where $E(k)$ is the energy density in mode k, we derive:

$$E(k) \sim C_k(\varepsilon v_A)^{1/2} k^{-3/2} \tag{2.70}$$

This is the so-called *Iroshnikov-Kraichnan* spectrum [52, 53]. It is less steep than the Kolmogorov spectrum because the factor τ_l/τ_A by which the transfer time is longer, increases with decreasing l and therefore increasingly higher amplitudes are required compared to the Navier-Stokes case to produce the same energy transfer. In contrast to Kolmogorov spectrum, which depends only on the inertial range quantity ε, the MHD energy spectrum depends explicitly on the large scale quantity v_A related to the mean magnetic field B_0.

2.8 Intermittency

Starting from the Navier-Stokes equation, Kolmogorov analytically showed that in statistically homogeneous turbulent fluids, the third order moment of the fluctuations of the velocity component parallel to the average flow has a scaling like [54]:

$$\left\langle (\delta v_{\parallel}(\mathbf{l}))^3 \right\rangle = -\frac{4}{5}\varepsilon l \tag{2.71}$$

This last equation, together with the scaling transformation (eq. 2.22), implies that:

$$\delta \mathbf{v}(\lambda l) \sim \lambda^h \delta \mathbf{v}(l) \tag{2.72}$$

with a unique value of the exponent $h = 1/3$. This implies that the statistical properties of the velocity fluctuations, for example the Probability Density Function (PDF), do not depend on the scale l of the fluctuations themselves: this is the *self similarity* of the turbulence.

However, in the last twenty years , it has been shown that in systems where fully developed turbulence occurs, the shapes of the PDFs of the velocity field increments change with the scale l. The PDFs at large scales are more or less Gaussian, while, as the scale decreases, they show sharper peaks and, correspondingly, higher tails (see ref. [55] and references therein for a review). Some examples of such behaviour, coming from earth surface atmospheric boundary layer, solar wind and laboratory plasmas respectively, are shown in fig. 2.4.

This scale dependence of the PDFs indicates that large increments become relatively more and more probable as scales get smaller. This means that turbulent flows are characterised by the presence of strong coherent structures localised in some regions of space. This breakdown of self similarity is called *intermittency* and represents one of the central problems in the theory of turbulence.

2.9 Turbulence and transport in plasmas

Plasmas were initially thought to be quiescent so that transport would occur according to classical diffusion, where particles are lost only by Coulomb collisions

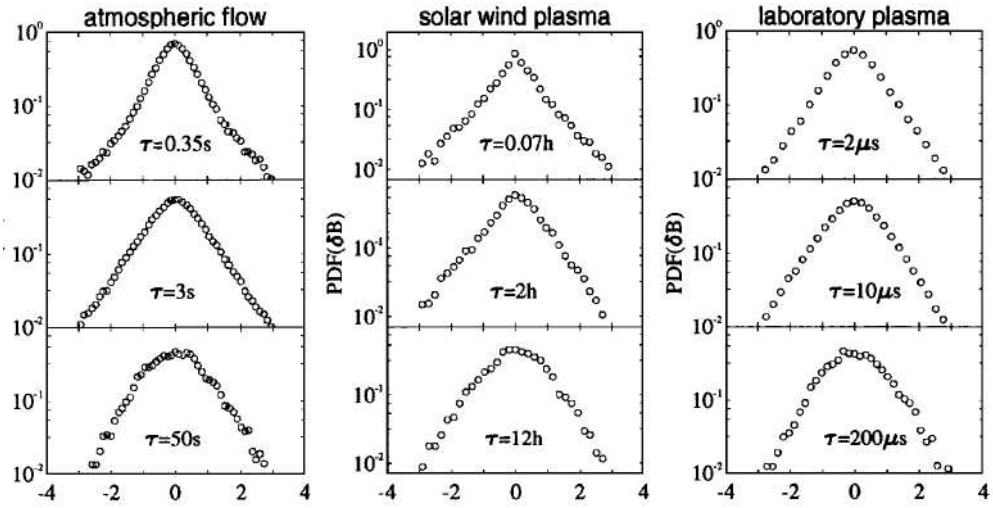

Figure 2.4: *PDFs of field increments, at three different time scales (τ on each figure) for three different turbulent system (from ref. [56]).*

with other particles. However, measured particle and energy transport in all the magnetic devices are generally enhanced beyond the level determined by collisions. Observations show that plasmas are not quiescent but rather exhibit fluctuations in all their parameters, such as density, temperature, potential and magnetic field. These fluctuations, which give rise to turbulent motion, are considered the main cause of the *anomalous transport* [4].

There are two types of fluctuations which are cause of transport: electrostatic and magnetic. In the first case the cross-field velocity is governed by the $\mathbf{E}\times\mathbf{B}$ drift velocity, where the electric field is $\mathbf{E} = -\nabla\phi$. In the second case, magnetic islands are formed in plasma so that radial diffusion along a field line around the island occurs at a much higher rate than across the field lines. The magnetic turbulence is dominant in the plasma core, the electrostatic one in the edge. In this thesis only the electrostatic turbulence is considered, as the edge plasma is studied.

2.9.1 Electrostatic turbulence

For electrostatic turbulence that characterises the plasma edge, a treatment similar to one described in the previous paragraphs for the hydrodynamic and MHD turbulence is quite difficult; the reason resides on the fact that a zoo of microinstabilities has been proposed to take into account the observed anomalous transport but a definite answer seems quite far to be reached.

Very quickly we can remind that anomalous particle flux is determined by cross correlation between density and electric field fluctuations or equivalently between density and potential fluctuations. Among the models for the evolution of electrostatic potential ϕ and density n the simplest one is the one-field Hasegawa-Mima (HM) model [57]. In this model the density response is assumed to be adiabatic $n = e\phi/T_e$ and the pressure and magnetic perturbations are assumed to be small. The governing equation may be written as [58]:

$$\frac{d}{dt}\rho_i^2\nabla_\perp^2\phi - \frac{\partial\phi}{\partial t} - V_{de}\frac{\partial\phi}{\partial y} = 0 \tag{2.73}$$

where ρ_i is the ion mass density and V_{de} is the electron drift velocity in an adiabatic response:

$$V_{de} = \frac{T_e}{eBL_n} \qquad L_n^{-1} = -\left|\frac{\nabla\bar{n}}{\bar{n}}\right| \tag{2.74}$$

For this model is has been recently observed [59] that a sort of Kolmogorov like "3/2" spectrum for the energy cascade can be evidenced and strong deviations from gaussianity in the velocity field are recovered.

2.9.2 Turbulence suppression

There is accumulating evidence that sheared $\mathbf{E}\times\mathbf{B}$ plasma flow is the mechanism most likely responsible for edge turbulence suppression and confinement enhancement (ref. [60] and references therein). This flow is caused by a non-zero electric field, and the correspondent fluid velocity perpendicular to the main component of the magnetic field is:

$$\mathbf{v}_{E\times B} = \frac{\mathbf{E}\times\mathbf{B}}{B^2} \tag{2.75}$$

The mechanism of the sheared flow is responsible of the formation of edge and core transport barriers and so of the improved confinement regimes: in fact,

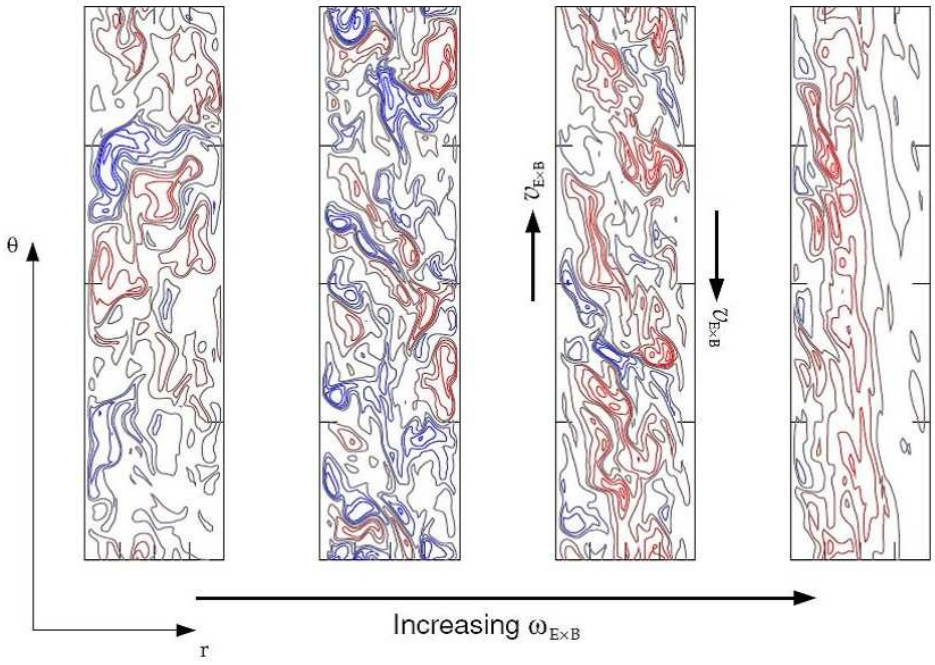

Figure 2.5: *The effect of a sheared $E\times B$ flow on plasma turbulence (from ref. [61]). Increasing the shear $\omega_{E\times B}$, the edge eddies are reduced*

transport barriers at the edge are characterised by reduced turbulence and are accompanied by an increase in the $\mathbf{E} \times \mathbf{B}$ velocity shear [25, 62].

The $\mathbf{E} \times \mathbf{B}$ flow shear

$$\omega_{E\times B} = \frac{\partial}{\partial r} v_{E\times B} \tag{2.76}$$

reduces the plasma turbulence by nonlinear decorrelation: it decorrelates the turbulent fluctuations, decreases the radial correlation lengths and fluctuation amplitudes and changes the phase between density and velocity fluctuations, thereby resulting in a reduction of radial transport. In the sheared $\mathbf{E}\times\mathbf{B}$ flow, the turbulent eddies become elongated and eventually break up. Figure 2.5 gives an illustration of a numerical simulation of turbulent decorrelation [61].

One of the most cited model for the theoretical investigation of the turbulence decorrelation is the one developed by Biglari, Diamond and Terry (BDT model) [63]. This model shows how electric field shear can nonlinearly stabilise a broad class of turbulent modes. The criterion for shear decorrelation to be important is when the shearing rate exceeds the decorrelation time. This can be written as:

$$\frac{\bar{\lambda}_\perp}{\Delta r_t \Delta t_t} < \frac{\partial}{\partial r} v_{E\times B} \tag{2.77}$$

where $\bar{\lambda}_\perp$ is the average perpendicular wavelength, Δr_t is the radial correlation length and Δt_t is the turbulence autocorrelation time. There are many experimental evidences that the disequation 2.77 is satisfied independently from magnetic configurations, and this is a remarkable indication of some universal property of edge turbulence [60, 64].

3

The Gas Puff Imaging Diagnostic

3.1 Basic principles of the GPI

The *Gas Puff Imaging* (GPI) diagnostic is an optical, non-intrusive diagnostic for studying the plasma edge of fusion devices, and particularly the edge turbulence. It measures the visible light emission, usually the line emitted by neutral Hydrogen, Deuterium or Helium that are present in the plasma edge. These atoms are excited by collisions with the electrons and in the de-excitation they emit photons. In order to increase the light signal level, neutral gas can be puffed in the plasma edge.

The line emission is due to the decay of an ion or atom from the excited state. The number of photons emitted per unit time and volume due to the transition $j \rightarrow i$ with $(E_j > E_i)$ is:

$$W_{ij} = A_{ij} N_{exc} \tag{3.1}$$

where N_{exc} is the density population of the excited level j and A_{ij} is the decay probability.
The GPI diagnostic can use, as mentioned above, various types of gases; as the behaviour is similar, here we suppose to use Hydrogen and so the H_α line of neutral atom. This line is due to the decay of the electrons from the energy level with $n = 3$ to the level $n = 2$, and the wavelength is $\lambda = 656.3\, nm$. The equation 3.1 can be written as:

$$I_{H_\alpha} = n_0 f_{H_\alpha}(n_e, T_e) A_{32} \tag{3.2}$$

where I_{H_α} is the emission rate in $[m^{-3} s^{-1}]$, and n_0 is the local density of the neutral Hydrogen. The function $f_{H_\alpha}(n_e, T_e)$ is the ratio between the density of the electronic state with $n = 3$ and the ground state, and depends on both electron density and temperature [65, 66].

The GPI diagnostic is nowadays used in many plasma experiments for the study of the edge turbulence. It is used as a "simple" light emission measurement (1D)

or with 2D cameras. The history of the diagnostic is described in the next section.

3.2 The GPI evolution

The use of the Gas Puff Imaging diagnostic for studying the edge turbulence has a long history, and it has been one of the first diagnostic that measured the turbulence in the plasma edge, pointing out the presence of violent plasma instabilities during the plasma discharges and the presence of "filaments" highly elongated in the direction of the main magnetic field.

Initially, the light fluctuations (H_α, D_α or HeI) were measured with photodiode arrays, allowing a characterisation in one dimension of the plasma edge turbulence. The first analysis was made by dr. S.J Zweben in the early '80s in the Caltech Tokamak [67]: he showed that the H_α light collected in the plasma edge possessed a small-scale broadband structure similar to what measured for plasma edge density turbulence.

Then, after using photodiode or photomultiplier arrays for gathering 1D information on the turbulence, the tokamak experiments began using cameras in order to study directly also the 2 dimensional structure of edge fluctuations. One of the first images of the edge filaments taken with a fast camera was made by Zweben in TFTR tokamak (ref. [68]), and is shown in figure 3.1.

The camera had an exposure time of $10\,\mu s$, and it clearly shows the presence in the plasma edge of filaments extended along the magnetic field lines.

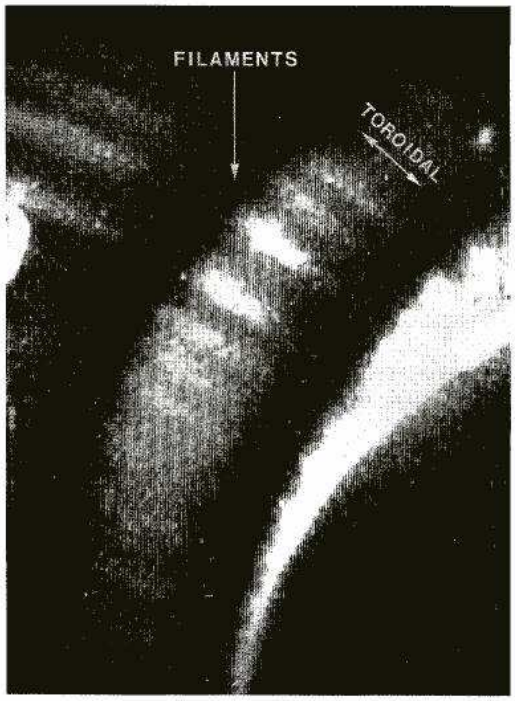

Figure 3.1: *Image of D_α light in the TFTR tokamak (from [68]). The bright stripes are filaments of D_α elongated along the magnetic field lines.*

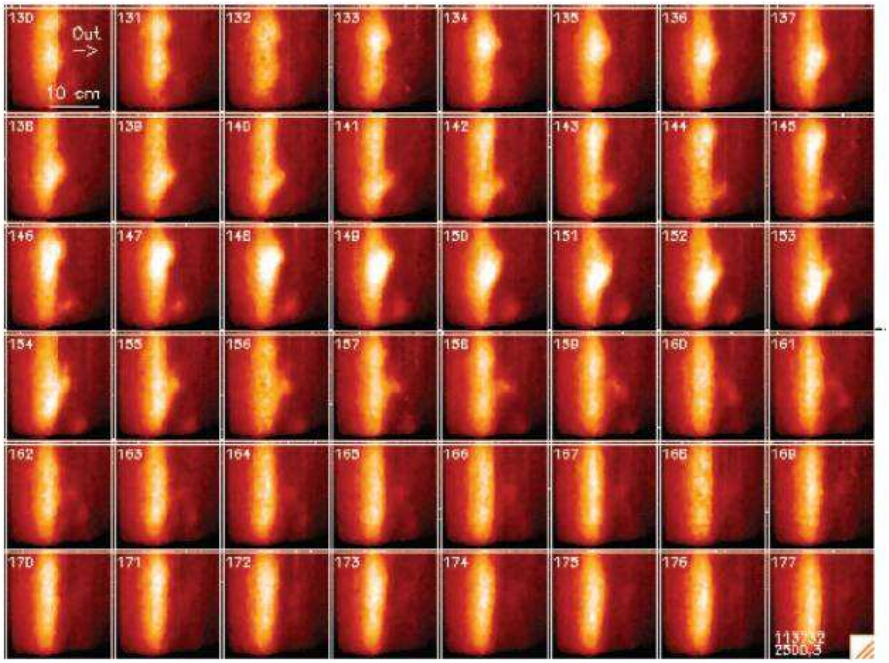

Figure 3.2: *Example of 48 frames taken by the PSI-5 fast camera in NSTX experiment. It is visible a blob moving poloidally and radially in the plasma edge. (From [72]).*

After these first works, the GPI, especially as fast camera, knew a fast development and it is used up to now in many devices; from a single frame it developed up to detect movies at high frequency that allow viewing the evolution of the edge structures.

The first GPI fast cameras were used in TFTR tokamak to study the edge plasma physics and the edge turbulence in particular. These first instruments are described in [69, 70]. This camera allows the operation at 1000 frames/s with an exposure time of 10 μs. Then, it is evolved into the PSI-4 fast camera installed in NSTX [71] tokamak experiment; this camera allows 10^6 frames/s, and the two dimensional images had shown regions of strong localised light emission, the "blobs", which move both poloidally and radially. The last evolution is the PSI-5 fast camera, with a higher time resolution (250000 frames/s), used in NSTX [72] and Alcator C-Mod [73]. With this camera it is possible to study the evolution of the edge blobs that characterise the turbulence in the edge plasma. One example of 48 frames taken in the NSTX edge is reported in figure 3.2. (Many GPI movies from NSTX and Alcator C-Mod experiments can be found at http://www.pppl.gov/∼szweben/).

This camera has the disadvantage that it can store only 300 frames per shot, and so it is not possible to study the statistical properties of the blobs. To increase the number of frames measured, the PSI-7 camera is installed in NSTX tokamak; it can measure up to 350000 frames but with a resolution of 120000 frames/s [74]. Today, besides NSTX and Alcator C-Mod, also the TJ-II stellerator in Spain has a fast camera to study the edge turbulence [75].

Together with fast cameras, the GPI is already used also as 1D array of PMTs or photodiode in many plasma devices.

To demonstrate the great impact that the GPI systems have in studying the plasma turbulence, we can add that recently this diagnostic has been installed also in the CSDX linear plasma device to reveal the spatio-temporal properties of radially events [76]. In this experiment, as in the mentioned fusion machines, the GPI is used together with the Langmuir probes.

By now it is clear that this diagnostic technique is widely and successfully applied to the tokamak configurations and linear experiments, where direct imaging can be readily obtained since in these devices the lines of sight are tangential to low curvature magnetic field lines. On the other hand in the edge plasma region of the RFP configuration the magnetic field is mainly poloidal, thus the higher curvature intrinsically reduces the resolution and makes difficult the use of fast CCD cameras. In order to overcome this problem, a tomographic like arrangement for the lines of sight of the GPI has been adopted in the RFP experiments where the GPI was used (TPE-RX and RFX-mod) [77], in which the observation is made on a plane perpendicular to the magnetic field.

Furthermore, the GPI has been used to study the magnetohydrodynamics instabilities in Magneto-Plasma-Dynamic thrusters [78], thus demonstrating the great versatility of the diagnostic.

3.3 The GPI systems in this thesis

In this section the experimental equipment used is described. The three GPI diagnostics installed in the three experiments are quite different from each other. In NSTX there are two arrays of photomultiplier tubes (PMTs) and a fast CCD camera. The GPI used in TPE-RX and in RFX-mod is the same hardware system, but in RFX-mod it has been improved with magnetic coils and a different gas injector system. For this reason, the main description of the GPI used in the two RFP experiments is made in the section regarding TPE-RX, and only the new upgrades are described in the section about RFX-mod.

3.3.1 GPI in TPE-RX

The Gas Puff Imaging diagnostic installed in TPE-RX experiment consists of a gas-puffing nozzle and an optical system for the GPI function and it is completed by a retractable electrostatic rake probe [77]. A photo of the equipment is shown in figure 3.3.

The optical diagnostic arrangement views the edge region in the plane perpendicular to the main component of the magnetic field, that is the radial-toroidal plane in the RFP experiments. It covers an observation region of about $80\,mm$ along the toroidal direction and $40\,mm$ in the radial one, by means of three optical fans: the central fan with 16 lines of sight (LoS) directly observes the edge region from the radial direction; the other two fans, each with 8 LoS are aimed at the observation region at about $38°$ to the radial direction, after three reflections over two

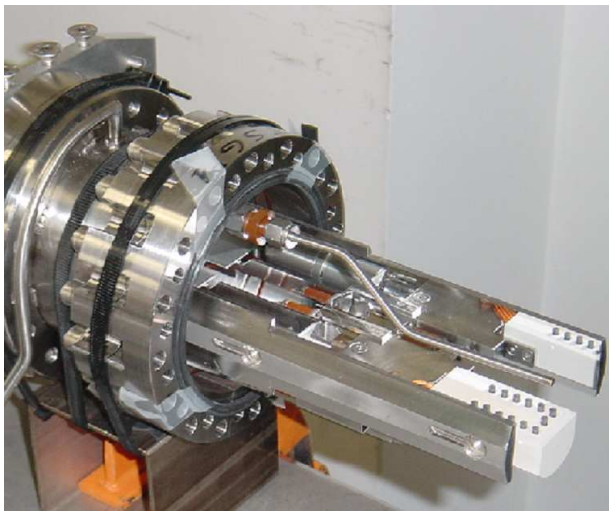

Figure 3.3: *View of the head of the GPI system before the installation in the TPE-RX experiment. The two mirrors, the array of Langmuir probes and the gas puffing nozzle are visible.*

metal mirrors. The geometrical disposition of the LoS is schematized in fig. 3.4. The same geometrical configuration is also used for the RFX-mod experiment.

In the focal region the spacing between adjacent LoS is $5\,mm$ and the beams

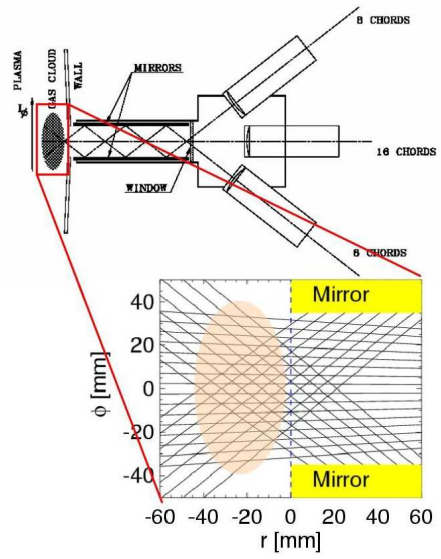

Figure 3.4: *Schematic drawing of the GPI system used in TPE-RX and RFX-mod, sketching the three fans of* 32 *optical chords focused onto a puffed cloud. The inset shows a zoom of the region of the puffed gas cloud. All the* 32 *lines of sight are shown in the radial-toroidal plane, that is the plane perpendicular to the magnetic field. The vacuum vessel is located at* $r = 0\,mm$.

have a diameter between 3 and 4 mm. The light is collected by the optics (focal length 100 mm, $f^{\#} = 2$) at the port window and sent through optical fibers (diameter 1 mm, length 35 m) to two detectors, each equipped with an interference filter for the D_α line ($\lambda = 658\,nm$, $\Delta\lambda = 3.3\,nm$) and a 16 channels photomultiplier array Hamamatsu 5900U-20-L16.

Deuterium (in Deuterium plasma) is puffed to enhance the brightness of edge fluctuations. A reservoir is filled at a pressure of $1-2$ bars and the flux is regulated by a piezo-electric valve. The gas influx can be varied from 10^{18} to 10^{19} atoms/s, corresponding to a local neutral density on the order of $10^{17} - 10^{18}\,m^{-3}$. The head of the gas injector is 30 mm long with an internal diameter of 1 mm and the expected visible size of the gas cloud is between 30 and 50 mm in the radial direction and about 70 mm in the toroidal one.

The current signals of the PMTs array are amplified by operational amplifiers, configured as transimpedance converters with a gain of 20 $mV/\mu A$. At this gain the equivalent noise input level generated by the converter is of the order of the dark current of the PMT sensor and the analog bandwidth is 1.8 MHz. A further gain/buffer stage amplifies the signal by a factor of 2.5.

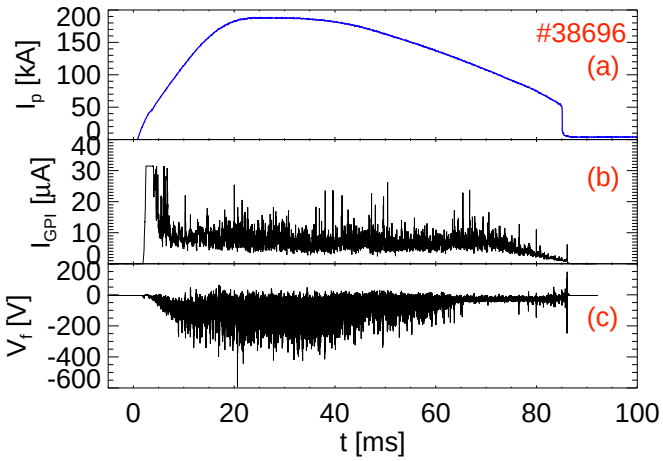

Figure 3.5: *Example of the signal collected by the GPI in TPE-RX experiment. Plasma current (a), D_α fluctuations measured with the GPI (b) and floating potential measured by Langmuir probe (c).*

The GPI system used in TPE-RX is complemented by two radial arrays of Langmuir probes, which measure the floating potential V_f to investigate the electric field structure, comparing the data with the optical ones. The Langmuir probes are arranged into two radial arrays of six probes each. Probes are spaced by 6 mm in the radial direction and 12 mm along toroidal one (see fig. 3.3). The most inserted raw is equipped with an additional electrode to provide the electron temperature measurement.

Each probe consists of a graphite cylinder (3 mm diameter, 15 mm length), housed in a boron nitride cage and screwed into a hole reinforced by Helicoil insert.

The probe system is mounted on a sliding carriage, moved by a screw connected to a stepper motor with gear reduction in vacuum, in order to avoid cumbersome mechanical feedthroughs.

The signals coming from the PMTs and from the Langmuir probes are acquired at 10 Msamples/s by 12 bit analog to digital modules (Yokogawa WE 7116). The high sampling frequency is needed to study the edge fluctuations and their statistical properties.

Figure 3.5 reports the typical edge fluctuations of TPE-RX measured both with the optical diagnostic (b) and with the Langmuir probe (c); the plasma current signal (a) is also represented. Both the optical and the floating potential signals are characterised by large fluctuations for all the plasma duration. As the two measurements are related to the same toroidal position, this arrangement allows to compare the two signals and to study the relation between the fluctuations of emissivity and floating potential.

3.3.2 GPI in RFX-mod

The Gas Puff Imaging diagnostic installed in RFX-mod is the same as the one just described for TPE-RX. The same arrangement of the LoS in the radial-toroidal plane of figure 3.4 has been used. Some improvement has been carried out when it was installed in RFX-mod after the measurements in the Japanese experiment.

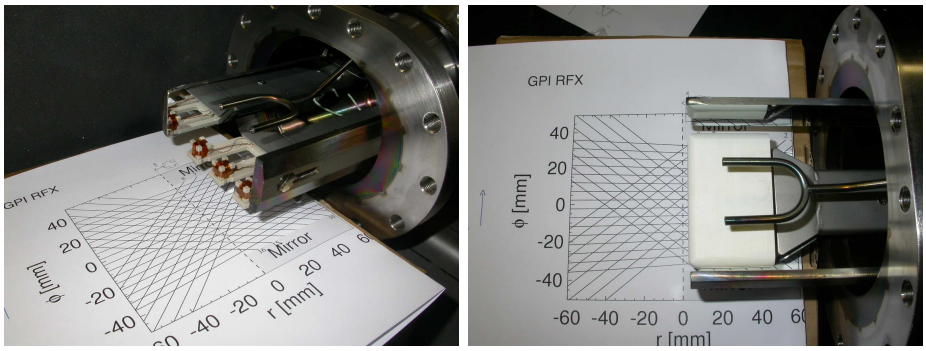

(a) (b)

Figure 3.6: *The GPI installed in RFX-mod. The fork-like nozzle for puffing the Helium, the magnetic coils and the two mirrors are visible. "Naked" triaxial magnetic coils (a) and the boron nitride cage that protects the coils from the plasma (b).*

In RFX-mod Hydrogen is used as principal gas for the discharge, and the GPI puffs Helium to highlight the edge fluctuations. As a matter of fact, it has been found that Helium provides more local information as the measurements are not affected by the background light [79]. For this reason, the interference filters has been changed, and it is centred in the HeI line, at $\lambda = 667.8\,nm$. Also the gas nozzle has been modified: the new one is made like a fork, with two different holes separated in the toroidal direction to obtain a wider (along the toroidal direction) and more uniform cloud of neutral Helium.

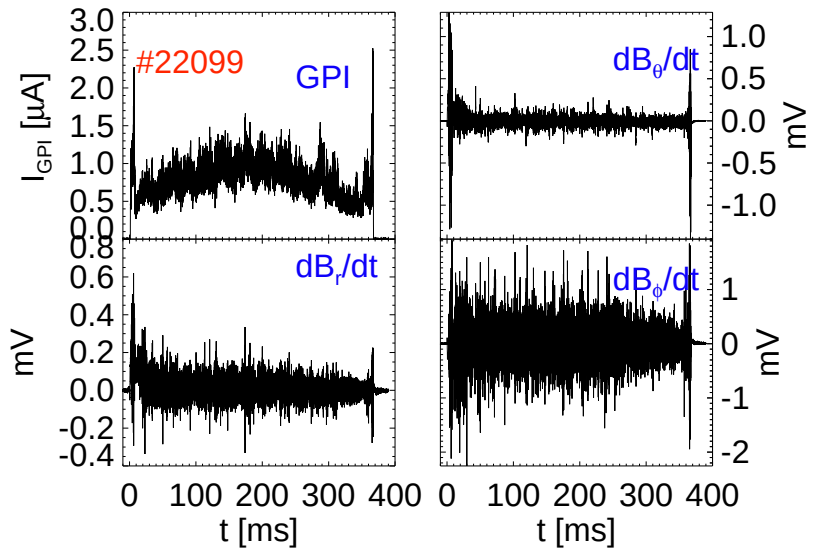

Figure 3.7: *Examples of signals collected by the GPI in one typical discharge of RFX-mod. The first signal is the fluctuation of edge emissivity; the other three are the raw signals of the magnetic coils, proportional to the time derivative of the magnetic field.*

Another significant change is the replacement of the Langmuir probes with three triaxial magnetic pick-up coils to measure the three components of the magnetic field $\dot{B}_r$, $\dot{B}_\theta$ and $\dot{B}_\phi$, and compare them with the fluctuations of the emissivity. These coils are housed in a boron nitride cage to protect them from the heat and particle flux. This description of the diagnostic is summarised in figure 3.6. In the two photos the new equipment is captured: the two mirrors for the lateral fans, the magnetic coils and the boron nitride cage, the new double nozzle for puffing the neutral Helium are visible.

The acquisition system is the same used for the GPI in TPE-RX: all the signals are acquired at 10 MHz to detect the fluctuations of the plasma edge.

An example of the experimental signals (optical and magnetic) collected in one discharge of RFX-mod are reported in fig. 3.7. This equipment allows the contemporary measurement of the edge fluctuations of the emissivity and of the magnetic field, and so it is possible to study the magnetic structure of the edge turbulence in detail.

3.3.3 GPI in NSTX

The GPI used in NSTX tokamak consists in a fast CCD camera and two arrays of photomultiplier tubes [72, 80]. The GPI diagnostic measures the D_α fluctuations emitted by the neutral Deuterium puffed into the plasma edge, and views the puff from along the local **B** field line at the edge, to resolve the radial and poloidal structure of the turbulence.

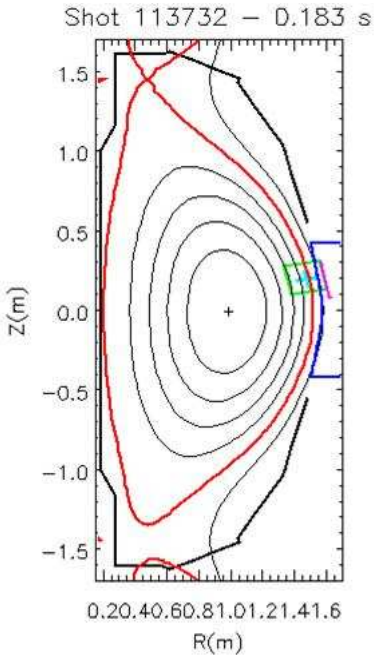

Figure 3.8: *NSTX layout, with the region viewed by the GPI camera (the green square).*

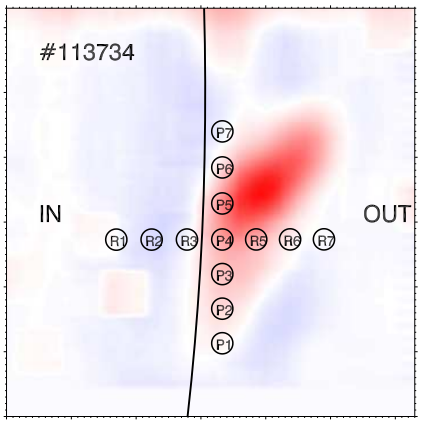

Figure 3.9: *One smoothed frame of the CCD camera of NSTX in the radial poloidal plane. The continuous black line is the separatrix evaluated with LRDFIT algorithm; the circles are the two arrays of PMT, spaced by* $20\,mm$.

The viewed region is emphasized in fig. 3.8: the figure depicts the geometry of the NSTX experiment, and the green square indicates the region were the GPI is focalised, that is near the external radius of the machine.

The D_α line emission is measured with a charge coupled device (CCD) camera, that is the PSI-5 fast camera that records 250000 $frames/s$ for $1.2\,ms$, for a total of 300 frames per discharge. This camera provides a direct 2D imaging of the turbulence. It has 64×64 pixels, for a total viewed area of $230 \times 230\,mm^2$.

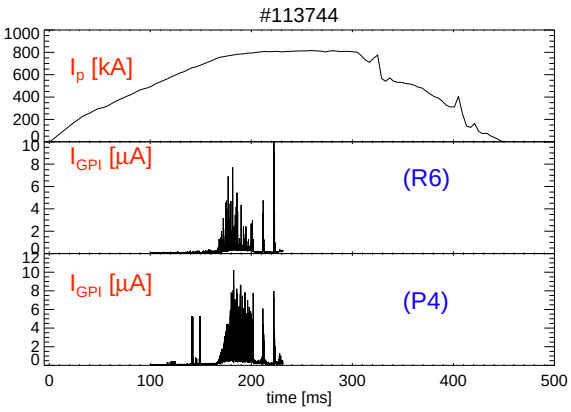

Figure 3.10: *Time behaviour of plasma current and of two GPI chords (R6 and P4) for the NSTX experiment.*

In NSTX there are also two arrays of PMT that allow a higher sampling rate ($500\,kHz$) for $64\,ms$ during the plasma discharge. Each chord in these arrays views a $20\,mm$ diameter section of plasma, and their centers are spaced by $20\,mm$. The two systems observe the line emission in the radial-poloidal plane, that is the plane perpendicular to the local magnetic field. The viewing geometry of the GPI diagnostic is shown in figure 3.9: one frame of the PSI-5 camera is shown (the time average-image has been subtracted out to show only the fluctuating part) together with the PMT chords and the separatrix position evaluated with the equilibrium reconstruction (LRDFIT algorithm). The names written in the figure are assigned to each chords.

Figure 3.10 points out the time behaviour of two GPI chords (R6 and P4 of fig 3.9) with the plasma current. The puffing of neutral Deuterium starts at about $t = 165\,ms$ and the data are recordered for $64\,ms$ during the flat top of the plasma current.

3.4 Upgrade of the GPI in RFX-mod

A new radial fan with two arrays of 10 lines of sight each has been installed as an improvement of the GPI of RFX-mod, to obtain a better radial resolution respect to the original diagnostic. These LoS are focused in the center of the Helium cloud. In the focal plane, the two arrays of 10 lines have a radial separation of 5 mm and a poloidal separation of 2.5 mm. One array is used as a new radial fan for the tomographic inversion in order to improve the radial resolution of the 2-dimensional pattern reconstruction, the other array is used for a new diagnostic for measuring the radial profiles of electron temperature and density with the Helium line intensity ratio, method described in section 3.4.1.

The optical system of the new equipment is described in figure 3.11; the new optics are installed in the nearest port of the GPI that are 15 degrees toroidally separated.

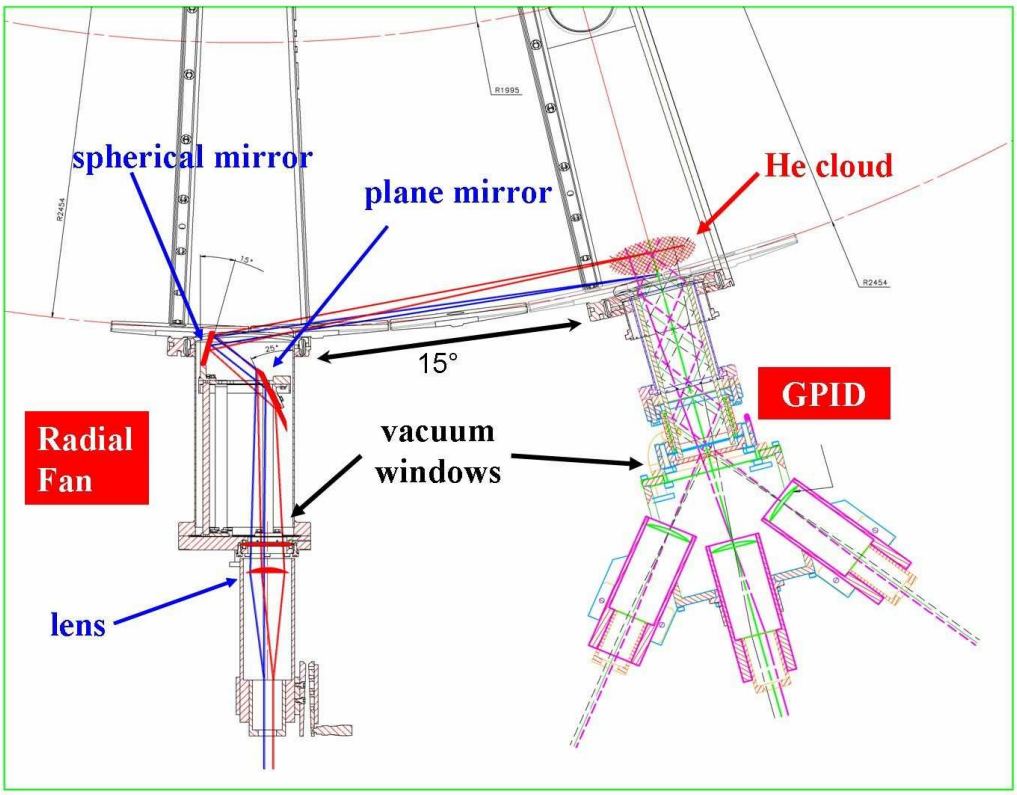

Figure 3.11: *The upgrade of the GPI. On the right the original GPI system with the three fans is visible; on the left the new optical system for observing the Helium cloud in front of the GPI with ten radially separated LoS is shown. As an example, the optical path of two LoS (red and blue) is shown.*

The first mirror that collects the light from the Helium cloud is a spherical mirror; after a second reflection trough a plane mirror, the light is focalised by a lens into a double array of fiber optics (one for the tomographic inversion and the other for the measurement of temperature and density) that carries the signals to the detectors.

For the ordinary GPI the dectector is a 16-channels PMT; the detection system for the line intensity ratio will be introduced in the next section.

3.4.1 GPI for temperature and density measurement

One of the new radial array of LoS installed for the improvement of the GPI diagnostic will be used, as already said, for the measurement of the edge electron temperature and density. The experimental method, introduced in the TEXTOR device [81, 82] and then used also in RFX [83, 84], consists on the observation of the intensity ratio of three selected emission lines of the HeI. In fact, when the atoms enter the plasma, they are excited by particle collisions with a rate depending on the local plasma parameters n_e and T_e. The measurement of the intensity ratio of selected pair of lines characterised by different n_e and T_e dependence allows the

evaluation of the local density and temperature.

The following HeI line intensity ratios will be used for the measurements:

$$I\,(728.1nm,\ 3^1S \rightarrow 2^1P)/I\,(706.5nm,\ 3^3S \rightarrow 2^3P) \qquad \text{sensitive to } T_e$$
$$I\,(667.8nm,\ 3^1D \rightarrow 2^1P)/I\,(728.1nm,\ 3^1S \rightarrow 2^1P) \qquad \text{sensitive to } n_e$$

The measured ratios are compared with a look-up table derived from the atomic model discussed in [85], from which the final T_e and n_e values are interpolated. The detection system will consist of a spectrograph ($f = 300mm$, $1200\,grating/mm$) used as a policromator that disperses the three considered HeI lines; then the three lines are collected by PMTs, that allow a good time resolution of the measurement. As the LoS are focused in the plasma edge and the neutral Helium is locally injected, the measurement is considered local. However, to be sure that the contribution to the line intensity due to the recycled residual Helium coming from the graphite wall is unimportant, also the light emission from a region outside the puffed Helium cloud is collected; to validate the measure of T_e and n_e, this LoS should have a signal comparable to the dark current of the PMT, indicating that the contribution of the recycled Helium is negligible.

By now the diagnostic has been installed and aligned in RFX-mod. To align the two arrays of fiber optics, we illuminated them with a lamp and each of them produces a spot in the center of a target simulating the Helium cloud source. The set-up has been calibrated such as the fiber optic 3 is focused at $r = 0\,mm$, i.e. the convolution of the graphite tiles. The result of the alignment is registered by

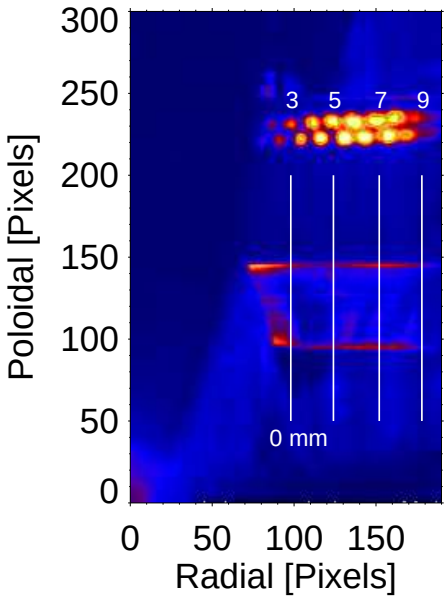

Figure 3.12: *Radial alignment of the line intensity ratio diagnostic. The target with the focused spots are visible. Line 3 is at r=0 mm, at the plasma edge; the other lines are inside the plasma. The vertical white lines are spaced by 10 mm radially.*

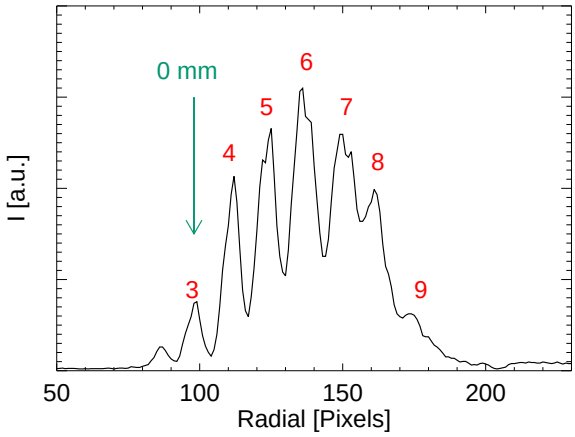

Figure 3.13: *Radial profile of the light intensity of the spots of the GPI array, which refers to figure 3.12. LoS 3 is centered at $r = 0\,mm$; each LoS is spaced by $5\,mm$.*

a CCD camera (which sees the He cloud region through a small plane mirror) and shown in figure 3.12. In the figure the target (that simulates the He cloud) with the double array of spots are visible: on the top the array for the GPI, and on the bottom the one for the line intensity ratio. The line of sight 3 of the GPI is positioned at $r = 0\,mm$, and all the spots are spaced radially by $5\,mm$. The last points are not well visible: this is due mainly to the inclination of the CCD camera respect the target, and by the fact that the camera is using the edge of the mirror to view the cloud region and this reduces the solid angle viewed.
At the same time, the analysis of fig. 3.12 shows that the spots are radially separated, and so the diagnostic can measure the edge plasma from $0\,mm$ to $35\,mm$ with a spatial resolution of $5\,mm$.

To underline this result, in figure 3.13 the radial profile of the light intensity of the GPI array collected by the CCD camera is shown. The LoS from 3 to 7 are well radially separated; LoS 8 and 9 are reduced mainly by the small solid angle viewed by the camera as already reported and not by the diagnostic itself.

Hence, the upgrade of the GPI and the installation of the line intensity ratio diagnostic provide a radial resolution of $5\,mm$ in the plasma edge. This will be used to:

(a) study the edge turbulence with the GPI and so to obtain a tomographic reconstruction of the 2D light emission pattern fluctuations with a good radial resolution, as described in chapter 4;

(b) measure the radial profiles of T_e and n_e with a high spatial resolution in order to study the link between them and the edge turbulence.

4

Mathematical tools for turbulence analysis applied to GPI data

In this chapter the mathematical tools used to analyse the GPI data are introduced. In the first section a brief introduction about the method for the spectral analysis of signals is given, pointing out which informations can be extracted from turbulent data with the Fourier transform and the Wavelet transform. There are many books in which it is possible to have a complete treatment of these arguments that are only shortly introduced here; for example, for the Fourier analysis see the reference [86], and for the Wavelet see [87, 88].

In the second section the tomographic reconstruction algorithm developed for obtaining a 2-dimensional image of the edge emissivity fluctuations from the line integrated signal of the GPI is described. This is the first time that a tomographic reconstruction method has been developed and applied to study the edge turbulence of magnetised plasmas.

4.1 Spectral analysis

4.1.1 Fourier Transform

The Fourier transform is a mathematical tools widely used in all fields of the physics research. The Fourier transform of a signal f is defined as [86]:

$$\psi(\omega) = \int_{-\infty}^{+\infty} f(t) e^{-i\omega t} dt \tag{4.1}$$

and from the Fourier transform the original signal can be obtained with the inverse Fourier transform:

$$f(t) = \frac{1}{2\pi} \int_{-\infty}^{+\infty} \psi(\omega) e^{i\omega t} d\omega \tag{4.2}$$

Since the experimental data are acquired as discrete points, the Discrete Fourier Transform (DFT) is computed. From the DFT the *power spectrum* can be evaluated. It is defined as:

$$S(\omega) = \frac{2N}{f_s} |\psi(\omega)|^2 \tag{4.3}$$

where N is the total discrete set of measurements and f_s is the sampling frequency. $S(\omega^*)\Delta\omega$ measures the contribution to the signal energy from the frequency interval $\Delta\omega$ around ω^*.

The Fourier transform will be used also to evaluate the relation between two signals of the same quantity, with the estimation of the power spectral density $S(k, f)$ where k is the wavenumber and f the frequency.

The reconstruction can be performed on a statistical basis, using the measurements of two signals. The numerical technique, described in [89, 90], proceeds as follows: the signals y_1 and y_2 of two probes are divided into N slices of equal length, $y_1^{(i)}$ and $y_2^{(i)}$, with $i = 1, \ldots, N$. The slices are considered as independent realisations of the stochastic process under study. For each slice the discrete Fourier transforms $\psi_1^{(i)}$ and $\psi_2^{(i)}$ are computed. From these, the cross power spectrum is evaluated:

$$S^{(i)}(f) = (|\psi_1^{(i)}(f)|^2 + |\psi_2^{(i)}(f)|^2)/2 \tag{4.4}$$

together with the cross phase:

$$\alpha^{(i)}(f) = arg\{[\psi_1^{(i)}(f)]^* \psi_2^{(i)}(f)\} \tag{4.5}$$

where * indicates the complex conjugate. The cross phase is used to obtain an estimate of the wave number in the direction connecting the two probes:

$$k^{(i)}(f) = \phi^{(i)}[f]/\Delta x \tag{4.6}$$

where Δx is the distance between the two probes. These results are used to progressively fill a histogram of the spectral density, i.e. for each frequency f the bin corresponding to the wave number $k^{(i)}(f)$ is increased by the amount $S^{(i)}(f)$. By repeating this procedure for all slices, the resulting histogram of $S(k, f)$ is a statistical estimate of the true spectral density function. In this procedure, we have to assume the stationarity of the process studied, and that Δx is much smaller then the fluctuation wavelength.

From the relation $v_p = 2\pi\Delta f/\Delta k$, the phase velocity of the fluctuations can be estimated from the quasi-linear dispersion relation between f and k evaluated in the $S(k, f)$ spectrum, according the method described in [90].

4.1.2 Wavelet Transform

Wavelets represent a common tool for analyzing localised variations of power within a time series. By decomposing a time series into time-frequency space, one is able

to determine both the dominant modes of variability and how those modes vary in time.

A wavelet is a function $f \in L^2(\mathbb{R})$ which satisfies the *admissibility condition*:

$$C_\psi = \int_{-\infty}^{+\infty} \frac{|\psi(\omega)|^2}{|\omega|} d\omega < +\infty \tag{4.7}$$

where $\psi(\omega)$ is the Fourier transform of f. The Continuous Wavelet Transform (CWT) of a function y at time s and scale a is defined as:

$$w(s,a) = \frac{1}{\sqrt{a}} \int_{-\infty}^{+\infty} y(t) f^* \left(\frac{t-s}{a} \right) dt \tag{4.8}$$

The wavelet transform $w(s,a)$ measures the variation of y in the neighborhood of s whose size is proportional to the scale a.

The free parameter of the CWT is the choice of the wavelet function f. There are many different possibilities: functions that are orthogonal or nonorthogonal, real or complex, with different widths and shapes. We do not enter the details of the different possibilities (one can read for example reference [91]), but in this thesis the wavelet transform is used to detect peaks in the signals, and one of the best choice for doing this is the *Mexican Hat* wavelet.

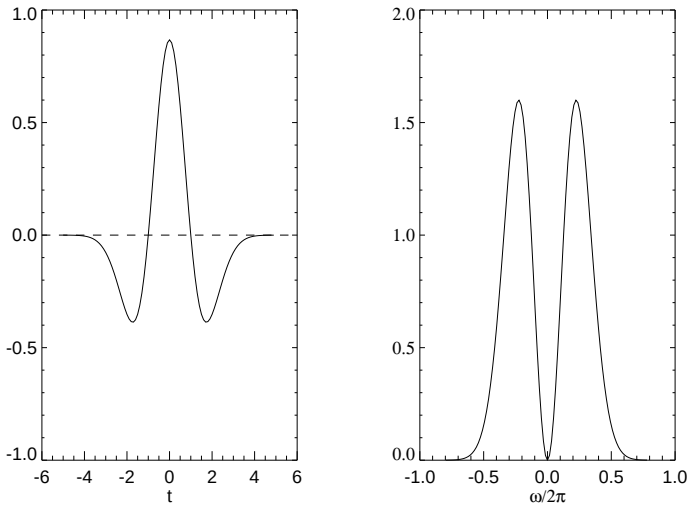

Figure 4.1: *The wavelet function used in this thesis: the Mexican Hat (left) and its Fourier transform (right).*

The Mexican hat is the second derivative of a Gaussian, and it is defined as:

$$\begin{aligned} f(t) &= \frac{2}{\pi^{\frac{1}{4}}\sqrt{3a}} \left(\frac{t^2}{a^2} - 1 \right) e^{-\frac{t^2}{2a^2}} \\ \psi(\omega) &= -\frac{\sqrt{8} a^{\frac{5}{2}} \pi^{\frac{1}{4}}}{3a} \omega^2 e^{-\frac{a^2\omega^2}{2}} \end{aligned} \tag{4.9}$$

In figure 4.1 it is represented.

The Fourier Transform of the Mexican Hat is centered at frequency $f \approx 1/4a$. For this reason the wavelet time scale is identified with the inverse of the Fourier frequency $\tau \approx 4a$. In the whole thesis, with the term *scale* we refer to this quantity.

4.2 Tomographic reconstruction algorithms

One of the goal of the Gas Puff Imaging diagnostic used in the RFP experiments is obtaining the two-dimensional image of the edge plasma in the plane perpendicular to the main component of the magnetic field. In particular it is developed to study the two-dimensional evolution of the edge structures. Similar investigations are carried out in tokamaks by means of fast cameras [92, 93, 71]; however, the less favorable topology of magnetic field lines in reversed field pinch experiments makes the direct two dimensional investigation of turbulent structures by cameras more difficult. Hence, exploiting the arrangement of the access ports, in RFX-mod the lines of sight have been arranged in a tomographic-like configuration on the plane perpendicular to the main magnetic field, that is poloidal in the RFP experiments.

In the next paragraphs the tomographic reconstruction methods developed for RFX-mod are described [94, 95]; then they are applied to a phantom image to detect the limitation of the tomographic reconstruction and then some application to experimental data are shown.

Mathematical tools are also developed to analyse in a simple way the reconstructed 2D images. In fact, normally the analysis of the 2D films obtained by the fast CCD cameras in tokamak experiments are difficult, and it is quite complex to extract quantitative information and to make statistical analysis of the "movies" [96].

The main aim of the reconstruction technique is to recover the emissivity pattern in the toroidal-radial plane $e(r, z)$ from the measured line-integrated signals l_i. The simplest method used to obtain rough images from the 32 LoS measurement is an application of the back-projection algorithm [97]. Back-projection is exactly what happens in a conventional camera when a 2D image is collected. This technique, applied to the three independent 1D "images" of the three fans, is capable of providing a fairly accurate 2D image of the field of view of the GPI system, more or less in the same way as two human eyes are capable of reproducing a 3D image on the basis of 2D "back projections" of the single eye.

From figure 4.2 it is conspicuous that lines of the GPI installed in the two RFP experiments belonging to each of the three fans intersect in several points in the centre of the viewed plasma region. If (r^*, z^*) are the coordinates of one of these points, the plasma emission is written as $e(r^*, z^*) \propto l_1 l_2 l_3$ meaning that the signal at the intersection point is assumed to be proportional to the product of the three line integrals l_1, l_2, l_3 intersecting in (r^*, z^*). Since the three LoS follow different paths in the plasma edge, the various contributions should cancel out; only the light emitted in the vicinity of the intersection point will give a simultaneous contribution to all three LoS yielding a triple product significantly different from zero. This method is very simple to implement, and requires small computational time; on the other hand, it is suitable when a very large number of LoS is available, since it does not assume any a-priori image pattern.

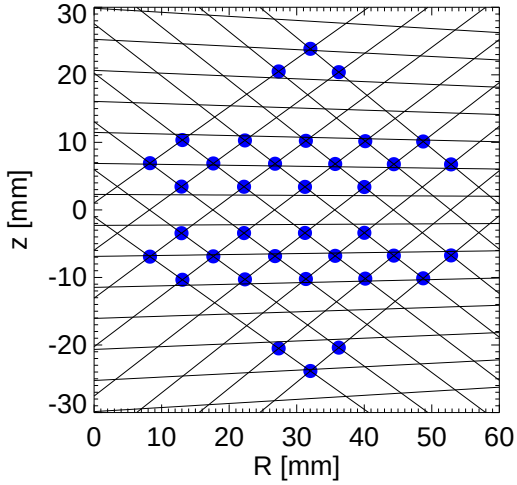

Figure 4.2: *Field of view of the GPI in the radial-toroidal plane. The blue circles are the points where three lines of sight intersect each other used for the back-projection reconstruction of the edge emissivity. This geometry has been used in the two RFP devices.*

Another way to solve the reconstruction problem consists in expanding the emissivity in a two-dimensional Fourier series (2D Fourier expansion) for each sampling time, according to the formula:

$$\epsilon(r,z) = \sum_{pq} \left[C_{pq} \cos\left(\frac{p\pi z}{\Delta z}\right) \cos\left(\frac{q\pi r}{\Delta r}\right) + D_{pq} \sin\left(\frac{p\pi z}{\Delta z}\right) \cos\left(\frac{q\pi r}{\Delta r}\right) + F_{pq} \cos\left(\frac{p\pi z}{\Delta z}\right) \sin\left(\frac{q\pi r}{\Delta r}\right) + G_{pq} \sin\left(\frac{p\pi z}{\Delta z}\right) \sin\left(\frac{q\pi r}{\Delta r}\right) \right] \quad (4.10)$$

where Δz and Δr are respectively the toroidal and radial dimension of the edge region to which the inversion is applied, and p and q are the toroidal and radial wave-numbers, and the coefficients C_{pq}, D_{pq}, F_{pq}, G_{pq} are the unknown spectral amplitudes to be determined. Integrating equation 4.10 along each of 32 LoS l_i yields the brightness:

$$f_i = \sum_{pq} \left[C_{pq} \int_{l_i} \cos\left(\frac{p\pi z}{\Delta z}\right) \cos\left(\frac{q\pi r}{\Delta r}\right) + \int_{l_i} D_{pq} \sin\left(\frac{p\pi z}{\Delta z}\right) \cos\left(\frac{q\pi r}{\Delta r}\right) + \int_{l_i} F_{pq} \cos\left(\frac{p\pi z}{\Delta z}\right) \sin\left(\frac{q\pi r}{\Delta r}\right) + \int_{l_i} G_{pq} \sin\left(\frac{p\pi z}{\Delta z}\right) \sin\left(\frac{q\pi r}{\Delta r}\right) \right] \quad (4.11)$$

Equation 4.11 is a matrix equation of the form:

$$f_i = \sum_j W_{ij} A_j \quad (4.12)$$

where the unknown coefficients C_{pq}, D_{pq}, F_{pq}, G_{pq} have been re-written as the components of the vector A_j and the coefficients W_{ij} are the results of the integration of the sine and cosine functions along the LoS and depend only on the LoS geometry.

Previous experimental results concerning electrostatic structures [98] show that $p = 0-5$ and $q = 0-3$ should be sufficient to describe the structures in RFX-mod plasma edge; in fact their typical toroidal dimension is about $20-50\,mm$ [99]. Using this choice of toroidal and radial wave numbers, with only 32 experimental LoS integrals, the resulting system of equations is underdetermined and to estimate the unknown coefficients the Singular Value Decomposition (SVD) technique is applied [100, 101, 102]. The SVD allows solving the unconstrained linear least squares problem:

$$min(J(\mathbf{A})) = min\|\mathbf{F} - W\mathbf{A}\|_2 \tag{4.13}$$

As W corresponds to a derivative operator, such a problem is ill-posed, namely a small perturbation of $\mathbf{A}$ may lead to a large perturbation in the solution; thus a regularisation is needed. The *Tikhonov regularisation* has been adopted [103]: a penalty function $P(\mathbf{A})$ is added to the object function $J(\mathbf{A})$ to create a new one $J_\lambda(\mathbf{A}) = J(\mathbf{A}) + \lambda^2 P(\mathbf{A})$, where $P(\mathbf{A}) = \|L\mathbf{A}\|_2^2$, and the matrix L is a smoothing operator, chosen as the second derivative, in order to penalise high amplitude fluctuations at small scales. The Tikhonov regularised solution $\mathbf{A}_\lambda$ is defined as the solution to the resulting least squares problem:

$$min(J_\lambda(\mathbf{A})) = min\left(\|\mathbf{F} - W\mathbf{A}\|_2^2 + \lambda^2\|L\mathbf{A}\|_2^2\right) \tag{4.14}$$

The parameter λ is chosen with the L-curve technique [103, 104], which is the parametric plot $[J_\lambda(\mathbf{A}), P_\lambda(\mathbf{A})]$ for different values of the regularisation parameter λ. This curve has a characteristic L-shaped appearance. The optimal regularisation parameter corresponds to the corner of this L-curve. So the inverted image is the best fit of the initial brightness data constrained by the smoothing operator. Indeed, unconstrained resolution would search for the lowest values of the object function J (corresponding to $\lambda = 0$ in eq. 4.14), and therefore would follow more closely the brightness measurements; however, it might be characterised by large, small-scale fluctuations.

This technique for the regularisation of the solution is used also for the tomographic inversion problem of X-ray emission in fusion plasma experiments [105, 106].

4.2.1 Application of the methods: phantom

We used both the back-projection and the 2D Fourier method on tomographic phantom to test the developed algorithms: the corresponding LoS integrals have been numerically evaluated, and the inversion algorithms have been applied, to get an image which has been compared to the phantom.

Figure 4.3 shows the phantom and the reconstruction results. A Gaussian-shape emitting pattern has been located in the zone of maximum LoS resolution (a); in (b) the reconstruction using the 2D Fourier series is shown, and in (c) the back-projection reconstruction. Both inversion techniques place the centre of the

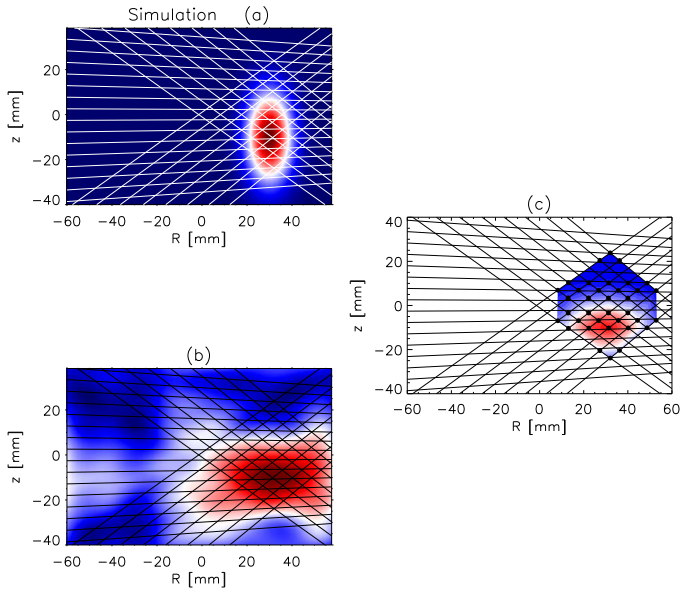

Figure 4.3: *Simulation of Gaussian emitting pattern (a) and results of reconstruction with 2D Fourier method (b) and back-projection (c). The traces of the lines of sight are shown. In (c) the black dots represents the position where three lines of sight intersect each others.*

Gaussian correctly in the radial-toroidal plane. Also the toroidal extension of the reconstructed pattern is similar to the original one, indicating that the optical system used and the numerical algorithm allow a good toroidal resolution. The radial resolution is a more critical problem: the inverted pattern using the Fourier series shows a wider radial extension than the original one. This is probably due to the small inclination of the LoS for the two lateral fans: the result is a broad structure elongated along the direction of the fans. A weakly emitting region is also reconstructed around $r = -60\,mm$: this is an aliasing phenomenon since in that region there are no intersections of LoS.

The pattern reconstructed by the back-projection technique gives an opposite appearance, as the three-point intersections are limited to a small region.

4.2.2 Application of the methods: experimental data

In this section the application of the two inversion methods to the experimental data is described. The main aim is to detect the coherent structures that characterise the plasma edge and to study their motion and evolution.

For the 32 measured time series of the integrated signal collected by the GPI during one plasma discharge, a time slice is selected and the inversion is applied; the time average of each signal is computed and subtracted from the signal; the signals

are subsequently divided by their average. This normalisation of the different signals is necessary because an absolute calibration of the system is not simple; this way the fluctuating part of the emissivity pattern is reconstructed. Then, these new time series are low-pass filtered at $1\,MHz$ to reduce noise that could make difficult the tomographic inversion. Then the two inversion algorithms are applied to the data to obtain a 2D image every sampling rate, namely every $100\,ns$.

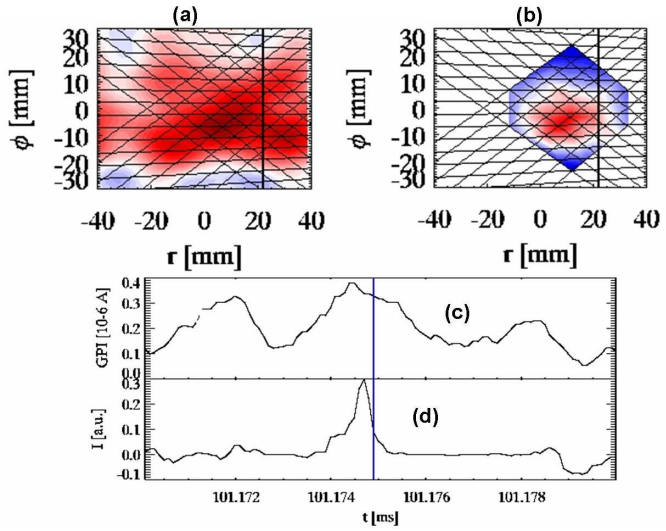

Figure 4.4: *2D inverted pattern of a coherent structure of the edge plasma. Reconstruction with Fourier method (a) and with the back-projection (b); time behaviour of one GPI signal (c) and one of the triple products (d). The inversion is made at* $t = 101.1749\,ms$ *(vertical blue line).*

In fig. 4.4 an example of inversion is shown at time instant $t = 101.1749\,ms$. At the top of the figure the comparison is provided between the two methods used: on the left the inversion using the 2D Fourier expansion, and on the right using the back-projection. In both graphs the black vertical line indicates the position of the vacuum vessel. In the lower graph, panel (c) reports the time behaviour of one LoS signal; panel (d) one of the triple products, relative to one of the central black dots; the vertical blue line indicates the time instant at which the inversion displayed has been computed.

It is clear that the integrated emission shows a peak; both methods can reconstruct an emissivity structure flowing in the field of view of the GPI, in the radial-toroidal plane. At the time instant considered in figure 4.4, the inverted structure is centred at about $-10\,mm$ in the toroidal direction. The differences in the two reconstructed emissivity patterns are about the same as described in the simulation of figure 4.3: the 2D Fourier expansion is stretched along the direction of the lateral fans, which results from a poor radial resolution. As anticipated, such observation is related to a low number of LoS intersections and to the little inclination of the lateral fans. On the other hand the toroidal resolution of both inversion methods is good.

The main difference between the two algorithms seems to be the dimension (especially radial) of the emissivity pattern: this is an intrinsic characteristic of

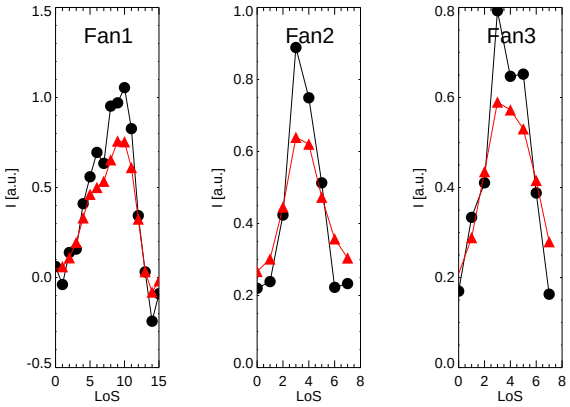

Figure 4.5: *Experimental (black circles) and Fourier-series reconstructed (red triangles) line integral signals of the GPI for the three fans at the same time instant as fig. 4.4.*

the 2D back-projection method. As it can be seen at the bottom of figure 4.4, the triple product signal in correspondence of a GPI peak is narrower than the original signals. Indeed the triple product is different from zero only when all three signals are simultaneously different from zero; consequently the structure reconstructed by the back-projection results smaller than what could be anticipated by inspection of the time signals.

To verify the quality of the reconstruction obtained from 2D Fourier expansion, in fig. 4.5 the line integrated signals measured by the GPI (black circles) and those reconstructed by the Fourier algorithm (red triangles) are compared; the reconstructed line integrals are computed by integrating the inverted emissivity along the 32 LoS. As already said the reconstruction is not meant to match exactly the experimental signals: using the L-curve method for the regularisation, the SVD inversion searches for a solution that minimises both the χ^2 and the penalty function, which aims at remaining within the spatial resolution of the diagnostic.

The tomographic reconstruction can be applied to the signals at each sampling rate. In figure 4.6 the time behaviour of experimental (black) and reconstructed (red) line integral signals are reported for two different LoS of central and lateral fan. The reconstructed signals follow very well the experimental behaviour: peaks in emissivity are reproduced, and the smoothing in the reconstructed signal is due mainly to the low-pass filter used to reduce the noise level. Thus, not only one single time instant can be inverted, but the whole time behaviour of the emissivity pattern can be reconstructed.

Thus, by applying the inversion technique to the time series, a movie of the plasma edge can be obtained. Six reconstructed images for the edge of RFX-mod are reported in fig. 4.7. At each instant, on the left, reconstructed images are shown (back-projection on top); on the right the comparison of 2D Fourier expansion line integrals for each fan, and the time behaviour of one chord of the central fan and of one triple product are displayed. Though the displayed structure is not one of the brightest, the 2D Fourier expansion can single the structure out and follow it during its motion. The sequence of structure images allows also to estimate a raw

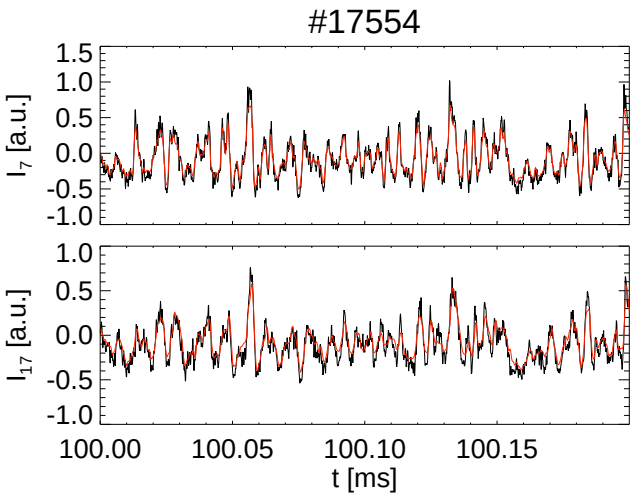

Figure 4.6: *Time behaviour of the experimental line integral (black) and of the Fourier-series reconstructed ones. Top panel is relative to one chord of the central fan, the bottom one to one chord of the lateral fan.*

toroidal speed, which is about $15\,km/s$, comparable to the average plasma flow.

The 2D Fourier expansion provides also important information concerning the analysis of the motion and the evolution of edge structures. Indeed the study of 2-dimensional images of the edge structures in fusion plasma detected with fast CCD cameras are quite complex, and it is difficult to extract any quantitative information. Moreover, as the CCD cameras can only register some hundred frames [80, 72], it is not possible to make anyone of the statistical analysis that the GPI with the tomographic reconstruction allows.

4.2.3 Analysis techniques for the tomographic reconstruction

When applied eq. 4.12, the inversion algorithm gives the values of the coefficients C_{pq}, D_{pq}, F_{pq}, G_{pq} as a function of time; they include all the physical information of the image. Such coefficients can be interpreted as the amplitudes of the modes with mode numbers p and q: so the time evolution of the total energy can be evaluated:

$$E(t) = \sum_{pq} C_{pq}^2(t) + D_{pq}^2(t) + F_{pq}^2(t) + G_{pq}^2(t) \tag{4.15}$$

as well as the energy of a particular toroidal mode p^*:

$$E_{p^*}(t) = \sum_{q} C_{p^*q}^2(t) + D_{p^*q}^2(t) + F_{p^*q}^2(t) + G_{p^*q}^2(t) \tag{4.16}$$

and analogously for a particular radial mode $E_{q^*}(t)$.

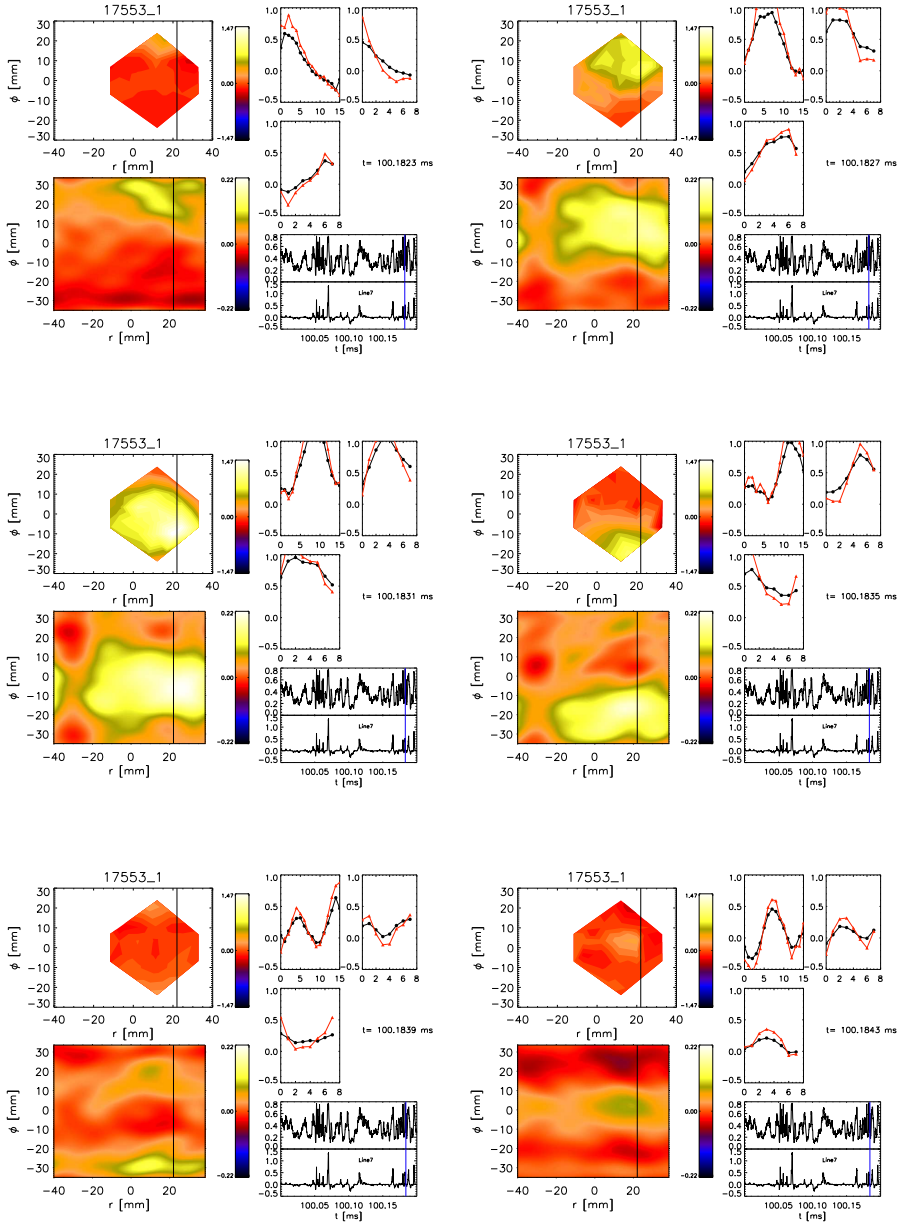

Figure 4.7: *Sequence of reconstructed images of plasma edge (see text). The time sequence is from left to right and then top to bottom.*

In fig. 4.8 the time behaviour of the Fourier mode energies (b,c,d) is compared with the GPI signal (a). The total mode energy $E(t)$ peaks in correspondence to peaks in GPI signal, which in turns correspond to structures in the reconstructed images. In figure 4.8 (c) and (d) the time behaviour of different toroidal p and radial q mode energy is shown: the two dominant toroidal modes are the $p = 0$ and $p = 1$, instead the dominant radial mode is $q = 0$.

Another important piece of information that can be extracted from the inverted coefficients C_{pq}, D_{pq}, F_{pq}, G_{pq} is the toroidal phase of the different modes. To

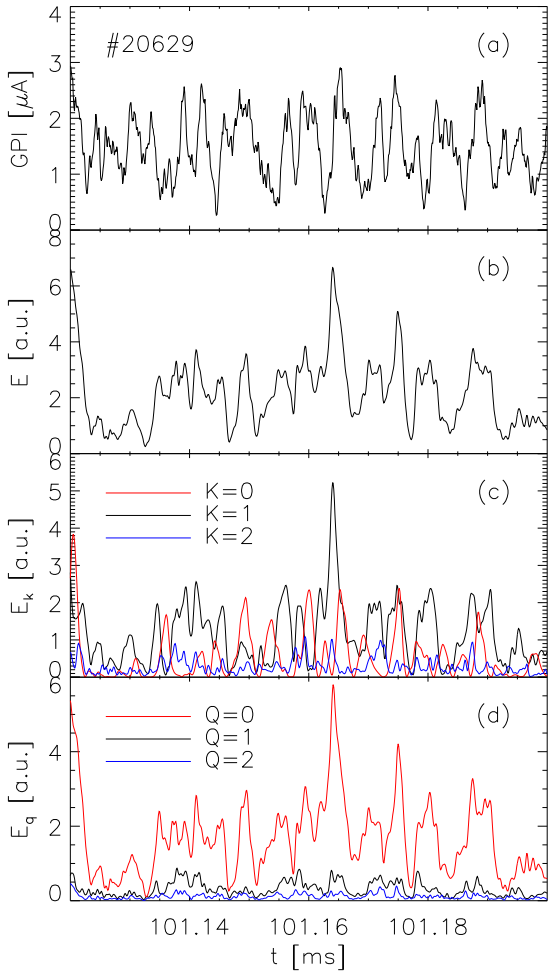

Figure 4.8: *Time behaviour of one GPI signal (a), total energy of the Fourier inverted modes (b), energy of toroidal (c) and radial (d) modes.*

evaluate the toroidal phase, equation 4.10 can be re-cast in the following form:

$$\epsilon(r,z) = \sum_{pq} \left[W_{pq}(r,t) \cos\left(\frac{p\pi z}{\Delta z}\right) + Z_{pq}(r,t) \sin\left(\frac{p\pi z}{\Delta z}\right) \right] \tag{4.17}$$

with

$$W_{pq}(r,t) = C_{pq}(t)\cos\left(\frac{q\pi r}{\Delta r}\right) + F_{pq}(t)\cos\left(\frac{q\pi r}{\Delta r}\right)$$
$$Z_{pq}(r,t) = D_{pq}(t)\cos\left(\frac{q\pi r}{\Delta r}\right) + G_{pq}(t)\cos\left(\frac{q\pi r}{\Delta r}\right) \tag{4.18}$$

From this expression the toroidal phase of the mode pq can be evaluated for a given radial position.

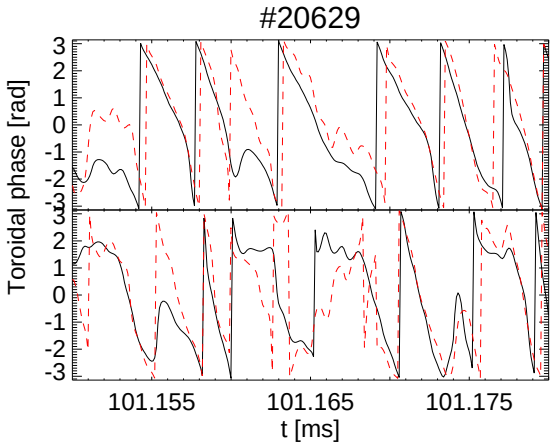

Figure 4.9: *Example of toroidal phases of the reconstructed images. Top: toroidal phase of the mode* $[p = 1, q = 0]$ *(continuous line) and* $[p = 1, q = 1]$ *(red dashed line); bottom:* $[p = 2, q = 0]$ *(continuous line) and* $[p = 2, q = 1]$ *(red dashed line).*

Fig. 4.9 shows the result of such computation for the modes $[p = 1, q = 0]$, $[p = 1, q = 1]$, $[p = 2, q = 0]$ and $[p = 2, q = 0]$. All these modes show a rotation along the toroidal direction, corresponding to the edge structures motion; an average velocity of about $15\,Km/s$ can be estimated from the figure.

The average toroidal phase of one particular mode p^* can be evaluated by summing over all q modes:

$$\tan[\phi_{p^*}(t)] = \frac{\sum_q Z_{p^*q}(r,t)}{\sum_q W_{p^*q}(r,t)} \tag{4.19}$$

Two examples of such a computation for the shot #19953 of RFX-mod are reported in figure 4.10, for $50\mu s$ time interval, along with the toroidal velocity of the fluctuations evaluated by the cross-correlation technique.

As reported in [107, 108], when an external toroidal magnetic perturbation is applied, the velocity of the edge fluctuations inverts its sign; this is what happens in the reported discharges of figure 4.10 around $60\,ms$. At the same time the slope of the average toroidal phase of the mode $p = 1$ changes, supporting the inversion of the toroidal motion: the two examples of the phase of the mode $p = 1$ refer to periods in which the velocity has different sign. Moreover, in both periods, the

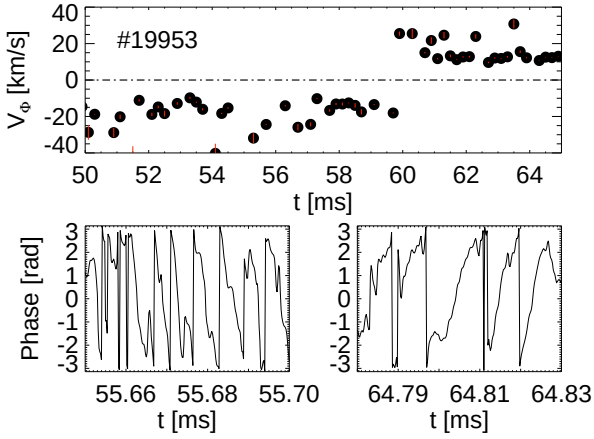

Figure 4.10: *Change of the toroidal velocity of fluctuations when an external magnetic perturbation is applied: cross-correlation technique (top) and average toroidal phase of the mode $p = 1$.*

velocity computed with the cross-correlation is consistent with the velocity deduced from the time behaviour of the phase.

All these techniques are applied to the inverted images of RFX-mode edge turbulence. In particular, the evolution of mode energies and toroidal velocity are evaluated with high-time resolution, and allow to study fast phenomena. At the same time, as all the discharges can be Fourier inverted, statistical analysis of the velocity and energies are possible. All these results will be used in particular in chapter 6.

4.3 Improvement of the radial resolution

As described in section 3.4, to overcome the problem of the poor radial resolution of the tomographic inversion, a new radial fan has been added to the GPI. Only changing the geometry of the LoS, the same tomographic algorithm based on the 2D Fourier transform can be used. By now, only the simulation has been done and not the implementation on the experimental data. In figure 4.11 a Gaussian emitting pattern has been simulated, and then the tomographic algorithm (with the new radial fan) has been applied. The improvement added by these new 8 LoS is significant: in fact now, not only the toroidal dimension of the emitting structure has reconstructed, but also the radial dimension between the simulation and the reconstruction is in agreement. The broadening along the lateral fans reported in figure 4.3 has vanished, and we recover a good radial resolution of the diagnostic.

This simulation make us confident that with this radial fan it is possible to better the tomographic reconstruction of the edge turbulence, and that will be possible to make similar analysis of the ones described in section 4.2.3 also for the radial modes; in particular the average radial wavenumber of the edge turbulence and the radial velocity could be evaluated, with the radial profile of the toroidal

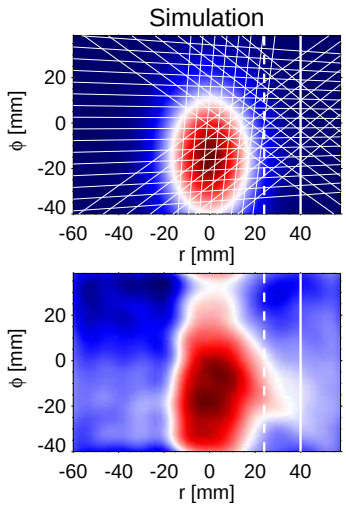

Figure 4.11: *Simulated gaussian light emission pattern (top) and its tomographic reconstruction with the 2D Fourier expansion (bottom). The lines of sight are visible in the top graph. Also the radial array has been used for the better radial reconstruction. The dashed vertical line is the radial position of the convolution of the graphite tiles of the firts wall; the continuos vertical line is the position of the vacuum vessel.*

velocity. With these data it will be possible to study the relation between the toroidal velocity shear and the radial dimension of the edge structures in all the plasma conditions, giving important information regarding the connection of the two phenomena [63].

Some resolvable problems of the application of the reconstruction with the radial array to the experimental data remain. In particular the main obstacle is the different normalisation between the radial fan and the other three fans of LoS. In fact, while the time signals of the central and lateral fans have similar *rms* value as they have similar path in the plasma edge, the radial fan has a completely different path and the *rms* changes for the different LoS decreasing from the most external to the most internal; then the optical system used to focalised the radial LoS in the He cloud (see sec. 3.4 and figure 3.11) is more complex then the one used for the lateral fan, and this decreases the signal as the solid angles are small and a little different for each radial chords. However we are working to the tomographic reconstruction in order to have as soon as possible the inversion with the radial fan, as the informations carried by it are necessary to improve the radial resolution, as previously underlined.

5

Experimental characterisation of edge turbulence in different devices

In this chapter spectral and statistical properties of the edge turbulence measured in RFP (TPE-RX and RFX-mod) and tokamak (NSTX) devices are described, together with a characterisation of the intermittent structures. It will be pointed out that even in different machines and in different plasma conditions, the edge turbulence has the same common properties: for this reason the edge turbulence seems to have some "universal" characteristics.

5.1 Spectral properties

Among the statistical properties of fluctuating signals, large information can be obtained from energy spectrum which is proportional to the second order momentum of the generic fluctuation $\delta\phi_\tau$:

$$\left\langle |\delta\phi_\tau|^2 \right\rangle \sim fE(f) \tag{5.1}$$

In this equation $E(f)$ is the spectral energy at the frequency $f \approx 1/\tau$. In figure 5.1, 5.2 and 5.3 the power spectra of emissivity signal from the GPI and of floating potential are shown for the three experiments studied.

First of all, the effectiveness of the sensitivity of the GPI system to local fluctuations can be inferred from figure 5.1 (a) for the TPE-RX experiment, comparing the power spectra of the emissivity signals obtained with and without gas puff. When the gas is puffed the average signal amplitude is higher by a factor 4, but this contribution comes mainly from low frequency range. On the other hand, for frequencies of interest for the turbulence (higher then 10 kHz in TPE-RX) the signal is more then ten times larger than the background emission.

Then, by analysing the different power spectra from different experiments, it is clear that these spectra, in the high frequency range, possess a broadband features

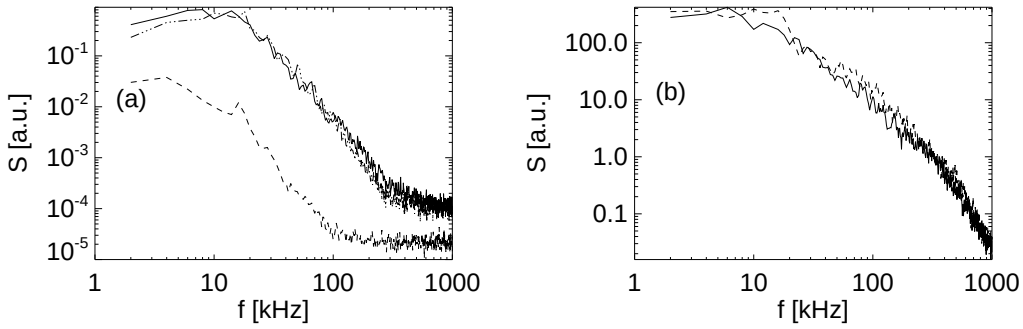

Figure 5.1: *Power spectra of D_α emission (a) measured by GPI without gas puffing (dashed line), with gas puffing (continuous line). Power spectra of floating potential V_f (b) with Langmuir probe inserted 16 mm into the plasma: without gas puffing (dashed line) and with gas puffing (continuous line). Signals refer to the TPE-RX experiment.*

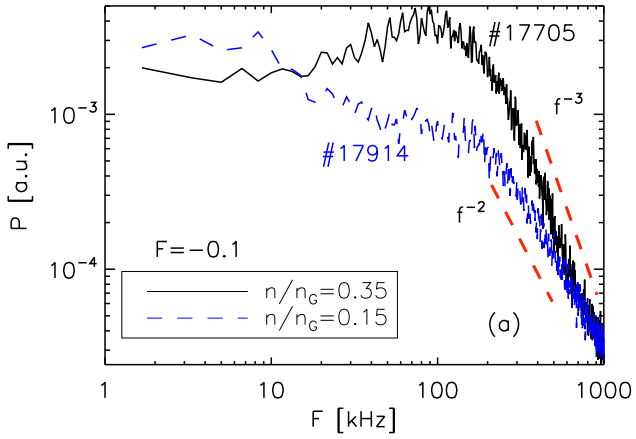

Figure 5.2: *Power spectra of GPI signal for two different normalised plasma densities in RFX-mod experiment.*

with a power-law decay $E(f) \sim f^{-\alpha}$, with $2 < \alpha < 4$, both for RFPs and tokamak. This non-trivial power-law decay exponent of the spectrum represents a qualitative indication of an energy exchange process between fluctuations at different scales [109].

Such power-law decay is detected in TPE-RX experiment both for the GPI signal (fig 5.1 (a)) and for floating potential one (fig 5.1 (b)); in RFX-mod both for high and low density discharges (fig 5.2); in NSTX (fig 5.3) both for L and H-mode plasma[1] (here, in the H-mode regime, two peaks at about 100 kHz appear in the spectrum: these have been previously quoted, and they occur in the Alvfen gap [110]).

[1]The Low (L) and High (H) modes are two different regimes obtained in tokamak devices. They will be defined and studied in chapter 7

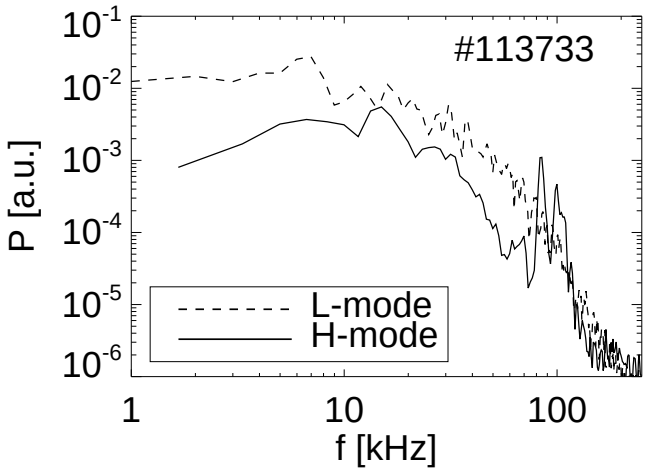

Figure 5.3: *Power spectra of GPI signal for L-mode (dashed line) and H-mode (continuous line) plasma for NSTX experiment.*

From the graphs it is visible that the regions of interest for the turbulence in frequency and the power law decay are different: in the TPE-RX experiment the power-law is detected in the region $30\,kHz < f < 300\,kHz$, in RFX-mod in the region $200\,kHz < f < 800\,kHz$ and in NSTX tokamak, for the L-mode, in $40\,kHz < f < 200\,kHz$. The detailed results for the different power-law exponents are described in table 5.1. Here the result regarding the H-mode of NSTX is not reported, since the two peaks in the power spectrum do not allow to make a good fit. This means that in tokamak and RFPs the time-scales of edge turbulence are different, and we care about it in the following sections.

From table 5.1 it is clear that the turbulence properties depend also on the electron density, as we will see better in the next paragraphs. Normally the electron density in fusion experiments is measured as a fraction of the *Greenwald* density n_G, defined as [111]:

$$n_G[m^{-3}] = 1 \times 10^{20} \frac{I_p[MA]}{\pi a^2[m^2]} \tag{5.2}$$

Experiment	Decay Exponent	Frequency range (kHz)
TPE-RX (GPI)	-2.7 ± 0.04	$30 < f < 300$
RFX-mod (GPI $n/n_G = 0.35$)	-3.1 ± 0.05	$200 < f < 800$
RFX-mod (GPI $n/n_G = 0.15$)	-2.1 ± 0.03	$200 < f < 800$
NSTX (GPI L-mode)	-5.6 ± 0.08	$40 < f < 200$
TPE-RX (V_f)	-2.2 ± 0.02	$30 < f < 400$

Table 5.1: *Decay exponent for the power spectra of the different devices analysed.*

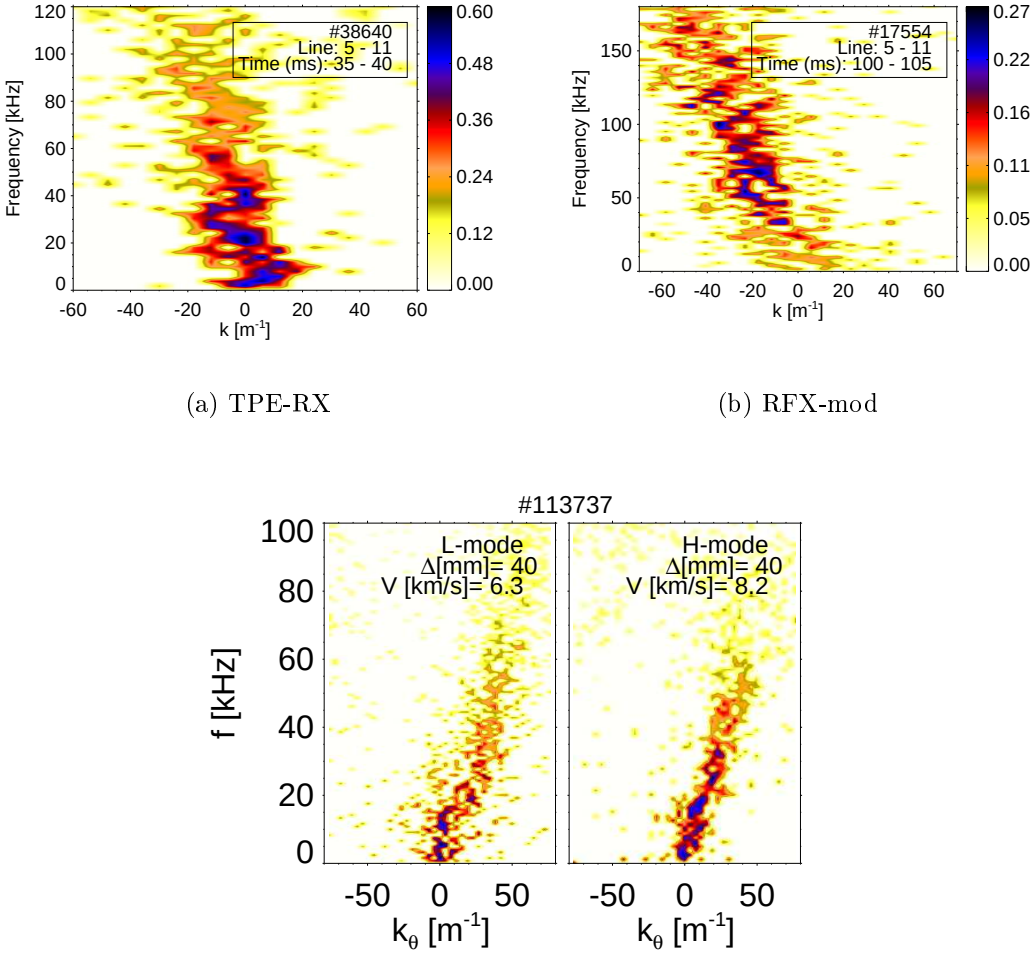

(a) TPE-RX

(b) RFX-mod

(c) NSTX

Figure 5.4: *Spectral density of the GPI fluctuations in the* $(k_\perp, f)$ *plane for TPE-RX (a), RFX-mod (b) and NSTX (c).* $k_\perp$ *is the wavenumber in the plane perpendicular to the main magnetic field.*

where a is the minor radius of the experiment and I_P the plasma current. This is the density limit for the plasma experiments above which a major disruption occurs. This limit was investigated in a large number of toroidal devices, and for a comprehensive and recent review on this topic see ref. [112]. From the various experimental data, the density limit would seem to be linked with the edge and SOL physics [113, 99]. For all these reasons normally the electron density is expressed as n/n_G.

Another characteristic that is found to be similar in different devices, and in particular in the three experiments analysed here, is the power spectral density $S(k, f)$, where k is the perpendicular wave number (toroidal in RFPs and poloidal in tokamaks). The result of this analysis is shown in figure 5.4.

The $S(k, f)$ power spectral density is evaluated according to the two-point spectral analysis, based on the method described in [90] and introduced in section 4.1.1. For the GPI used in TPE-RX and RFX-mod the signals corresponding to two lines of sight are considered as two measurements centred on the respective focal points. In NSTX two points of the poloidal array are used. Both for the RFPs and tokamak most of the power content is due to fluctuations with $|k| < 20m^{-1}$; instead, as mentioned above, the frequency ranges are different.
Besides, the three $S(k, f)$ show broadband features both in frequency and in wavenumber space, in analogy with the results described in [114] for ASDEX tokamak and in [115] for the W7-AS stellerator.

Another similarity that can be pointed out is the quasi-linear relation between frequency and $k_\perp$ indicating a propagation of the edge fluctuations perpendicularly to the main magnetic field; moreover the velocity is directed along the $\mathbf{E} \times \mathbf{B}$ flow. From this average linear trend a mean phase velocity $v_\perp$ can be evaluated; for the two RFP machines we obtain $|v_\perp| \sim 20 - 30 km/s$ and for NSTX $|v_\perp| \sim 6 - 8 km/s$. In NSTX this analysis is made for both L-mode and H-mode discharges, and the perpendicular velocity of fluctuations does not change appreciably (in the radial position of the poloidal array, about $10\,mm$ outside the separatrix).

A complementary way to evaluate the perpendicular velocity of edge fluctuations is described in the next paragraph.

5.2 Perpendicular velocity of fluctuations

A method based on the cross-correlation technique is developed to study the time behaviour of the perpendicular velocity of propagation of the edge fluctuations, and applied to the three different experiments. As the GPI gives a set of spatially distributed measurements of the same quantity, the cross-correlation function provides information related to the average velocity of propagation of fluctuations of that quantity. For two measurements located at distance $\mathbf{d}$, the time lag $\Delta t(\mathbf{d})$ at which the first maximum of the cross-correlation function occurs gives an indication of the average time required for fluctuations to cover the distance between the two measurement points. The propagation velocity v multiplied by Δt equals the projection of the distance between the measurement points along the velocity:

$$v\,\Delta t(\mathbf{d}) = \mathbf{d} \cdot \left(\frac{\mathbf{v}}{v}\right) \tag{5.3}$$

Defining $\mathbf{w} = \mathbf{v}/v^2$, equation 5.3 can be re-written as:

$$\Delta t(\mathbf{d}) = \mathbf{d} \cdot \mathbf{w} \tag{5.4}$$

Hence the determination of the propagation velocity turns into the problem of the least-squares estimation of the components of the vector $\mathbf{w}$. This amounts to performing a linear fit to the data of the time delays, corresponding to each pair of measurements, as a function of their distance from a reference point. Finally, the components of the velocity are recovered using:

$$\mathbf{v} = \mathbf{w}/w^2 \tag{5.5}$$

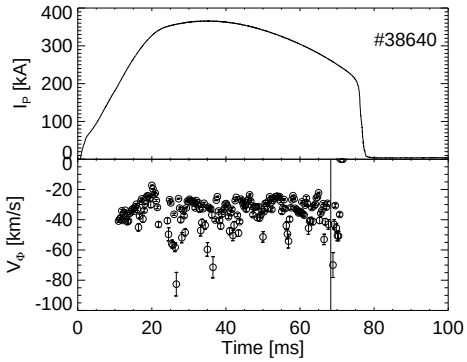

(a) TPE-RX: Plasma current and perpendicular velocity

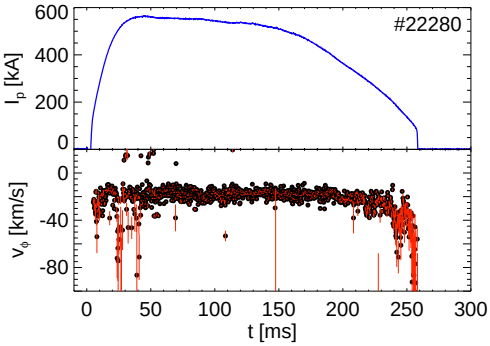

(b) RFX-mod: Plasma current and perpendicular velocity

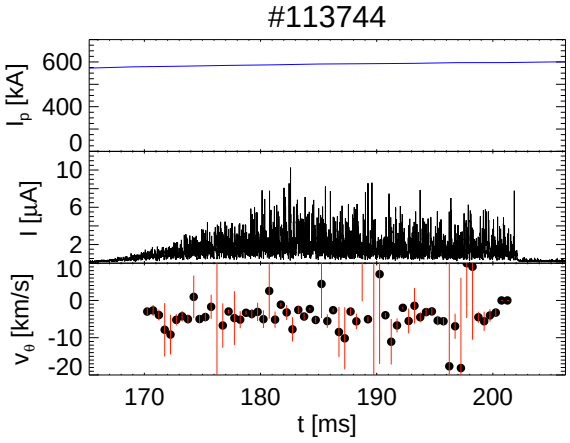

(c) NSTX: Plasma current, GPI signal and perpendicular velocity

Figure 5.5: *Time behaviour of the perpendicular velocity of the edge fluctuations in TPE-RX (a), RFX-mod (b) and NSTX (c).*

The statistical error on the resulting velocity can be estimated by propagating to $\mathbf{w}$ of the error of Δt and hence propagating to the velocity (see ref. [94]). This technique allows to obtain a time-resolved velocity.

In figure 5.5 the time evolution of the perpendicular velocity of the fluctuations in the plasma edge is shown. For TPE-RX and RFX-mod the velocity is along the toroidal direction and it is measured using the central fan of the GPI. In NSTX the velocity is along the poloidal direction and it is measured with the poloidal array. This technique allows to obtain a time-resolved velocity. The resolution is $0.2\,ms$ for the GPI installed in the RFPs and $0.5\,ms$ for NSTX. This is due to the different time scales involved in turbulence as mentioned in the previous section.

In fig. 5.5 typical standard discharges are shown for the three machines. The velocity is about $-20 \div -40 km/s$ for the RFP experiments and about $-4 \div -5 km/s$ for NSTX. These velocities are along the $\mathbf{E} \times \mathbf{B}$ flow (opposite to the plasma current) and in RFX-mod experiment, where also electrostatic probes are used, the two velocities are in agreement [116].

5.3 Statistical properties: intermittency

Applying statistical techniques to plasma turbulence [37] is an appropriate approach to capture some of the underlying physical mechanisms, and it is a powerful tool to study the universal aspect of the turbulence in different devices and in different plasma conditions. In fact, a remarkable feature of the plasma edge turbulence is that many of the statistical properties appear to be universal, i.e. common to all plasma devices, regardless of their magnetic configurations (tokamaks, stellerators, reversed field pinches) or geometrical configuration (toroidal or linear devices) [117, 118]: evidence of a common physical mechanism driving this turbulence. One way to study the universality of the statistical properties for the plasma edge fluctuations is to characterise their Probability Density Function (PDF). This approach is widely used, and in particular it was demonstrated that the PDFs of plasma edge fluctuations are non-Gaussian for many devices (see for examples references [117, 118, 119, 120, 121, 122], even if this list do not have the ambition to be complete).
In this section the statistical properties of the edge turbulence are studied by analysing the PDFs of the GPI signals and looking for intermittency (defined in sec. 2.8). This property is directly connected with the breaking of self-similarity and naturally reflects upon the PDF of the fluctuations; it can be quantified by looking at the dependence of the statistical properties of the fluctuations on the time scales. In particular, the measurements of turbulent fields manifest significant non-Gaussian tails for the shorter time scales of the inertial range. The presence of intermittency on plasma edge was found for the first time in ADITYA tokamak [123] and later detected in various magnetic configurations. The decay of the power spectrum different from f^{-2}, as reported for the experiments in this thesis, usually suggests the presence of intermittency, although not being a sufficient condition.

Let us consider the generic turbulent field $\delta\Phi_\tau$ which scales as:

$$\delta\Phi_\tau \sim \tau^h \qquad \text{with a unique value of } h \tag{5.6}$$

A generic scale transformation $\tau \to \tau' = \lambda\tau$ yields to the relation:

$$\delta\Phi_{\lambda\tau} \sim \lambda^h \delta\Phi_\tau \tag{5.7}$$

For a turbulent fluid this property has to be interpreted as an equality in law [33], i.e. it is satisfied by the corresponding probability density function:

$$pdf\left(\delta\Phi_{\lambda\tau}\right) = pdf\left(\lambda^h \delta\Phi_\tau\right) \tag{5.8}$$

Let us introduce the standard variables:

$$Z_\tau = \frac{\delta\Phi_\tau - \langle\delta\Phi_\tau\rangle}{\sigma_\tau} \tag{5.9}$$

where σ is the standard deviation. In the following we will show that if the Hölder exponent (h in eq. 5.7) is unique, the probability density function of the standard variables Z_τ collapses to a unique scale-invariant PDF [124]. Let us introduce the variables:

$$x_1 = \delta\Phi_{\lambda\tau} \tag{5.10}$$

$$x_2 = \delta\Phi_\tau \tag{5.11}$$

and the corresponding probability density function $P_1(x_1)$ and $P_2(x_2)$. Let us change the variables according to $y = \lambda^h\delta\Phi_\tau = \lambda^h x_2$. Equation 5.8 implies that:

$$P_1(x_1) = G(y) \tag{5.12}$$

where $G(y)$ is the PDF of the variable y. The probability measure $d\mu(y) = G(y)dy$ represents the probability that the variables reside in the interval $[y, y+dy]$. According to measure theory the probability measure has to be conserved:

$$G(y)dy = P_2(x_2)dx_2 \tag{5.13}$$

so that for a constant value of h it is straightforward to show:

$$G(y) = \frac{P_2(x_2)}{|dy/dx_2|} = \frac{P_2(x_2)}{\lambda^h} \tag{5.14}$$

and consequently considering equation 5.12:

$$P_2(x_2) = P_1(x_1)\lambda^h \tag{5.15}$$

We can use the previous results to write the n-momentum of variables x_1 as a function of the n-momentum of variables x_2 where $x_1 = \lambda^h x_2$:

$$\langle x_1^n\rangle = \int x_1^n P_1(x_1)dx_1 = \int \lambda^{nh} x_2^n \lambda^{-h} P_2(x_2)\lambda^h dx_2 = \lambda^{nh}\langle x_2^n\rangle \tag{5.16}$$

For the standard deviation the previous equation yields the following:

$$\sigma_1^2 = \lambda^{2h}\sigma_2^2 \tag{5.17}$$

Introducing the standard variables defined in 5.9 $Z_i = \frac{x_i - \langle x_i\rangle}{\sigma_i}$ with $i = 1, 2$ the corresponding PDF may be written as:

$$P_i(Z_i) = P_i(x_i)\sigma_i \tag{5.18}$$

so that:

$$P_1(Z_1) = P_1(x_1)\sigma_1 = \frac{P_2(x_2)}{\lambda^h}\sigma_1 = P_2(x_2)\sigma_2 = P_2(Z_2) \tag{5.19}$$

Consequently the scaling of normalised fluctuations provides information about the self-similarity or the intermittency of the turbulent field.
In order to compute the PDF of the edge fluctuations as a function of the time scale of the fluctuations themselves, the continuous wavelet transform $w(t,\tau)$ of the GPI signal I has been evaluated as (see sec. 4.1.2):

$$w(t,\tau) = \frac{1}{\tau}\int I(s)W\left(\frac{s-t}{\tau}\right)ds \tag{5.20}$$

These coefficients give a decomposition of the signal I at the scale τ as a function of the time t. The so-called "Mexican Hat" was used as the mother wavelet $W(t)$ [91].

As wavelet coefficients give a measure of the characteristic fluctuations as a function of time and scale [87], the PDF of normalised wavelet coefficients gives the same information of the PDF of the fluctuations themselves. The normalised wavelet coefficients $C(t,\tau)$ are defined as:

$$C(t,\tau) = \frac{w(t,\tau) - \langle w(t,\tau)\rangle}{\sigma_\tau} \tag{5.21}$$

where the average value $\langle w(t,\tau)\rangle$ and the standard deviation σ_τ are calculated for all the wavelet coefficients relative to scale τ.

The PDFs of the normalised wavelet coefficients are obtained by dividing the signal $C(t,\tau)$ in 30 bins of width D. The probability density for each bin will be:

$$P(C) = \frac{n(C)}{N_{tot}D} \tag{5.22}$$

where $n(C)$ is the number of coefficients in the bin's interval, N_{tot} is the total number of coefficients. The corresponding histogram will be the normalised probability density of the wavelet coefficients. The error bars can be computed by assuming a Poisson distribution for the number of counts in the i-th bin, $\Delta n = \sqrt{n}$. The error on $P(C)$ will be:

$$\Delta P(C) = \frac{\Delta n}{N_{tot}D} = \frac{\sqrt{n}}{N_{tot}D} = \sqrt{\frac{P}{N_{tot}D}} \tag{5.23}$$

The PDFs of wavelet coefficients for the light emission fluctuations are shown in figure 5.6 for the three experiments. The data are presented in a semi-logarithmic scale and the time scale indicated is the corresponding Fourier scale $f \sim 1/\tau$. The behaviour of the three experiments are similar: for all the signals the absence of self similarity is observed, as the PDFs of different time scales do not collapse to a single shape. The distribution of the fluctuations tends to develop strong non-Gaussian tails at small time scales and to recover a shape similar to a Gaussian at large ones. This is equivalent to state that at small time scales fluctuations have a higher probability to occur if compared to a Normal distribution.

To quantify this variation, the fourth moment (flatness, F) of the PDF of the normalised wavelet coefficients can be evaluated as a function of time scales. It is defined as:

$$F = \frac{\langle C(t,\tau)^4\rangle}{\langle C(t,\tau)^2\rangle^2} \tag{5.24}$$

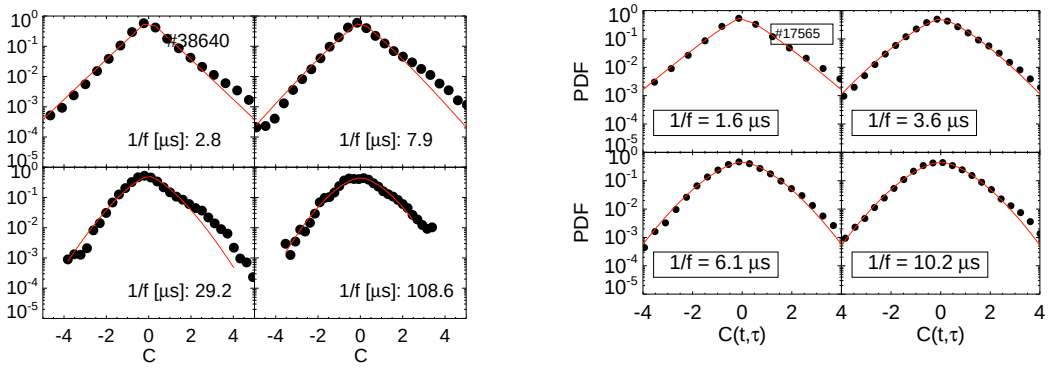

(a) TPE-RX

(b) RFX-mod

(c) NSTX

Figure 5.6: *Probability density function of wavelet coefficients for light emission fluctuations at different time scales measured in TPE-RX (a), RFX-mod (b) and NSTX (c). The solid line in the first two graphs is the result of stretched exponential fit.*

It measures the weight of the tail of the distribution with respect to the mean. For a Gaussian distribution $F = 3$.

In figure 5.7, the scaling of the flatness of the PDFs as a function of time scales is shown for the three machines.

In order to evaluate F, in the RFP experiments we computed the flatness of the PDF for the 16 chords of the central fan of the GPI; in the graph, for every time scale the mean is reported, and the error bars are the rms. In NSTX the poloidal array that is positioned near the separatrix is used. For the different experiments, the flatness has a value of 3 (=Gaussian) for high time scales, and increases for small ones. This characteristic behaviour is observed both for RFP and tokamak experiments, suggesting that the statistical properties of the fluctuations depend on the time scale of the fluctuations themselves and are independent from the

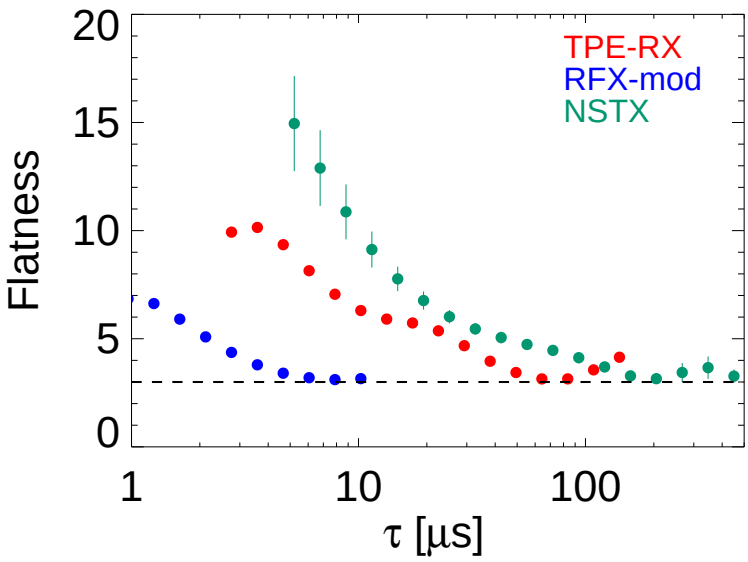

Figure 5.7: *Flatness of GPI fluctuations as a function of time scales for TPE-RX (red), RFX-mod (blue) and NSTX (dark green). In NSTX experiment the Flatness is referred to a position near the separatrix. The dashed line is F=3, the Gaussian.*

magnetic configuration. Looking at fig. 5.7, it is clear that, as pointed out in the previous sections, the characteristic frequencies of the turbulence are different between the RFPs and the tokamak. Intermittency is recognised from 3 to 100μs in TPE-RX, from 1 to 10μs in RFX-mod and from 5 to 500μs in NSTX. These ranges roughly correspond to the frequency ranges where a power-law decay of the power spectrum is recognised (figs. 5.1, 5.2, 5.3).

In TPE-RX, together with the optical diagnostic, also the array of Langmuir probes was used measuring the floating potential in different radial positions. So, a complementary piece of information can be obtained by their statistical analysis, and the results are shown in figure 5.8. On the top the flatness of the floating potential fluctuations is shown as a function of the time scale for two different radial positions of the probe, and the behaviour is very similar to the one of the GPI. Another way to study the intermittent behaviour is to fit the PDF with a stretched exponential fit:

$$f(x) = A \exp(-\beta |x|^{\gamma}) \tag{5.25}$$

where β and γ are real coefficients. The parameter β is related to the width while γ is related to the shape of the distribution. If $\gamma = 2$ we have a Gaussian distribution, while for $\gamma < 2$ a stretched exponential shape is recovered. In figure 5.8 at bottom, the scaling of the exponent γ as a function of the time scale of floating potential measurement is reported. The scaling behaviour of $\gamma(\tau)$ reflects the absence of self-similarity of the turbulence. Similar results are reported for the electrostatic turbulence of T2R RFP experiment [125], for the magnetic fluctuations

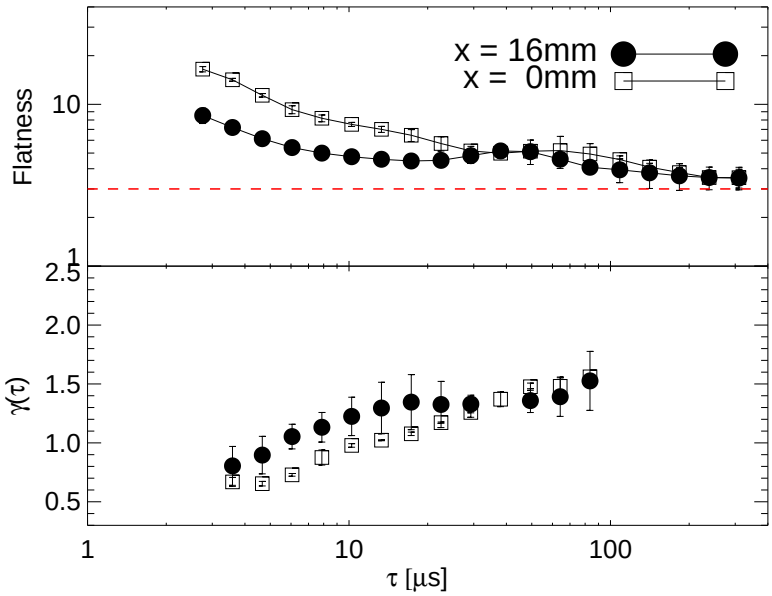

Figure 5.8: *Scaling of flatness and stretched exponential parameter γ as a function of time scale τ for the floating potential measured in two different radial position at TPE-RX. The red dashed line is the Gaussian value of the flatness.*

of RFX [126] and for density fluctuations of Tore Supra [127].

By comparing the results obtained here both for tokamak and RFPs, the intermittent behaviour of the edge turbulence, and in particular the fact that the PDF of the plasma edge fluctuations depends on the scale of the fluctuations themselves, seems to be a "universal" property. This universality is supported by similar results reported also for other experiments.

This peculiar behaviour of the PDFs can be characterised through the generation of "structures" at all scales [88, 128, 129]. These structures can be viewed as coherent localised events within the sea of Gaussian turbulence.

5.4 Statistical properties: universality

All the statistical analyses just described suggest a common behaviour of the statistical properties of the edge turbulence in all the different devices studied in this thesis. In order to strengthen this picture, the third order moment (Skewness) and the fourth order moment (Flatness) of the distribution of the GPI signals collected in the edges of the three experiments are evaluated, and we plotted the Flatness as a function of the Skewness in figure 5.9.

For all the GPI signals, Flatness and Skewness are evaluated for every time portion of 10 ms. For RFX-mod there are 40781 points, from 2167 different plasma discharges. This great amount of data allows a good statistics, as visible from fig. 5.9. For RFX-mod only the central chord of the central fan of the GPI is used (using another chord does not change the behaviour of the curve). Also for

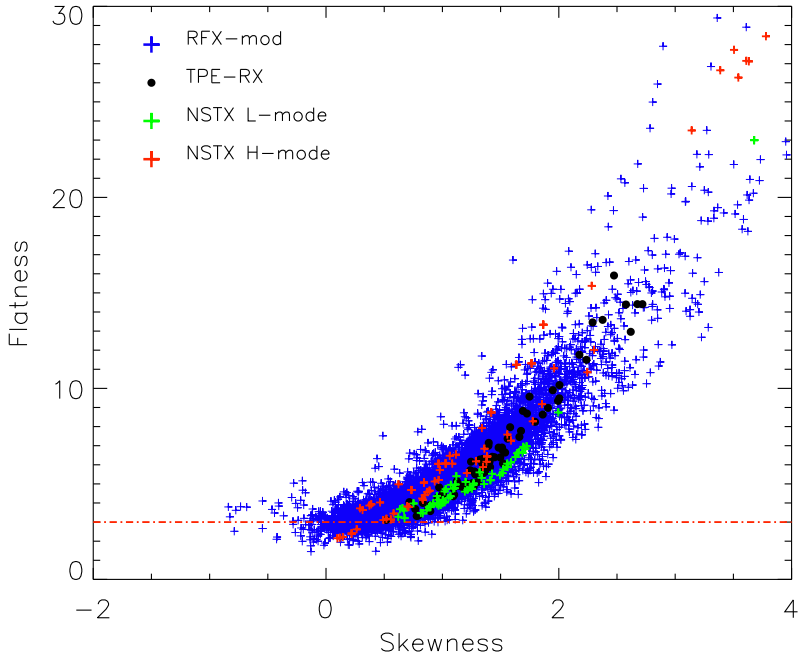

Figure 5.9: *Flatness Vs Skewness for the GPI data of RFX-mod (blue crosses), TPE-RX (black circles), NSTX in L-mode (green crosses) and NSTX in H-mode (red crosses). The horizontal red line represents F=3, the Gaussian value of the Flatness.*

TPE-RX the same GPI chord has been used; instead for NSTX all the 10 different chords of the two arrays are considered, both during the L-mode and the H-mode. Figure 5.9 shows that Flatness and Skewness lie in a common curve for all the experiments, independently from the plasma conditions: in fact, we remind that in the curve there are points from high plasma current (up to 1 MA for RFX-mod), low plasma current (200-300 kA for both RFX-mod and TPE-RX), different densities and different magnetic configurations.

This result is very similar to what obtained in TORPEX machine with Langmuir probes [122]. In that paper it was found that Flatness and Skewness are characterised by a quadratic relation $F = \alpha S^2 + \beta$. Also for the RFX-mod data the two quantities could be related by a quadratic relation, and the fit gives: $F = (2.98 \pm 0.01) + (1.66 \pm 0.01)S^2$. The quadratic relation between F and S is valid for a large set of PDF families: in the cited paper by Labit [122], the quadratic relation has been explained with a Beta distribution, that is a curve often found in modeling in a variety of fields [122]. We will discuss the compatibility of the Beta distribution with our data later; now we introduce a new PDF that can explain the behaviour of our GPI data.

All the edge fluctuation data collected by the GPI in the three experiments display PDFs whose tails, at large values of the signal, are approximately exponential. In RFX-mod it has been attempted to fit the PDFs using Gamma functions as done in [119]. These distributions are versatile, and satisfy an important constrain:

they are defined only for positive values, that is the proper peculiarity of the GPI signals.

The fit with just one Gamma function is not satisfactory for all the plasma discharges. However, in [121] we attempted a generalization with a linear combination of *two* Gamma functions and the fits turned out to be fairly satisfactory:

$$\begin{aligned} P(n) = C_< \frac{(\beta_< N_<)^{N_<}}{\Gamma(N_<)} n^{N_<-1} \exp\left(-\beta_< N_< n\right) + \\ + C_> \frac{(\beta_> N_>)^{N_>}}{\Gamma(N_>)} n^{N_>-1} \exp\left(-\beta_> N_> n\right) \end{aligned} \tag{5.26}$$

where n is the GPI signal, $\Gamma(N)$ is the mathematical function Gamma, $\Gamma(z) = \int_0^\infty t^{z-1} \exp(-t) dt$ introduced for normalisation purposes, $C_<$ and $C_>$ are positive numbers with $C_< + C_> = 1$. The subscripts "$< >$" have been chosen to stress the order relation between the two parameters N: the $<$ symbol labels the triple (N, β, C) with the lower N. In figure 5.10 the experimental PDF of four different plasma discharges of RFX-mod are shown along with the result of the fit with the two Gamma functions.

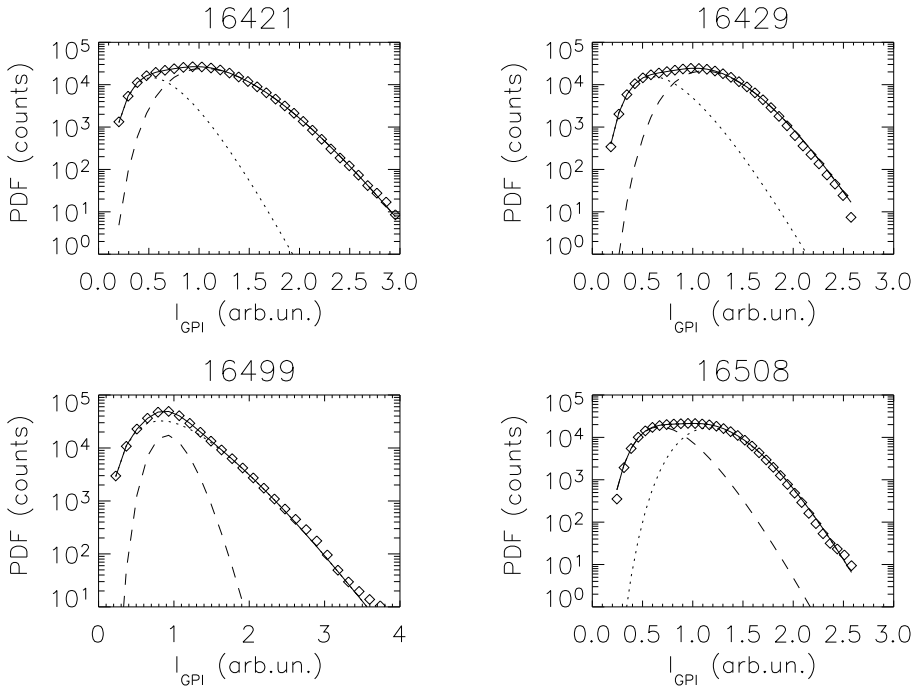

Figure 5.10: *Examples of PDFs of GPI signals for four RFX-mod discharges. Symbols: GPI data; solid curve: best fit from a linear combination of the two Gamma functions (eq. 5.26). The two individual components are shown as dashed and dotted curves.*

An inspection of the literature shows that similar results are not confined to RFX-mod: in ref [130] the data of Tore Supra have been interpreted in terms of a Gaussian contribution plus an exponential one, and a similar double structure was found also in PISCES [131, 132], TORPEX [133] and VINETA [134] devices.

We guess therefore that there is a substantial amount of evidence in the literature in favour of the hypothesis that experimental PDFs could be fitted by the sum of *two* contributions. Empirically it is found that these two contributions may be quantified reasonably well using Gamma distributions with different weights and parameters. The two functions should stand for the contribution from two independent subsystems.

In order to show that two Gamma functions can reproduce the experimental PDFs of the GPI data in many different plasma conditions, figure 5.11 reports for RFX-mod the flatness as a function of the skewness (red circles) together with the same quantity for the two Gamma functions of equation 5.26 (black crosses).

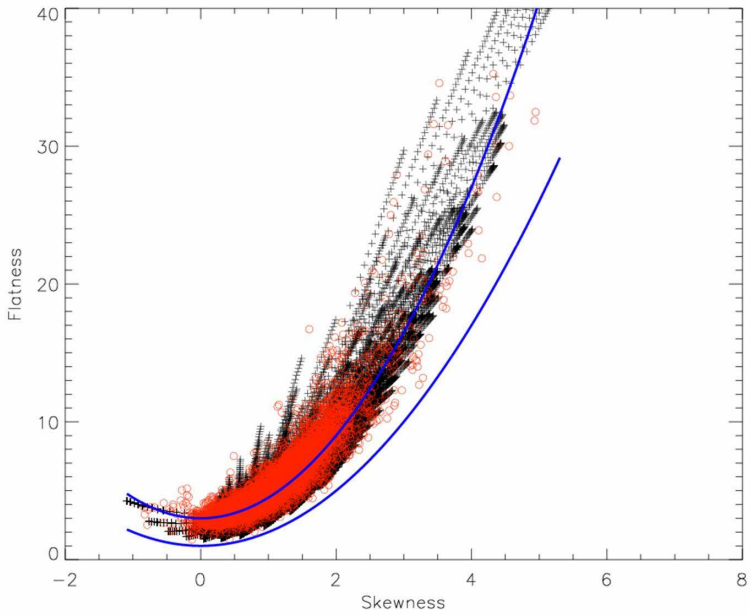

Figure 5.11: *Flatness as a function of the skewness for experimental data of RFX-mod (red circles), and the same quantity computed for the two Gamma functions of equation 5.26 (black crosses). Flatness and Skewness of the beta functions should occupy the region between the two blue lines.*

To obtain the "theoretical" points of figure 5.11, we have computed the Flatness and the Skewness of the two Gamma functions of equation 5.26 varying the parameters $0.5 \leq \beta \leq 1.1$, $0.2 \leq C \leq 0.9$, $1 \leq N_< \leq 20$ and $N_< \leq N_> \leq 31$. The data collected by the GPI in the edge region of RFX-mod is superimposed to the curve related to the two Gamma functions. Since also the data from the plasma edge of TPE-RX and NSTX lay in the same region (see fig. 5.9), we can suppose that the two Gamma functions represent the PDFs of the edge plasma fluctuations for all three experiments analysed.

In the same figure it is shown also the region of the plane Skewness-Flatness that represents the Beta function. In fact, for a Beta function $1 + S^2 \leq F \leq 3 + 1.5S^2$, and these two curves are represented in blue in figure 5.11. The experimental points are not limited to the area enclosed between these two curves, and so we can infer that the Beta distribution does not describe the data.

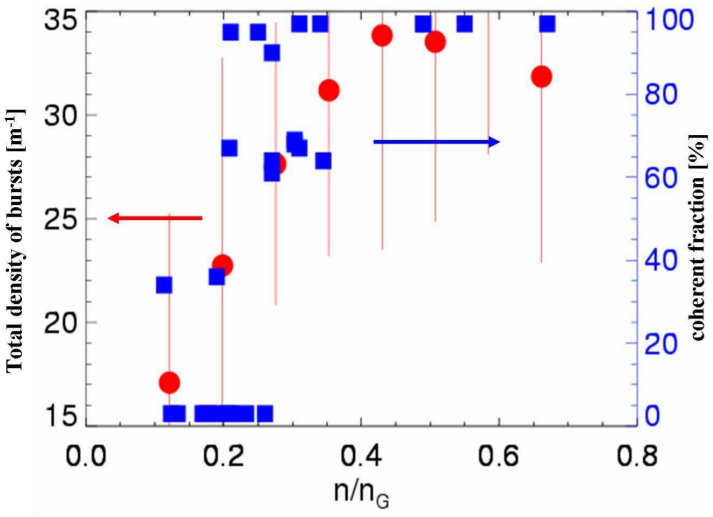

Figure 5.12: *Linear density of burst N_s (red circles) detected in the GPI signal of RFX-mod and fraction of the PDF due to the low-N Gamma function contribution (blue squares) as a function of the normalised electron density.*

Hence, it has been shown that the PDF of each GPI data of the edge plasma fluctuations, independently from the magnetic configurations (tokamak or RFP) and plasma conditions, can be described with two Gamma functions, with a suitable choice of the parameters (β, N, C). In reference [121] we attempt to provide a possible physical explanation of this picture. In particular it is possible to postulate the $N_>$ contribution as due to the uncorrelated background fluctuations, while the $N_<$ one is related to the coherent part of the fluctuations. One evidence toward this picture is that improved confinement regimes in RFX-mod appear often related at the edge to a reduction of the content of the $N_<$ fluctuations (see ref. [121]).

To enforce the universality of the two Gamma PDF that can describe the edge fluctuations of RFX-mod, TPE-RX and NSTX experiments, recently it has been shown that this model can accurately describe also the edge fluctuations of Alcator C-mod tokamak measured with the GPI [135].

A convincing test that the $N_<$ contribution of the Gamma function is related to the coherent part of the fluctuations comes from the explicit comparison with the linear density of intermittent bursts detected in the GPI signal reported in figure 5.12 (the method used to identify the bursts is described in the next section).

The coherent fraction is conventionally set to 0 when both $N_< > 10$ and $N_> > 10$, and when both $N_< < 10$ and $N_> < 10$ the coherent fraction is set to 1.

From the figure a fairly good correlation between the coherent fraction of the signal measured by the two Gamma analysis and the linear density of bursts N_s can be seen. In figure 5.12 the two quantities are plotted as a function of the normalised electron density n/n_G, suggesting that the coherent turbulence plays a more important role for high density discharges than for the low ones.

5.5 Intermittent structures

As stated in the previous paragraph the change of shape of the PDF of increments of turbulent signal can be associated with small scale intermittency which basically consists of an uneven distribution of turbulent energy dissipation. Generally in fluid turbulence intermittency is related to the presence of vortical structures. So we can suppose that intermittency phenomenon as detected from the GPI measurements in the three machines studied is correlated with intense fluctuations caused for example by a sort of "structure" which passes through the GPI field of view [136, 137, 138, 139].

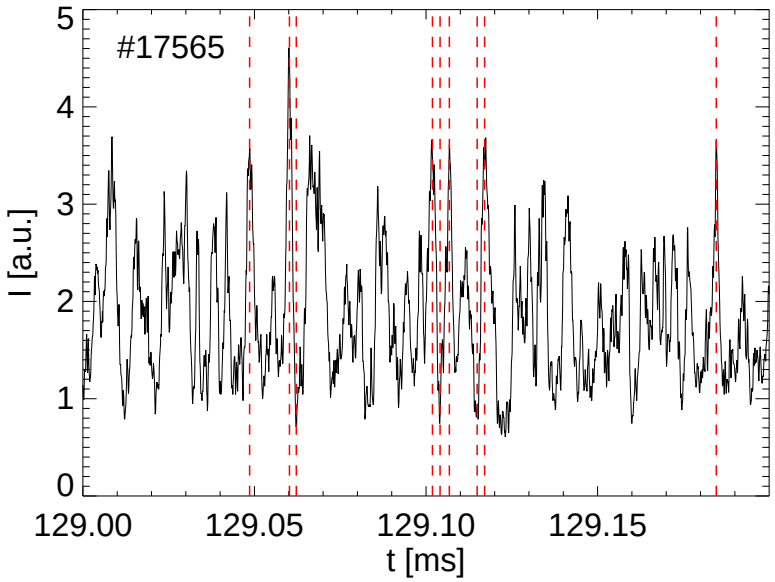

Figure 5.13: *Example of identification of intermittent events in the GPI signal. The vertical dashed red lines indicate the time occurrence of an intermittent events at a scale $\tau = 4\,\mu s$. The method allows to detect positive (peaks) and negative (valleys) events. The figure refers to a signal collected from RFX-mod.*

To identify in time t and scale τ the occurrence of strong events in the GPI time series raising the PDF tails, a method based on the wavelet transform introduced by Farge [88] (see also references [128, 129]) is used. An unambiguous characterisation of the local activity present in the signal at each scale τ and time t can be given by the *local intermittency measure* (LIM) defined as:

$$l(t,\tau) = \frac{C(t,\tau)^2}{\langle C(t,\tau)^2 \rangle} \tag{5.27}$$

where $\langle \dots \rangle$ indicates a time average and $C(t,\tau)$ are the normalised wavelet coefficients of the signal. An intermittent event yields a large value of $l(t,\tau)$, as it corresponds to an energy fluctuation larger that the mean value at the scale τ. The method divides the set of wavelet coefficients into two orthogonal sets:

$$\{C(t,\tau)\} = \{C_e(t,\tau)\} \oplus \{C_g(t,\tau)\} \tag{5.28}$$

one, $\{C_e(t,\tau)\}$, relative to the events and the other, $\{C_g(t,\tau)\}$, relative to the Gaussian background. The distinction is made through an iterative process which identifies a threshold $S(\tau)$ on the LIM $l(t,\tau)$ for each scale. All coefficients for which the LIM is above $S(\tau)$ are considered as part of $\{C_e(t,\tau)\}$, whereas the others belong to $\{C_g(t,\tau)\}$. The appropriate threshold value is found as that for which the flatness

$$F(\tau) = \frac{\langle C_g(t,\tau)^4 \rangle}{\langle C_g(t,\tau)^2 \rangle^2} = 3 \tag{5.29}$$

In this way the gaussianity of the coefficients belonging to $\{C_g(t,\tau)\}$ is insured. Using this method it is possible to identify the temporal occurrence of intermittent events. In order to avoid counting twice the same structure as a result of the redundancy of the continuous wavelet transform, an intermittent event is assumed to occur when $l(t,\tau) > S(\tau)$ and simultaneously $l(t,\tau)$ has a local maximum in time. Figure 5.13 gives an example of the GPI signal collected from RFX-mod with the intermittent events detected with the LIM method: the vertical lines indicate the intermittent bursts with $\tau = 4\,\mu s$.

5.5.1 Characterisation of the structures in TPE-RX and RFX-mod

In this paragraph the intermittent structures detected in the two RFP experiments with the LIM method are studied.

The GPI system installed in TPE-RX and RFX-mod provides very good spatial resolution and allows for the first time on an RFP the direct study of the spatial features of intermittent events. Here the analysis is carried out on the basis of the conditional average technique (CA), that is widely used in plasma physics for studying the edge structures (see for example [136, 140]). According to the CA technique a reference signal $I(s_0,t)$ is measured at a fixed position s_0. Measurements performed simultaneously at w different positions $I(s_{\{1,2,\ldots,w\}},t)$ are collected at each time t_i when a prescribed condition on the reference signal $I(s_0,t)$ is met; these measurements form an ensemble, and their average gives the mean shape $I(s)$. Here we used as $I(s_0,t)$ the signal of the central chord of the central fan of the GPI; as prescribed condition the presence of an intermittent event on it, detected with the LIM method; as $I(s_{\{1,2,\ldots,w\}},t)$ all the 16 LoS of the central fan. The conditional average is then computed using the 16 LoS of the central fan of the GPI toroidally spaced, and it yields the typical toroidal pattern of the edge structures. The result for peaks with positive amplitude at two significant wavelet scales is shown in figure 5.14 for TPE-RX and in fig. 5.15 for RFX-mod. Since all the signals are sampled simultaneously, no frozen turbulence hypothesis is required.

Both for TPE-RX and RFX-mod, the structures detected on the shorter time scale have a smaller toroidal extent than the structures detected at the larger time scale. The time scales plotted in the two figures are chosen by considering the

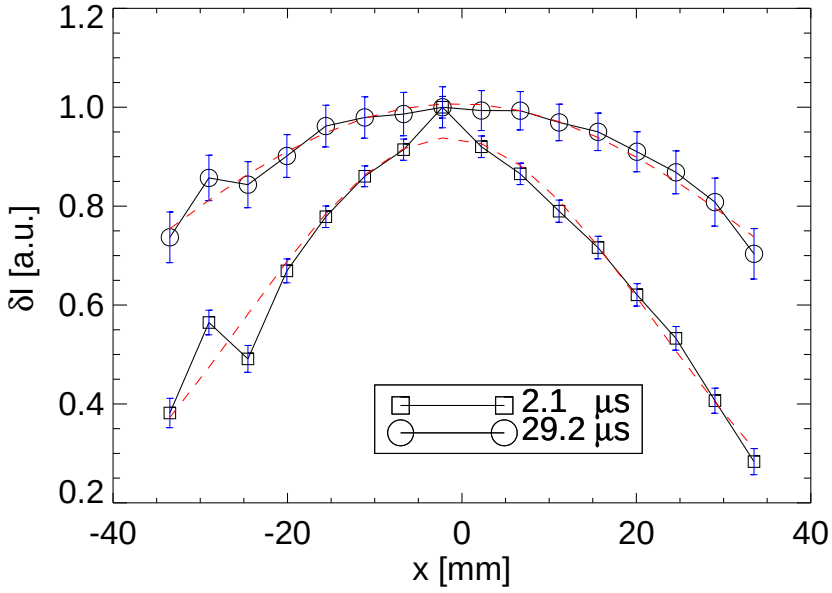

Figure 5.14: *Typical toroidal patterns of positive intermittent structures for TPE-RX at two different time scales τ, obtained by conditional average. The dashed red lines are the corresponding Gaussian best fit.*

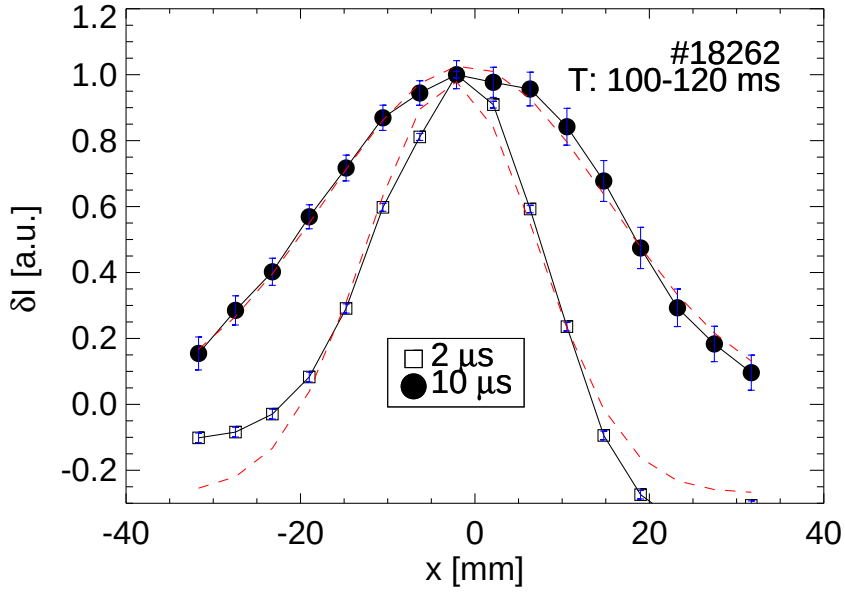

Figure 5.15: *Typical toroidal patterns of positive intermittent structures for RFX-mod at two different time scales τ, obtained by conditional average. The dashed red lines are the corresponding Gaussian best fit.*

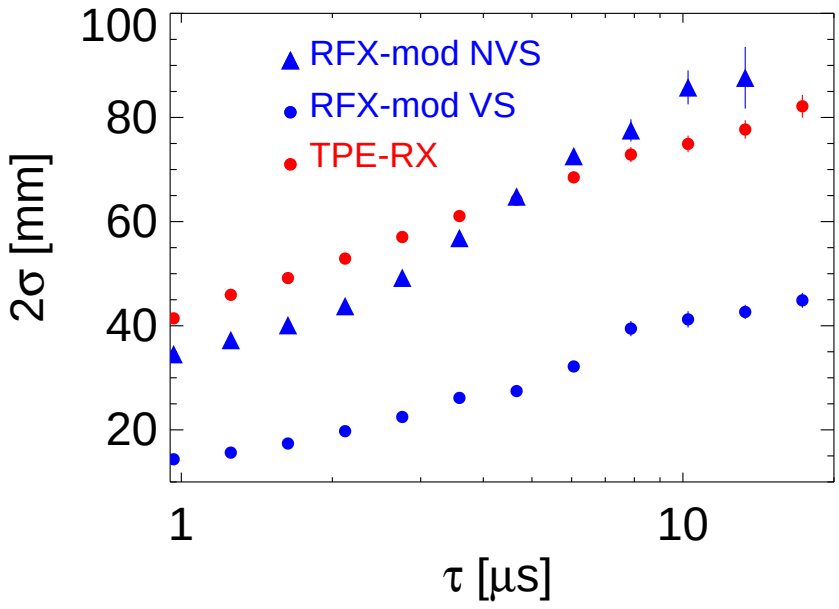

Figure 5.16: *Dependence of toroidal width of intermittent structures on wavelet time scale τ as computed by the conditional average technique. RFX-mod with virtual shell (blue circles), RFX-mod without virtual shell (blue triangles) and TPE-RX(red).*

behaviour of the flatness in the two experiments (figure 5.7): in fact, if $2\,\mu s$ is a "small" scale for both the RFP experiments, the "large" scales are different, as they are chosen as the scales at which the values of F are sufficiently different from the values at $2\,\mu s$. In the two figures 5.14 and 5.15, the Gaussian best fits of the form $Ae^{-(1/2)(x/\sigma)^2}$ have been superimposed to the average patterns of intermittent structures (red dashed lines). The value 2σ is considered as the toroidal width of the structure. Figure 5.16 shows that this width scales non-linearly with the wavelet characteristic time. In red there are the data for TPE-RFX and in blue for RFX-mod; also the error bars are reported. For RFX-mod two experimental conditions ere compared: the standard operational condition with the magnetic boundary control (virtual shell operation, VS) and without (NVS) [141]. The general trend is the same for the two experiments: bursts detected on small scales appear to be more spatially localised than at large scales. The great difference between the two experiments is the absolute value of $2\sigma(\tau)$. The edge structures in TPE-RX are about two times larger in the toroidal direction with respect to the ones of standard RFX-mod. However, without the control of the magnetic boundary (NVS), the behaviour is comparable to TPE-RX. Before trying to deduce an explanation of this difference, another result will be introduced. In figure 5.17 the linear density of edge structures N_s (i.e. the number of structures per unit of space) for RFX-mod (with and without virtual shell) and TPE-RX is shown as a function of the time scale of the fluctuation τ. Using the central fan of

the GPI the toroidal velocity of the edge fluctuations v_ϕ are evaluated using the cross-correlation technique described in paragraph 5.2. With the LIM method the intermittent events for each time scale N_τ are identified in all the 16 lines of sight of the central fan and the average number of events ΔN_τ in the analysed time interval Δt are computed. Then the linear density of bursts is evaluated as:

$$N_s = \frac{\Delta N_\tau}{v_\phi \Delta t} \tag{5.30}$$

for the two experiments. Since the number of structures that cross the GPI depends upon their velocity, we divided the number of events ΔN_τ by the toroidal velocity measured and for the time window analysed. Here it is assumed that the radial velocity of fluctuations is negligible respect to the toroidal one.

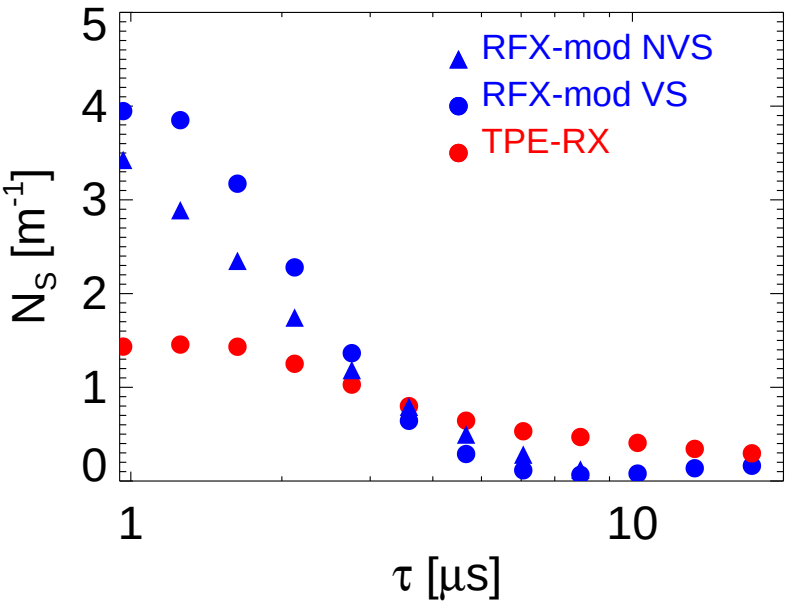

Figure 5.17: *Linear density of intermittent structures as a function of time scale in RFX-mod with virtual shell (blue circles), RFX-mod without virtual shell (blue triangles) and TPE-RX(red) detected in the GPI signal.*

The variation of N_s with respect to the time scale of the fluctuations τ is similar for the two experiments: there are more intermittent events for small τ and less for large ones. Moreover N_s at small scale ($\tau < 4\,\mu s$) is about three times larger in RFX-mod than in TPE-RX, so there are more intermittent structures per unit space.

Summarising the results described in the two figures 5.16 and 5.17, it is clear that both the toroidal width and the linear density of the edge structures have the same behaviour with the time scale τ of the fluctuations. However $2\sigma^{TPE} \approx 2 \cdot 2\sigma^{RFX}$ and $N_s^{TPE} \approx 1/3 \cdot N_s^{RFX}$ for small scales in the standard virtual shell operation. This difference in N_s is probably due to the difference in plasma density.

In fact TPE-RX has a metallic first wall and so it operates mainly at low density, about $n/n_G \approx 0.15$; instead the plasma discharges analysed in RFX-mod are characterised by $n/n_G \approx 0.35$. This means that in TPE-RX there are edge structures that are larger than in RFX-mod, but their linear density are smaller. This difference in the edge turbulence could be directly connected with the different magnetic boundary, in particular with the radial magnetic field B_r at the edge. With the MHD active control (VS) developed in RFX-mod the magnetic boundary is well controlled, and in particular the radial magnetic field at the edge is maintained at a very low level ($B_r(a) \approx 0$). This better control in the magnetic boundary could explain the difference between the two RFP experiments described here. An experimental evidence in this direction is that, operating in RFX-mod without the active control of the magnetic field, the edge turbulence has a behaviour very similar to TPE-RX, in particular concerning the toroidal width of the structures.

5.5.2 Potential structures and emissivity structures

In TPE-RX experiment, the measurements of edge turbulence with both the GPI and the Langmuir probes allow to compare the two diagnostics obtaining more information about the edge structures. In particular it is possible to draw some conclusions about the driving mechanism. The Langmuir probes measure the floating potential V_f, and the gas puff imaging measures a signal whose fluctuations are proportional to the local electron density fluctuations $\tilde{n}_e$. In fact, even if the light emission measured by the GPI depends both on the local electron density and temperature (see eq 3.2), in the plasma edge the relative temperature fluctuations are normally smaller than the density ones [142].

In order to study the relation between V_f and n_e, the conditional average analysis (technique described in sec. 5.5.1) is applied, comparing the intermittent structures detected in the GPI signal (n_e structures) and the potential structures detected with the electrostatic probes.

To this end, in the central chord of the central fan of the GPI the intermittent events are detected with the LIM technique, and the conditional average is made in the floating potential signal of the most inserted probe ($16\,mm$ inside the plasma). The results are reported in figure 5.18 for positive and negative intermittent events with a time scale $\tau = 22.5\,\mu s$. The GPI pattern is a monopole-like shape located at the center of a dipole pattern of potential: the two types of structures, density and potential, are well related, and they combine together to positively contribute to anomalous transport.

To underline the similarity of the edge turbulence in different machines, we remind that also in Alcator C-mod a similar relation has been described between the structures of the GPI and the one detected in the potential with Langmuir probes [139]. These results suggest a phase shift between the structures detected in n_e (the GPI signal) and in the potential V_f of about $\pi/2$ and the phase shift between these two quantities can give some information about the nature of the instabilities that affect the turbulence and about the source of free energy [143].

In figure 5.19 the cross-phase between ϕ and n_e is shown as a function of the frequency.

The coherence is higher than zero, indicating that the two quantities are linked,

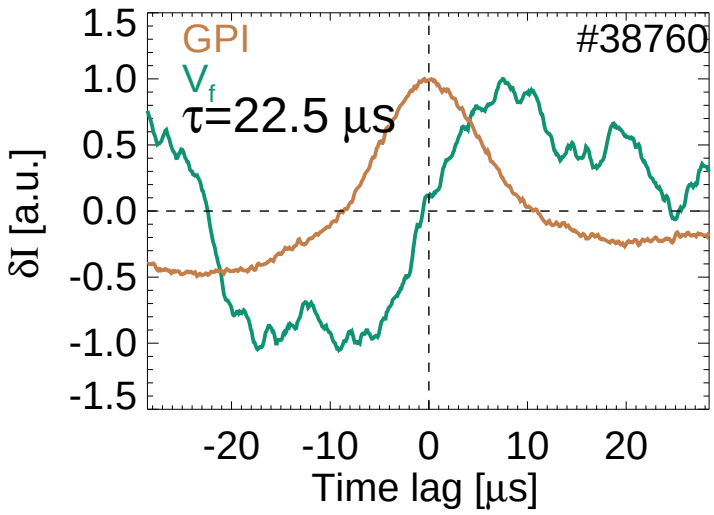

(a) Conditional average on GPI peaks

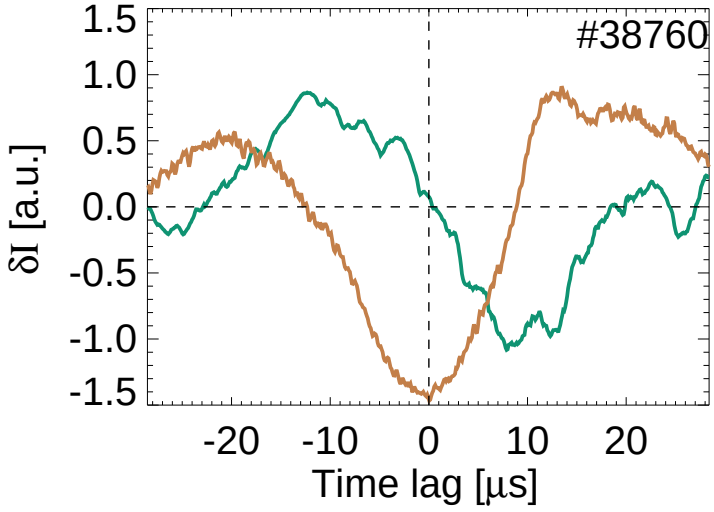

(b) Conditional average on GPI valleys

Figure 5.18: *Relation between the GPI structures (brown) and the floating potential ones (green) detected with the conditional average technique. (a): positive emissivity event (peak of n_e); (b): negative emissivity event (valley of n_e). Data from TPE-RX.*

and the cross-phase assumes a value of about $-\pi/2$, as suggested by the conditional average analysis. The phase assumes a constant value for the frequency range

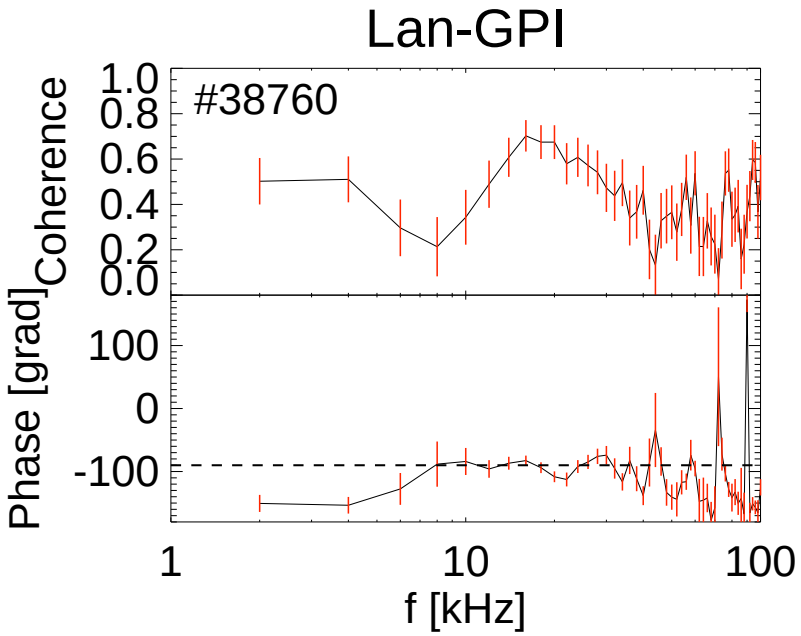

Figure 5.19: *Coherence and cross-phase between potential and GPI signals as a function of the frequency. The horizontal dashed line corresponds to the cross-phase of $-\pi/2$. Data from TPE-RX.*

$(10 \div 50\,kHz)$, where the coherence is high. Even if it could be interesting to analyse also frequency higher than 100 kHz as in this experiment the intermittency behaviour of the turbulence is detected up to 300 kHz (see fig. 5.7), the collected data do not allow it.

Similar relation between density and potential structures of the plasma edge detected with the conditional average technique has been described also for the W7-AS [136] and TJ-K [144] stellerators. Also the linear machine VINETA presents similar behaviour when the developed turbulence dominates the plasma [145].

All these data contribute to consider that the edge turbulence in TPE-RX, for the considered frequency range, is caused predominantly by curvature driven modes, as they are in good agreement with the simulation described in ref. [143], and as suggested for Alcator C-mod [139]. Also a comparison of experimental results in TCV tokamak with two dimensional interchange turbulence simulations are in excellent agreement, indicating that the SOL turbulence in that tokamak is largely governed by non-linear interchange motions [146], and that this instability is a common feature of the plasma edge.

These instabilities (as the drift waves) are driven by the background plasma pressure gradient, which can be considered the source of free energy needed to the instabilities to develop [147]. We will see in the next paragraph 5.6 that also the edge turbulence of NSTX tokamak is related with the electron pressure gradient [120].

The basic mechanism of curvature driven modes is schematically illustrated in figure 5.20. As the study of this instability are beyond the scope of this thesis, only a brief and simple description is given, to better clarify it. The initial state

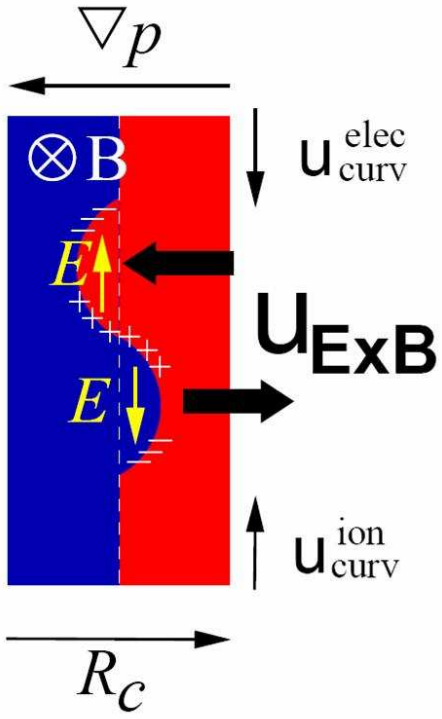

Figure 5.20: *Instability mechanism of curvature driven modes. R_C is the curvature radius, outward; ∇P is the radial gradient of the pressure, inward; B is the magnetic field, mainly in the poloidal direction in the edge of RFPs; the two u_{curv} are the curvature drift velocities for electron and ion (in opposite directions) of equation 5.31.*

is a plasma pressure gradient ∇p with superimposed sinusoidal perturbation. The curvature and ∇B drifts lead to a separation of charge due to the opposite ion and electron velocities:

$$u^q = \frac{2W_{||} + W_{\perp}}{q} \frac{\mathbf{B} \times \nabla B}{B^3} \tag{5.31}$$

where $W_{||}$ and $W_{\perp}$ are the parallel and perpendicular kinetic energy. As a consequence, an electric field $\mathbf{E}$ perpendicular to the magnetic field $\mathbf{B}$ is generated. The resulting $\mathbf{E} \times \mathbf{B}$ drift amplifies the initial perturbation and becomes linearly unstable if the magnetic field gradient is parallel to the plasma pressure gradient. This mechanism leads to a phase shift between the plasma pressure fluctuations and the plasma potential fluctuations of $\approx \pi/2$.

Even if the results described here cannot demonstrate unambiguously this mechanism as the drive of the edge turbulence, they give some suggestions in this direction, and in particular that the pressure gradient could play a significant role.

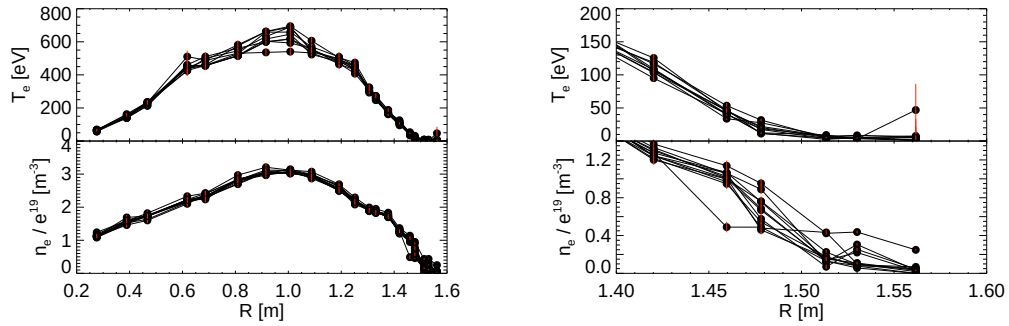

(a) (b)

Figure 5.21: *Radial profiles of electron temperature T_e and electron density n_e measured with the Thomson scattering diagnostic in NSTX. Each line is referred to one analysed shot in the time interval when the deuterium of the GPI was puffed. Here the L-mode phases are shown. (a): complete profiles. (b): detail of the edge profiles.*

5.6 Radial dependence of turbulence in NSTX

In NSTX tokamak experiment it is possible to study the radial behaviour of the edge turbulence with the radial array of the GPI, and in particular to study the relation with the radial profiles of electron temperature, density and pressure measured with the Thomson scattering diagnostic [148]. For the analysis described in this thesis, 13 similar discharges taken in one single day are studied.

In figure 5.21 the radial profiles of T_e and n_e for the 13 NSTX analysed shots are shown. Every profile refers to the time interval used also for the analysis of the GPI data. The analysed discharges have an electron temperature at the center of about $800\,eV$, electron density $3 \cdot 10^{19}\,m^{-3}$ and a normalised density $n/n_G \approx 0.4$. The radial profiles of the various discharges are very similar to each other, also in the edge, and so it is possible to make a statistical analysis of the relation between the profiles and the edge turbulence. We recall that the GPI views the region from about $R = 1.4\,m$ and $R = 1.55\,m$ and that in the discharges analysed here the separatrix is in the region $1.455 \div 1.465\,m$ and it doesn't change more than $10 - 20\,mm$ in the time window used for the analysis.

In order to study the radial dependence of the edge turbulence, the radial array of the GPI chords (R1, R2, P4, R6, R7 in fig. 3.9) is used. The different behaviour of signals in the radial array is clearly visible also in the raw data of figure 5.22. In this figure the innermost R1 (a) and the outermost R7 (b) chords are shown. Each signal is normalised to its average value over the 10 ms-long analysis window. Inside the separatrix the GPI fluctuations have a smaller amplitude and many bursts are observed in the whole time window displayed; indeed outside there are only few bursts but very intense.

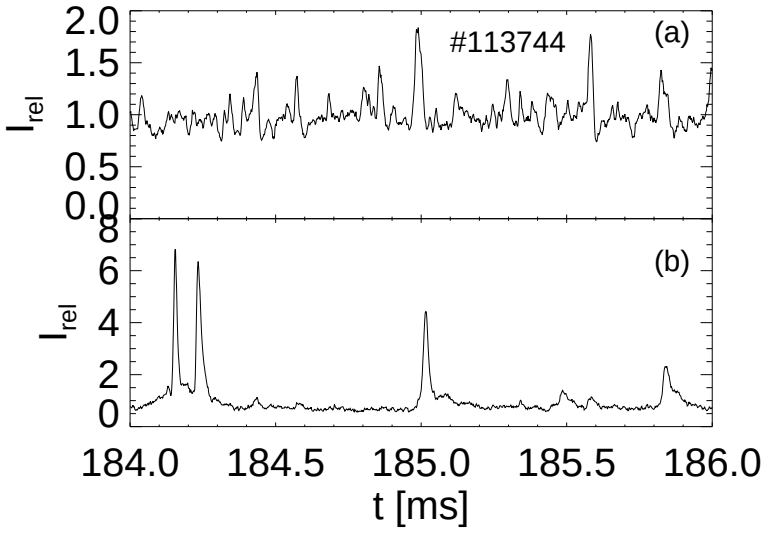

Figure 5.22: *Time behaviour of two PMT signals of NSTX. Chord R1 (a) is 60 mm inside the separatrix and chord R7 (b) is 80 mm outside the separatrix. The two signals are normalised to their average value within the time window analysed.*

To clarify and quantify this different behaviour, the statistical properties are studied, in particular the PDFs of the signals are evaluated. The PDF is computed by dividing the analysed signal in 40 amplitude bins and counting the samples of the signals in each bin. Then the PDFs are normalised to their maxims to make the comparison easier. A typical example of this result is reported in figure 5.23.

Both signals have non-Gaussian distribution, with high positive tails. This non-Gaussian statistics of the signal of the edge plasma turbulence is a common feature detected in all magnetic configurations [123, 28, 149, 150, 117, 71, 119, 118, 134, 132, 121, 122]. Moreover the departure from the normal distribution is clearer for the chords that measure outside the separatrix (e.g. R7), which exhibit a higher tail. The results verify that the edge intermittency level is higher outside the separatrix.

To quantify this difference, the third (S, Skewness) and the fourth (F, Flatness) order moments are computed for different discharges and different chords of the radial array. The Flatness was already defined in equation 5.24; the skewness of the GPI signal I is defined as:

$$S = \frac{\langle (I - \langle I \rangle)^3 \rangle}{\langle (I - \langle I \rangle)^2 \rangle^{3/2}} \tag{5.32}$$

Here we recall that the Flatness measures the weight of the tail in the distribution, and the skewness measures the degree of asymmetry. The result is shown in fig. 5.24 (for the Normal distribution $F = 3$ and $S = 0$.)

The Flatness and Skewness exhibit two different regions: for the three most internal chords F assumes about the same values (~ 5) and increases up to 100

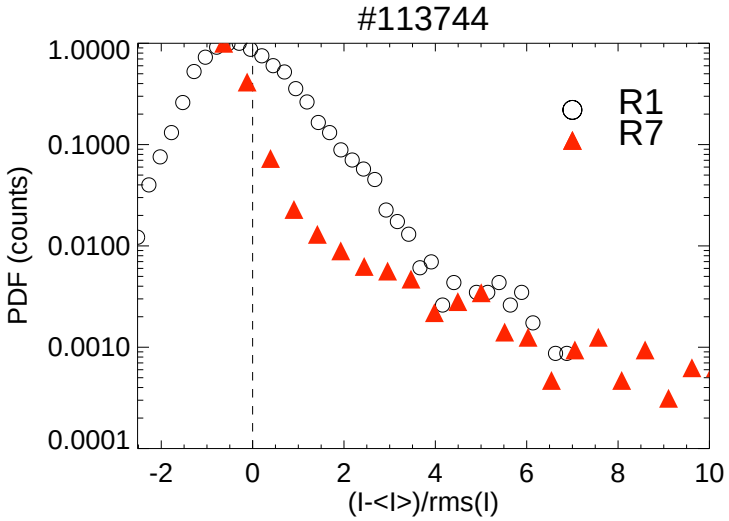

Figure 5.23: *Normalised PDF of the normalised signal amplitude for two radial GPI chords: R1, about 60 mm inside the separatrix (circles) and R7, about 80 mm outside (red triangles). Data from NSTX.*

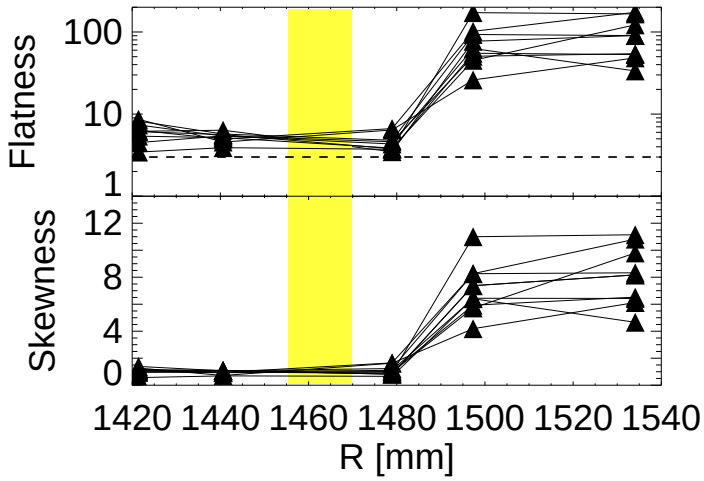

Figure 5.24: *Flatness and skewness as a function of the major radius of NSTX. Each line is from different shot. The separatrix is between 1455 and 1465 mm (shadowed region).*

in the outermost channels. Also the Skewness has a similar behaviour, with the most external chords that are more asymmetric. The PDF of the fluctuations is non-Gaussian for all radii, but the departure from the Normal distribution is more pronounced for the most external chords. These results are in agreement with other measurements of the edge fluctuations made using Langmuir probes in tokamak experiments [151, 152, 146]. As we move outward the GPI signal is more and more dominated by positive ($S > 0$) bursts with high amplitude (high F values) relative to the mean.

To clarify the meaning of these phenomenologies and to study the relation with the electron pressure profile, the packing fraction of the edge structures is evaluated as a function of the radius. It is defined as [98]:

$$f_p = \sum_{\tau} \tau N_\tau / \Delta t \tag{5.33}$$

where Δt is the time interval analysed and N_τ is the number of intermittent events at scale τ detected in the signal with the LIM; the parameter f_p is evaluated for the various radial chords. This estimator measures the percentage of the signal occupied by the structures. In order to avoid double counting, all the smaller structures

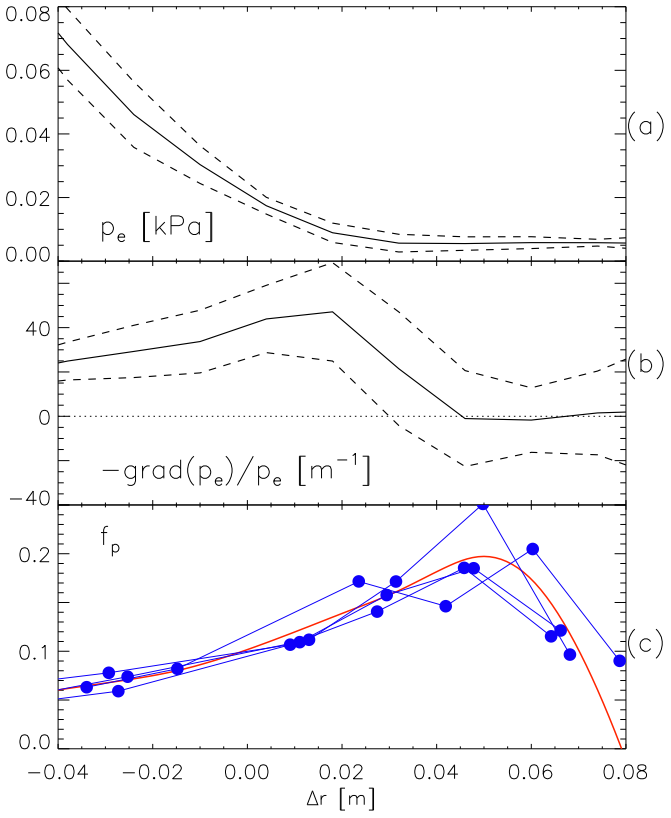

Figure 5.25: *Packing fraction f_p as a function of the radius (c) compared with the average electron pressure profile (a) and its logarithmic radial derivative (b) for NSTX. The dashed lines are the errors in the radial profiles. Zero in the x-axis is the position of the separatrix; positive values of the radius mean outward. In panel (c) the circles are the experimental packing fraction points; the continuous line is a spline fit.*

whose time occurrence lies within the width of the larger ones are discarded. In fig. 5.25 the packing fraction f_p is computed for the different radial chords of the GPI, and compared with the radial logarithmic derivative of the pressure gradient ($\nabla p_e/p_e$) measured with the Thomson scattering diagnostic.

For every shot the electron pressure is measured and the experimental points are interpolated using a spline. Then the average pressure and its radial gradient are evaluated. Inside the separatrix f_p is about 5 % and increases up to 20 % outside. The maximum of the packing fraction corresponds to the minimum of the logarithmic gradient of the electronic pressure. In ref. [153] the birth of blobs measured with the GPI in NSTX is seen at the location of the maximum of this logarithmic derivative, which is near the separatrix. The analysis regarding the packing fraction developed here suggests that these structures, born near the separatrix, evolve toward the low gradient region outside the separatrix, occupying a bigger area of plasma (f_p increases). At the same time, the normalized amplitude of these blobs increases, since the PDF of the signal develops larger tails as reported in figure 5.24.

Therefore a clear link is found between the edge structures and the electron pressure. This relationship, together with the measurements of floating potential fluctuations in TPE-RX, suggest the electron pressure as a possible drive for the edge turbulence.

6

Edge turbulence and magnetic fluctuations

6.1 Dynamo relaxation events in RFX-mod

Relaxations events in magnetised plasmas are signs of self-organisation processes, well known to occur in almost all current-carrying fusion plasmas (they play a key role in sawteeth activity in tokamak discharges [154]) as well in many astrophysical phenomena such as the evolution of solar flares and the formation and accretion of stars and galaxies. In RFP devices, a spontaneous and almost cyclic rearrangement of the magnetic topology occurs, which is considered to be due to reconnection of magnetic field lines [12]. This process can take place either continuously or in a discrete fashion: the latter is called *Dynamo Relaxation Event* (DRE).

The discharges of RFX-mod with reversal parameter $F < -0.1$ are characterised by discrete MHD activity, visible in the strong oscillations of the F parameter[1].

These DREs are clearly visible in fig 6.1, where the time behaviour of the reversal parameter (which strong oscillations are the magnetic relaxation events) with the plasma current and the GPI signal are shown. The plasma discharge shown is a typical shot of RFX-mod analysed in this chapter. Plasma current assumes values of about $600\,kA$, and the reversal parameter $F < -0.1$ in order to have frequent and deep DREs. In fact, for $F > -0.1$ DREs appear only rarely.

The study of the DREs is a topic of general interest because it allows to investigate how the MHD activity influences phenomena like the plasma-wall interaction. Moreover it is interesting to study how this oscillations in magnetic field can modify the edge turbulence. Some suggestions of the interaction between the MHD activity and the edge turbulence have already been reported in [129]: in this reference

[1] The reversal parameter F, defined in chapter 1, equation 1.23, is the ratio between the toroidal magnetic field at the edge and the average toroidal field.

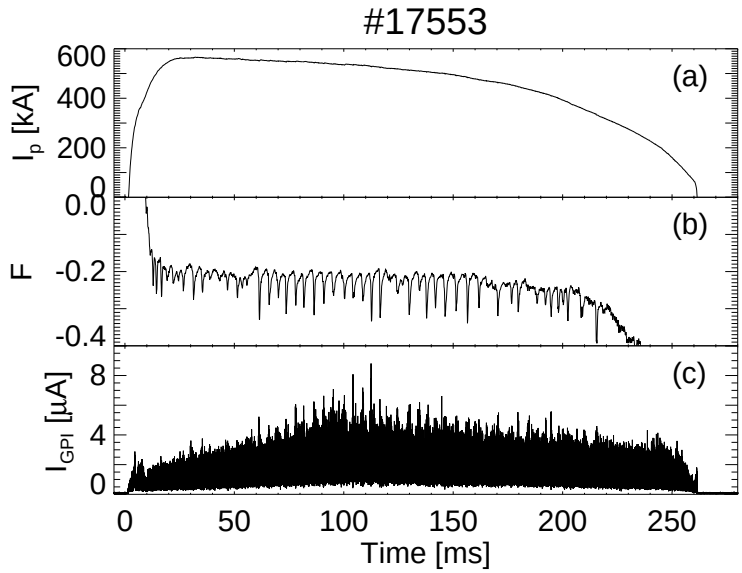

Figure 6.1: *Example of one discharge of RFX-mod with DREs. (a): plasma current; (b) reversal parameter with frequent DREs; (c) signal of one GPI chord. The DREs are the strong oscillations of the reversal parameter.*

it was demonstrated the link between the MHD activity and the floating potential fluctuations measured in the edge of RFX for low current plasma discharges $(200 - 300\,kA)$. Now, with the GPI and new magnetic diagnostics installed in RFX-mod experiment, a more complete analysis of the interaction between the

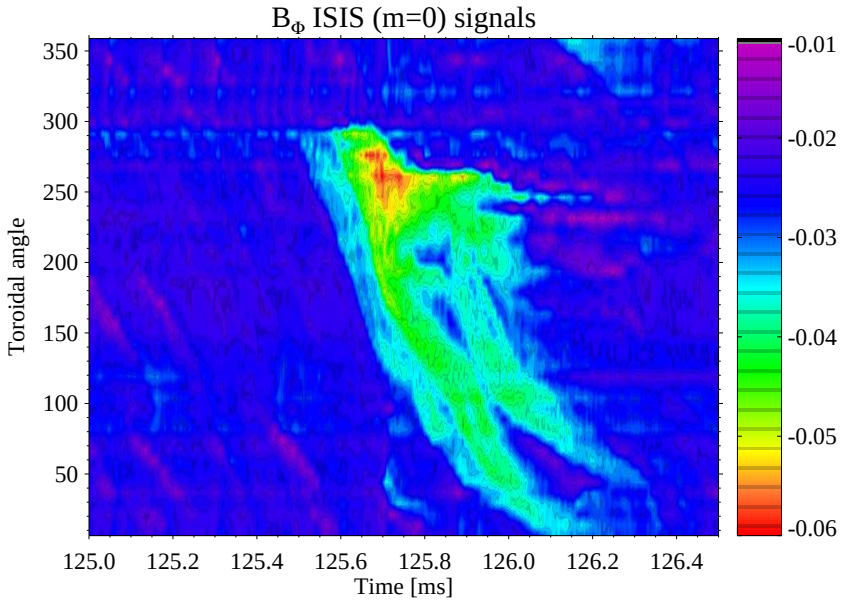

Figure 6.2: *Contour plot of $m = 0$ components of magnetic signals collected by ISIS during one DRE. RFX-mod, shot number* #20293*.*

MHD activity and the edge turbulence is possible. Then new information about the nature of the DRE is available.

In particular, RFX-mod is now equipped with a large set of magnetic pick-up coils located inside the vacuum vessel, which constitute the *Integrated System of Internal Sensors* (ISIS) [155]. These coils measure the time derivative of the toroidal component of the the magnetic field. They are installed behind the graphite tiles which cover the vacuum vessel of the machine, and they are evenly distributed in the toroidal direction, on two arrays located in two opposite poloidal positions. Each array consists of 48 coils. The sampling frequency is $2\,MHz$, while the estimated bandwidth of the measurements is up to $300-400\,kHz$. This high frequency and their location inside the vacuum vessel allow to capture the magnetic structure of the DRE.

The spatial and temporal structure of one typical DRE measured with ISIS is reported in figure 6.2. The magnetic structure is born at $t \approx 125.6\,ms$ and in the toroidal position $\phi \approx 270°$, that is also the angular position of the locked mode. Therefore the DRE is characterised by a high amplitude $m = 0$ magnetic perturbation that initially occurs at the toroidal position of the locked mode and then moves mainly opposite toroidal plasma current direction (toward decreasing toroidal angle ϕ in fig. 6.2). During this propagation the amplitude of the $m = 0$ perturbation slowly decreases until it vanishes. Deeper analysis has shown that this $m = 0$ rotating perturbation is associated to a moving poloidal current [156].

Moreover, it is interesting to study not only the effect of this large poloidal current filament in the global plasma parameter, but also the interaction between the DRE and the edge turbulence, trying to complete the previous analysis and understanding in a better way the nature of the edge turbulent structures.

6.2 DRE and edge turbulence

A tight correlation between the MHD activity (that is mainly a magnetic activity of the plasma core) and the edge turbulence is not obvious. In RFX-mod, the first simple link between the two phenomena which involve different time and space scales are reported clearly in figure 6.3. The periodic oscillations in F are the magnetic reconnections; the two spectrograms (GPI and ISIS) feature an activity increase both in edge turbulence measured by the GPI and in magnetic fluctuations of toroidal field measured by ISIS. In fact, during the DRE there is an increase of edge fluctuations for frequencies of about $50\,kHz$ that decreases between two crashes in the GPI signal. A similar behaviour is detected also in the edge magnetic fluctuations measured by ISIS. This means that the core MHD dynamics (mirrored by the crashes in F) is well correlated with the edge structures, but also with the fast (with respect to the low frequency dynamic of the DRE) fluctuations of the magnetic field. This is a first indication that the edge turbulence interacts in someway with the DRE and that there is a magnetic activity that involves frequencies higher that the MHD ones and very similar to the frequency of the turbulence detected by the GPI; moreover the magnetic activity is well correlated with the fluctuations of the GPI signals. These observations induce to investigate the interaction between DREs and edge fluctuations, but also to study

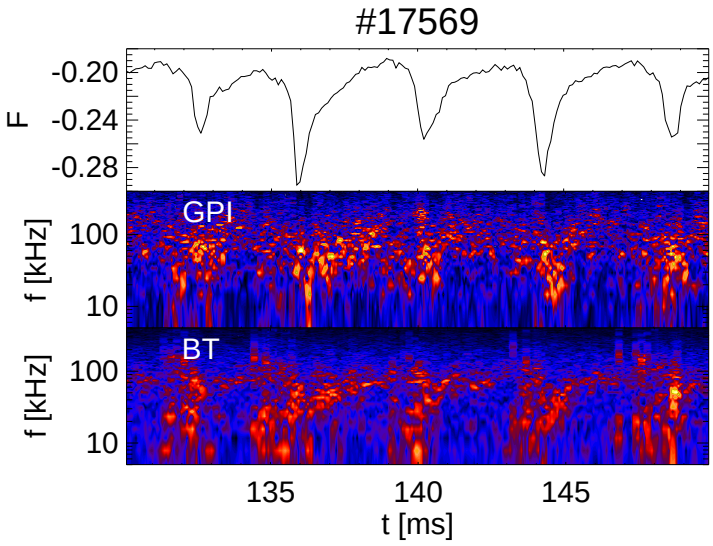

Figure 6.3: *Comparison between the spectrogram of GPI signal and of toroidal magnetic field measured with ISIS in RFX-mod. The reversal parameter F is also shown in the first panel, where many DREs are visible.*

how the edge structures are linked with the high-frequency magnetic structures. A strong indication of the interaction between DREs and edge fluctuations is shown in fig. 6.4.

Panel (a) shows the fluctuations of the local magnetic field δB_ϕ measured by ISIS. The magnetic fluctuations are measured in the same toroidal position as the GPI in order to have a local estimation of the magnetic field fluctuations; in fact, as shown in fig 6.2 the magnetic field is not uniform along the toroidal direction. δB_ϕ is computed by numerically integrating the raw signals of the pick-up coils; only the fluctuating part is used.

In panels (b) and (c) the total energy of the Fourier modes of the tomographic reconstruction and the toroidal velocity of the $p = 1$ mode (evaluated according to equations 4.15 and 4.19) of the GPI fluctuations are shown. Also the average toroidal length of the edge emissivity measured by the GPI λ_ϕ (panel (d))is well correlated with the magnetic fluctuations. λ_ϕ is evaluated with a cross correlation technique: as the central fan of the GPI has 16 LoS equispaced along the toroidal direction, it is possible to evaluate the cross correlation function for every pair of lines separated by a distance Δ as:

$$C(\Delta) = \int I(t,x)\, I(t,x+\Delta)\, dt \tag{6.1}$$

where $I(t,x)$ is the signal of the line of sight of the GPI that looks at the toroidal position x. To evaluate the integral of equation 6.1, a time portion of $0.5\,ms$ of the GPI signal is used. The cross correlation $C(\Delta)$ has a relation with the distance between the lines of sight like:

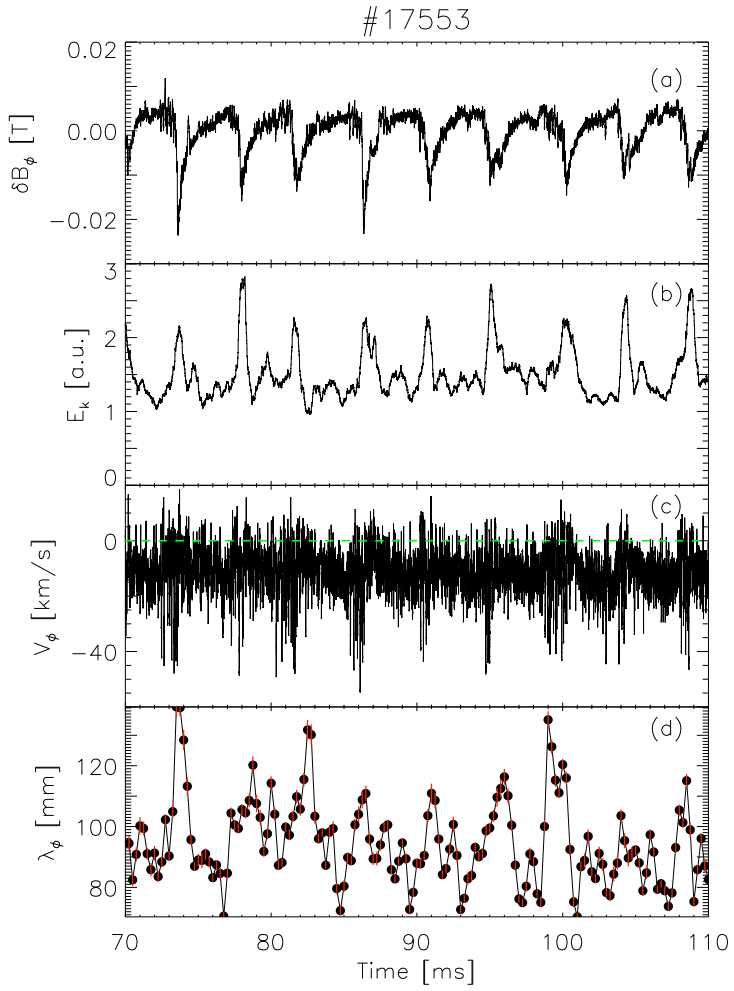

Figure 6.4: *(a): fluctuations of the toroidal magnetic field; (b) total mode energy of the tomographic reconstruction; (c) toroidal velocity of the edge fluctuations; (d) toroidal correlation length λ_ϕ. Data from RFX-mod.*

$$C(\Delta) \sim e^{-\frac{\Delta}{\lambda_\phi}} \tag{6.2}$$

Therefore, it is possible to compute a fit of the experimental data $C(\Delta)$ and measure the toroidal correlation length and its statistical error as reported in fig 6.4 (d). As the correlation is calculated using $0.5\,ms$ of the GPI data, the time resolution of λ_ϕ is $0.5\,ms$.

Coming back to the physical results of figure 6.4, the time signal of the energy of the 2D tomographic reconstruction E_k (b) is well correlated with the DRE (a): every time a strong fluctuation of toroidal magnetic field occurs, the energy increases. As the signal E_k measures the energy of the edge turbulence detected

by the GPI, this correlations means that the turbulence level increases every time the poloidal current filament of the DRE is in front of the GPI. This is another indication that the MHD activity can modify the properties of the edge turbulence.

The DRE modifies also the toroidal velocity of the fluctuations (6.4 (c)). The mean toroidal velocity evaluated from the 2D tomographic reconstruction is about $-15\,km/s$ along the $\mathbf{E} \times \mathbf{B}$ flow, in agreement with velocity measured with the cross correlation technique described in section 5.2. When the DRE passes in the field of view of the GPI, the toroidal velocity of the edge turbulence begins to fluctuate, reaching values up to $-40\,km/s$. This means that the passage of the current filament of the DRE modifies the toroidal velocity of the edge fluctuations. Probably the magnetic perturbation changes the ion losses toward the wall, and this causes a modification in the profile of the radial electric field; the consequent variation of the $\mathbf{E} \times \mathbf{B}$ velocity might change the velocity of the edge structures. At the same time, the toroidal correlation length of the fluctuations increases in correspondence of the magnetic perturbation: the edge fluctuations are larger along the toroidal direction. This figure explains that the DRE has a great influence on the edge turbulence: the fluctuations become toroidally larger and their velocity fluctuates.

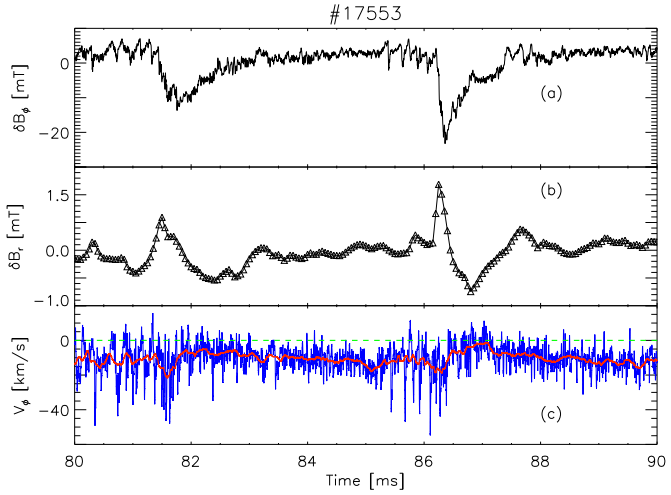

Figure 6.5: *(a): fluctuations of toroidal magnetic field; (b): fluctuations of radial magnetic field; (c): toroidal velocity of the edge fluctuations (blue) and its smoothing (red). Data from RFX-mod.*

A deeper look in the structure of the DRE and edge turbulence is obtained in fig. 6.5. The first thing that has to be seen in the figure is the relation between the fluctuation of the local toroidal magnetic field (a) and the local radial magnetic field (b). The fluctuations δB_r are not measured with ISIS, but with the external coils, and so the time resolution is lower.

The fluctuations δB_ϕ are associated also with the radial magnetic field δB_r, and the relation between the two components confirms that the DRE can be interpreted as a poloidal current sheet that propagates mainly along the toroidal

direction. Then the zoom of the toroidal velocity (panel (c)) makes clearer the time behaviour of this signal. Between the two crashes $v_\phi \approx -15\,km/s$ with small fluctuations; when the DRE arrives, fluctuations increase, and v_ϕ assumes values from $-40\,km/s$ to $+10\,km/s$; then after the crossing, v_ϕ comes back to the standard value of $-15\,km/s$. The second DRE in the figure, that has a toroidal magnetic fluctuations of about $20\,mT$, modifies considerably the velocity increasing its fluctuation range. Instead the first one, that is smaller ($\approx 10\,mT$), is less visible in the radial component of the magnetic field, and it modifies only slightly v_ϕ. This means that only the strongest DRE affects the edge turbulence: if a DRE is born far from the GPI, and propagates along the toroidal direction, it arrives in front of the GPI already degraded and it cannot modify the edge turbulence. Making a statistics with many different discharges, shows that if a crash is characterised by $\delta B_\phi \approx 20\,mT$ it can modify the edge properties; instead, crashes with $\delta B_\phi < 10\,mT$ do not affect the turbulence.

Now the effect of the DRE directly on the edge structures is analysed. To detect the edge structures in the GPI signal, we used the triple product signal of three chords, relative to a central position of the field of view of the GPI. As already said, this signal is significantly different from zero only when a structure flows through the intersection point of the three LoS. So, whenever a threshold is exceeded, the fluctuation pattern in this triple product is considered a structure. A threshold of $3\,\sigma$ of the signal is chosen, but changing the threshold does not change the results obtained. After detecting the structures, their number is counted every $0.2\,ms$, obtaining in this way the signal of the time evolution of the number of intermittent events ($N(t)$) displayed in figure 6.6.

When the DRE is in front of the GPI, the number of intermittent events increases with respect to the standard conditions. To detect more clearly this behaviour, the conditional average technique (see section 5.5.1)has been applied to

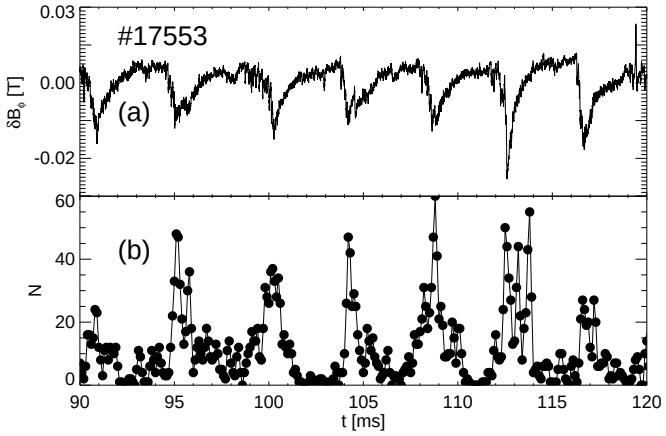

Figure 6.6: *Relation between DREs and the number of intermittent events in RFX-mod. (a): magnetic fluctuations of the local magnetic field; (b): number of edge structures.*

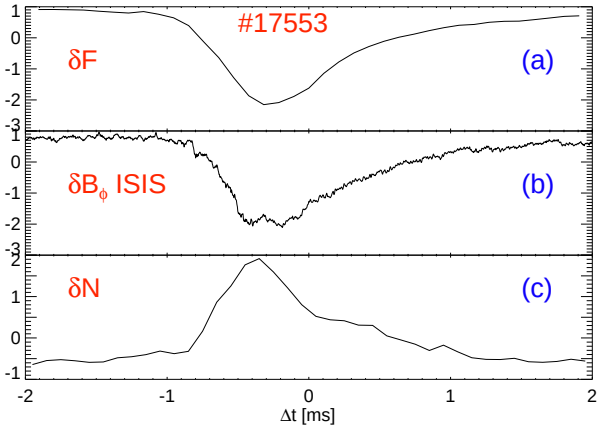

Figure 6.7: *Conditional average on DREs of RFX-mod. (a): average reversal parameter; (b): average magnetic fluctuations of the local toroidal field; (c): average number of intermittent events.*

the three signals $F(t), \delta B_\phi(t)$ and $N(t)$; the prescribed condition is the presence of a DRE in F signal. This signal was used instead of $\delta B_\phi(t)$ because it is smoother and so makes it simpler to detect the DREs.

Every time a DRE is detected in the reversal parameter signal, a time portion of $4\,ms$ centred around the time occurrence of the DRE is extracted in $F(t), \delta B_\phi(t)$ and $N(t)$; then for every signal the average is subtracted and then it is normalised to its rms. Eventually, the conditional averaged signals of figure 6.7 are obtained. When the DRE is detected in the global parameter F, it is also present in the local magnetic fluctuation signal $\delta B_\phi(t)$; correspondingly the average number of edge structure increases.

The magnetic activity at low frequency (the DRE) affects not only the toroidal velocity of the edge fluctuations, but it interacts directly with the intermittent events. Summarising the results obtained up to now, the DRE increases the number of edge structures together with the toroidal width of fluctuations and modifies their toroidal velocity. In fact, as in evaluating v_ϕ both from the cross-correlation analysis and from the tomographic inversion also the signals of the structures are used, the resulting velocity includes also the velocity of the intermittent events.

All these results induce to study also the magnetic structure of intermittent events, trying to understand the possible causes of the correlation between them and the DRE.

The simplest thing that can be done is to study the correlation between the local magnetic fluctuations measured with the magnetic coils installed on the GPI and the emissivity measured by the GPI. In figure 6.8, the cross-correlation between signals of the time derivative of the radial magnetic field $\frac{\partial B_r}{\partial t}$ measured with the magnetic coil of the GPI and the central chord of the central fan of the GPI is shown as a function of time. The signal of the GPI is high pass filtered at $100\,kHz$, to exclude the low frequency fluctuations.

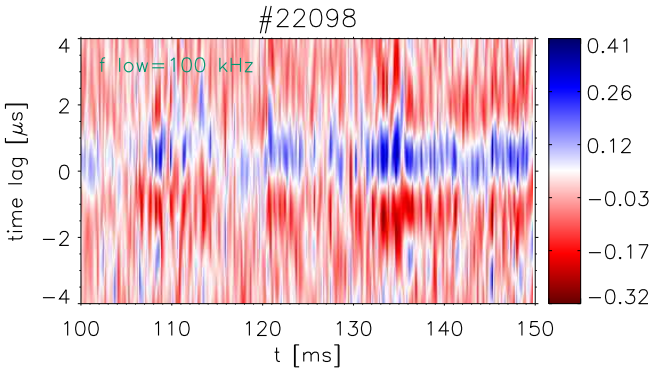

Figure 6.8: *Time behaviour of the correlation between the time derivative of the radial magnetic field and the central chord of the GPI. Data from RFX-mod.*

The cross-correlation is evaluated every 0.2 *ms* with a time portion of the signals of the same duration. The correlation varies with time, but it is clearly high, and in some intervals it assumes values up to 0.4. This means that the two types of fluctuations are linked together: the edge turbulence and the edge magnetic fluctuations are not separated, but there is some degree of connection between them. The edge turbulence should also have a magnetic structure. The maximum of the cross correlation is about zero time-lag: in fact the GPI chord and the magnetic pick-up coil are in the same toroidal position.

6.3 Edge structures as current filaments

A possible mechanism of interaction between the edge structures and the magnetic fluctuations can be identified if each structure is associated to a current filament. This way, the interaction with a DRE could be explained through a $\mathbf{J}\times\mathbf{B}$ force [157], and also the link between the GPI fluctuations and the high-frequency magnetic fluctuations detected with the magnetic probes of the GPI are explained.
Some indication in this direction was already proposed in [158]. Now, with the triaxial magnetic coils installed in the GPI system it is possible to study how the GPI fluctuations are related with the magnetic ones, and what is the phase relation between the signals. Thus the magnetic structures of the edge turbulence can be investigated.

It is supposed that the edge structures detected by the GPI are related to a current filament along the poloidal direction. In the next sections we will write a model of a current filament moving radially and toroidally and then compare these results with the experimental ones, giving some considerations.

6.3.1 Simple model

A simple model of a poloidal current filament moving along the toroidal and radial direction is described here. It is meant to be a description of what is detected with the GPI and the magnetic probes. The geometry used is shown in fig. 6.9. The

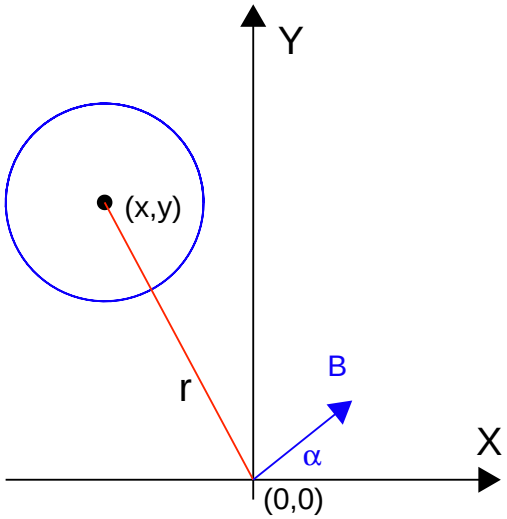

Figure 6.9: *Cartoon of the geometry used for the model of the current filament propagating along radial (y) and toroidal (x) direction.*

(X, Y) plane is the $(toroidal, radial)$ plane; the GPI with the magnetic probes is in $(0, 0)$. The blue circle is the current filament.

The current filament centered in (x, y) with a poloidal current (I) produces a magnetic field in $(0, 0)$ with amplitude:

$$B = \frac{\mu_0 I}{2\pi r} \tag{6.3}$$

where r is the distance of the center of the current filament from the magnetic pick-up coils that are in $(0, 0)$. In the figure the angle α is defined as the angle between the magnetic field and the X axis. In this geometry we have:

$$\begin{aligned} x &= r \sin\alpha \\ y &= r \cos\alpha \end{aligned} \tag{6.4}$$

and

$$\begin{aligned} B_x &= \frac{\mu_0 I}{2\pi r} \cos\alpha \\ B_y &= \frac{\mu_0 I}{2\pi r} \sin\alpha \end{aligned} \tag{6.5}$$

Assuming that the current filament moves in a linear uniform motion with two velocities v_x and v_y we have:

$$\begin{aligned} x(t) &= v_x\, t \\ y(t) &= y_0 + v_y\, t \end{aligned} \tag{6.6}$$

Then, replacing in eq. 6.5 $x(t)$ and $y(t)$, remembering that $r^2 = x^2 + y^2 = v_x^2 t^2 + (v_y t + y_0)^2$ and deriving with respect to time we obtain (the constant value $\frac{\mu_0 I}{2\pi}$ has been dropped):

$$\begin{aligned} \frac{\partial B_x}{\partial t} &= \frac{v_y}{r^2} - \frac{v_y t + y_0}{r^4}\left[2v_x^2 t + 2v_y(v_y t + y_0)\right] \\ \frac{\partial B_y}{\partial t} &= \frac{v_x}{r^2} - \frac{v_x t}{r^4}\left[2v_x^2 t + 2v_y(v_y t + y_0)\right] \end{aligned} \tag{6.7}$$

In this way the simulated signals $\frac{\partial B_x}{\partial t}$ and $\frac{\partial B_y}{\partial t}$ are proportional to the signals collected by the pick-up coils.

The results of this simulation are reported in figure 6.10. This simulation shows the pattern that can expect if the edge structures are associated with a current filament moving both toroidally and radially. If $v_y = 0$, the measured patterns of $\frac{\partial B_x}{\partial t}$ and $\frac{\partial B_y}{\partial t}$ are shown in figure 6.10 on the left. This reference signal is symmetric, and the minimum of $\frac{\partial B_y}{\partial t}$ corresponds to the change of sign of $\frac{\partial B_x}{\partial t}$. The symmetry is mirrored also in the hodogram. If $v_y \neq 0$, the resulting signals are shifted and become asymmetric, as reported in figure 6.10 on the right, for $v_y/v_x = 0.6$. In this simple model the current filament is supposed to have a pure poloidal component

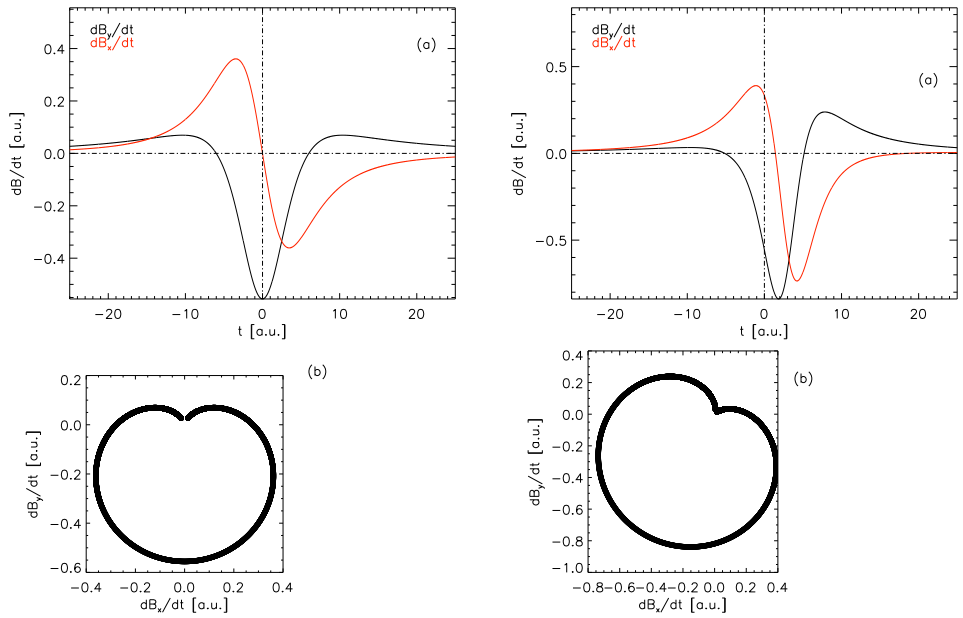

Figure 6.10: *Left: expected signal from a current filament moving along the toroidal (x) direction and with radial velocity $v_y = 0$ measured by pick-up coils in $(0, 0)$ (a); $\frac{\partial B_x}{\partial t}$ as a function of $\frac{\partial B_y}{\partial t}$ for the simulated signal (b). Right: the same results for a current filament with $v_y \neq 0$.*

of current; however, it seems reasonable that the filament is aligned along the magnetic field at the plasma edge. In the discharges here analysed, the angle between the poloidal direction and the direction of the magnetic field at the edge assumes values from 3 up to 10 degrees. This angle is small, and it only can vary the relative amplitude of the $\frac{\partial B_x}{\partial t}$ and $\frac{\partial B_y}{\partial t}$, but not their relative phase. So the effect is negligible.

After seeing the expected magnetic signals produced by a current filament moving along the radial and toroidal direction, we will compare the experimental ones with them.

6.3.2 Experimental data

In order to study the relation between edge turbulence and magnetic structures, the conditional average technique has been applied (see paragraph 5.5.1). The intermittent structures have been detected in the central fan of the GPI, with the method based on the triple product signal used also to obtain figure 6.6. Then the conditional average has been applied to the signals of the time derivative of the radial and toroidal magnetic field to obtain the average magnetic structure related to the structure of the GPI.

Figure 6.11 (a) shows the magnetic structure related with the emissivity one; the hodogram is in (b). Since from every signals the average has been subtracted

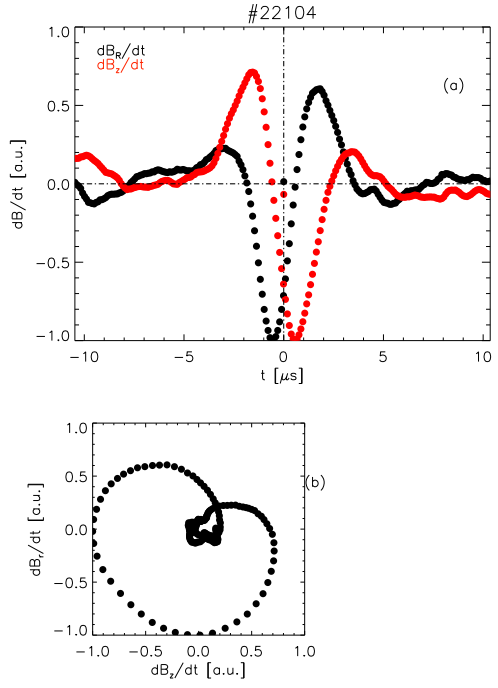

Figure 6.11: *Experimental conditional average on the time derivative of radial and toroidal magnetic field from RFX-mod (a); its hodogram is shown in panel (b).*

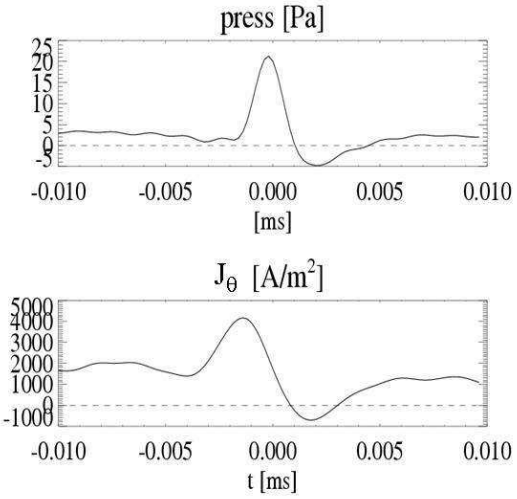

Figure 6.12: *Conditional average of the electron pressure and poloidal current density measured with the insertable edge probe in RFX-mod.*

and then normalised to the rms, all the quantities are in arbitrary units: we are interested only in the shape of the magnetic fields and in their reciprocal relation. On comparing the two figures 6.10 and 6.11, the magnetic structures and the hodograms are very similar: the experimental magnetic fields related with the edge structures are compatible with a poloidal current filament that propagates both in the toroidal and radial direction. Hence the edge structures detected by the GPI are associated with a poloidal current filament.

If the edge turbulence has also a magnetic structure, as pointed out here, the interaction between the DRE and the turbulence should be clearer: in fact there could be some interactions of the type $\mathbf{J} \times \mathbf{B}$ between the magnetic fluctuations of the DRE and the fluctuations in the poloidal current of the edge structures.

A confirmation of the magnetic structure of the edge blobs is obtained with the measurements of the insertable edge probe that can measure the floating potential, electron temperature, density and pressure, and the three components of the magnetic field for low-current discharges ($150 \div 350\,kA$). The conditional average technique is used detecting the intermittent events in the time signal of the electron pressure: the average structures of electron pressure and poloidal current are shown in figure 6.12. This edge probe has a radial array of magnetic probes that allows the direct computation of the current density reported in fig. 6.12: this measure shows that the pressure structures of the plasma edge are associated with a current filament that carries mainly poloidal current. This measure completes the measurements made with the GPI as it gives a value of the current density of the edge filament. A quite similar piece of information can be derived from figure 6.11: the GPI can give the indication that the edge structure is linked with a current filament, even if it can not give the current density itself; but the GPI can give this evidence also at high plasma current.

7

Turbulence in L and H modes in NSTX

7.1 L and H-mode: a short introduction

In this paragraph a short introduction of the L-mode and H-mode of tokamak plasma is given. For a more complete description we refer to some review articles, like [159, 160, 161].

The level of radial particle and energy transport found in tokamaks is mainly caused by small-scale turbulence. Nevertheless, suppression of this turbulence can be observed in specific cases, leading to a reduction of the particle and heat diffusivity in a restricted plasma volume. This behaviour is often called the formation of a *transport barrier*. With the introduction of the divertor, spontaneous formation of a transport barrier at the plasma edge has been found for the first time in the ASDEX tokamak [162] and then in all the other machines. This regime has been named *high confinement* mode ("H-mode"). The effect of the edge transport barrier in electron pressure profile is demonstrated in figure 7.1 for a discharge of ASDEX Upgrade tokamak before and after the transition to H-mode. Here, the presence of the transport barrier at the edge is reflected by the presence of the steep gradient in the electron pressure in the shadowed region. Since the discovery of H-mode, the plasma state before the transition to H-mode is usually termed "L-mode" (*low confinement mode*). In H-mode the pressure gradient steeps up at the plasma edge giving rise to a pressure pedestal, i.e. additional stored energy in the plasma from the pressure offset at the edge. The temperature just inside the transport barrier is significantly higher than in L-mode, allowing (for the same gradient length $L_T = T/\nabla T$) a higher plasma core temperature gradient than in L-mode, resulting in an additional confinement benefit.

While in L-mode additional heating power creates steeper gradients and thus generates more free energy to drive turbulence and enhance losses, it can also trigger a transition to H-mode, a self-organising process that results in a state of reduced transport. This transition to H-mode is accompanied by the creation of a

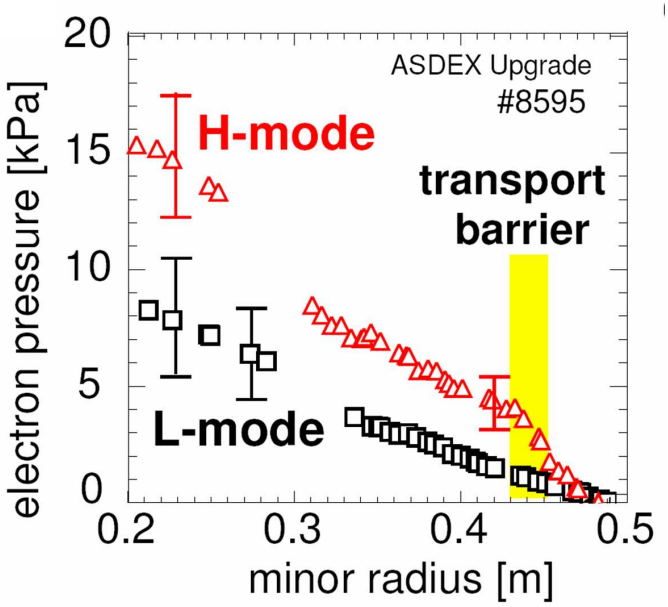

Figure 7.1: *Comparison of electron pressure profile in L-mode and H-mode for the ASDEX-Upgrade tokamak. The formation of the edge transport barrier is clear.*

radial electrical field gradient. It is believed that the de-correlation of turbulence $\mathbf{E} \times \mathbf{B}$ convection cells by sufficient rotation is the origin of the transport reduction (see paragraph 2.9.2 and figure 2.5). However, although a number of possible mechanisms has been proposed, the physics that drives the radial electric field is still unknown and the subject of ongoing research effort.

As the formation of the H-mode is well related to the reduction of the edge fluctuations, it is interesting to study the modification of the edge turbulence in the NSTX tokamak in the transition from L to H-mode. This will be done in the next sections.

7.2 Comparison between L and H-modes

In this section the relation between the edge turbulent structures of NSTX and the two confinement regimes is studied. Therefore, the possible link between the transition from L-mode to H-mode and edge turbulence in tokamak devices has been studied theoretically and experimentally, though it is not completely understood.

The 13 discharges analysed in section 5.6 have a spontaneous transition from L-mode to H-mode captured by the GPI. One example of analysed plasma discharge with the spontaneous transition is shown in figure 7.2.

The plasma current during the flat-top phase is about $800\,kA$, with an injected power by the neutral beam injector of about $2\,MW$. The H-mode increases the plasma performances and the confinement time, reducing the fluctuation level especially in the edge region [110].

A macroscopic effect of the H-mode in the plasma profiles for one of the analysed

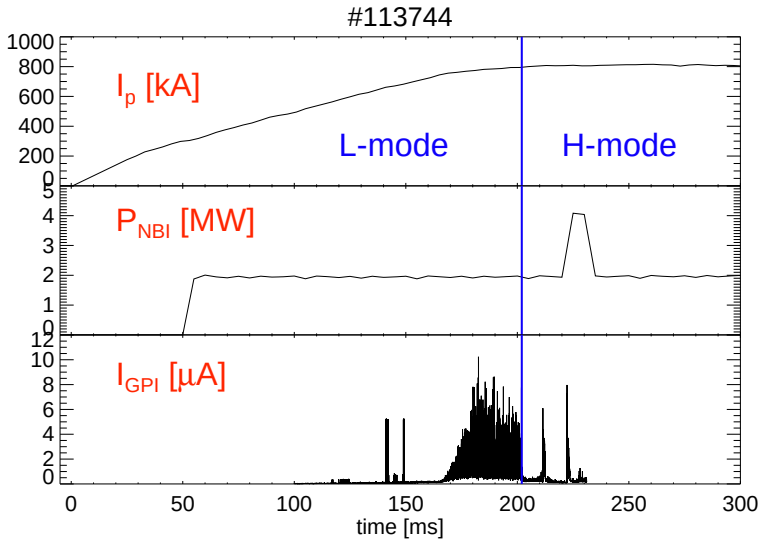

Figure 7.2: *Waveforms of one typical NSTX discharge analysed. Plasma current, NBI power and signal of one GPI chord are reported. The vertical blue line indicates the transition from L to H-mode. The deuterium for the GPI is puffed from* 165 *ms, when the signal increases.*

discharges is reported in fig. 7.3. There is an increase of the electron temperature in the plasma core and the development of a steep electron density gradient in the edge. It is the edge transport barrier previously described.

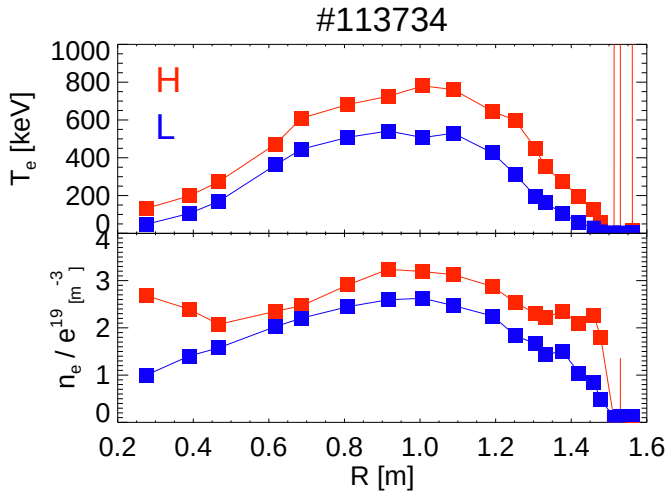

Figure 7.3: *Radial profiles of electron temperature and density in L-mode (blue) and H-mode (red) phase of one NSTX discharge. The profiles are measured with the Thomson scattering diagnostic.*

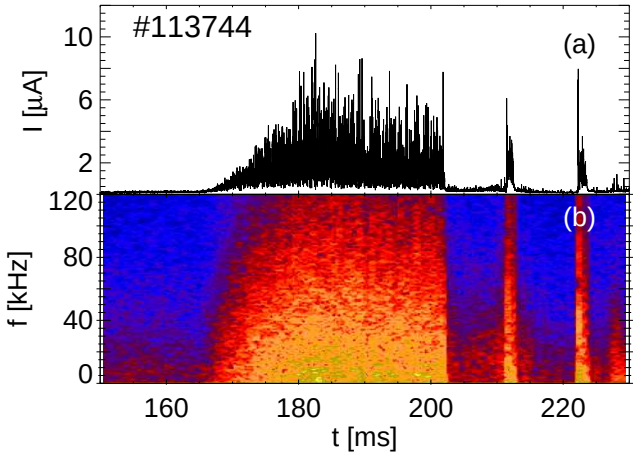

Figure 7.4: *Time behaviour of one chord (P4) of the GPI signal (a) and its spectrogram (b) for NSTX.*

Here we do not want to analyse the global performances of the plasma during the transition, but the attention will be focused on the edge turbulence in the two regimes as measured by the GPI. Only the poloidal array of chords is used, as the most external chords of the radial array have a very low signal (comparable to the noise) probably due to the low electron density that characterises the edge of the H-mode plasmas.

The typical GPI signal during the L-H transition is shown in figure 7.4, together with its spectrogram. When the transition occurs, the edge fluctuations measured by the GPI suddenly drop: the amplitude of the power spectrum decreases, mirroring the lower fluctuation level, and the frequency range of the turbulence is reduced.

From this simple consideration, in the next paragraphs we will study in detail the edge structures, comparing the number of intermittent events in the two regimes and studying the perpendicular $k-$spectrum of the turbulence.

7.2.1 Edge structures

Here the difference in the linear density of edge structures (number of blobs per unit space) between the L-mode and the H-mode is quantified.

Using the poloidal array of GPI chords the linear density of intermittent events (N_s of equation 5.30) is evaluated in the two regimes. Here we assume again that the radial velocity of fluctuations is negligible in the evaluation of the linear density of structures, based on the previous estimate of $v_\theta/v_r \approx 3-5$ for structures near the separatrix both for L and H-mode [71] in NSTX.

In fig. 7.5 (a) the values of N_s at the radial position of the poloidal array of the GPI (about 10-20 mm outside the separatrix position) as a function of the time scale of the structures is reported for the L-mode and the H-mode plasma. Each point is an average over 11 different discharges and the error bars are the rms values. The graph points out that in the higher confinement H-mode phases, the

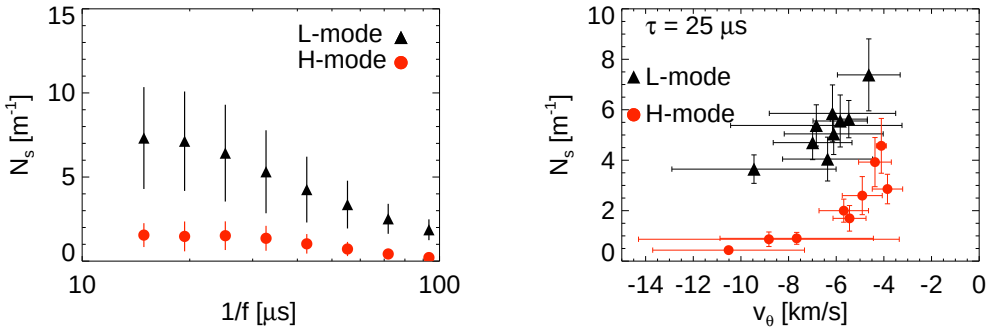

(a) N_s as function of $\tau = 1/f$

(b) N_s as function of v_θ

Figure 7.5: *Linear density of intermittent events for L-mode (black triangles) and H-mode (red circles). (a): linear density of intermittent events as function of the time scale. Each point is an average over different shots. (b): N_s for structures with $\tau = 25\,\mu s$. Each point refers to a different shot of NSTX.*

linear density of bursts is smaller than for the L-mode for all time scales τ.

A complementary piece of information can be gathered from fig. 7.5 (b), where the linear density of structures N_s with $\tau = 25\,\mu s$ is plotted as a function of the poloidal velocity of the fluctuations; each point refers to one shot. Every discharge exhibits a sudden decrease of the linear density of intermittent events in the H-mode phase with respect to the L-mode one, with no significant change in the poloidal velocity.

If these structures are considered to be responsible for most of the anomalous particle transport in the edge of the magnetic confinement devices [98, 114], this measurement indicates that the drop in their density correlates with the presence of the H-mode. Intermittent structures decrease their linear density for all the time scales and this modification seems not to be due only to a variation in v_θ. In fact, fig. 7.5 (b) shows no big difference between the average poloidal velocities in L-mode and H-mode.

7.2.2 Poloidal wavenumber spectrum

The perpendicular wavenumber spectrum is a quantity widely used in plasma turbulence theory to characterise the different space-scales involved in the energy injection and transfer. The GPI allows to obtain the poloidal wavenumber spectrum of the edge turbulence in the L and H-mode. Using two poloidal chords (P4 and P6) spaced by $40\,mm$, the $S(k_\theta, f)$ spectrum has been evaluated (see fig. 5.4) both for the L-mode and H-mode. At first sight the two $S(k_\theta, f)$ are very similar, with a quasilinear dispersion relation. But the integrated spectra show some interesting differences.

By integrating the $S(k_\theta, f)$ spectra in frequency, the normalised power spectra of fluctuations of the poloidal wavenumber k_θ are derived (fig. 7.6).

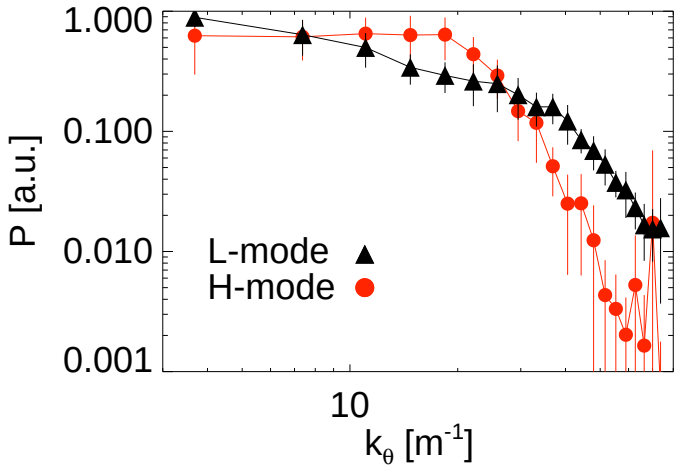

Figure 7.6: *Normalised poloidal wavenumber spectra for L-mode (triangles) and H-mode (circles) phase of the discharge for NSTX.*

For each shot the k_θ spectrum is normalised to its maximum and each point in the figure represents the average over the 11 discharges: the error bars are the rms. The two spectra are quite different: both of them display two separated regions with different power law decays, but the *critical wavenumber* k_θ^* that separates the two regions is different. From the graph, in the L-mode case $k_\theta^* = 40\,m^{-1}$ and in the H-mode $k_\theta^* = 20\,m^{-1}$ Also the decay steepness is different: for $k_\theta > k_\theta^*$ the L-mode decays as $k_\theta^{-3.7}$ and the H-mode as $k_\theta^{-5.5}$ (see table 7.1).

The interpretation of this k-spectrum is not simple. In MHD turbulence theory, the description of the power law decay of the energy spectra refers to the total energy (the sum of the kinetic and magnetic energies [50]) or to density fluctuations, and so it is not easily comparable with the k-spectrum obtained with the GPI. In turbulence theory of non-magnetised fluids, the scale k_θ^* where there is a change in the exponents of the power law decay is related to the injection scale of the energy in the system [36, 163, 164]. Assuming that the same framework remains valid, since the two confinement regimes (L-H) show two different k_θ^*, we can suppose that there are two different injection scales. For the L-mode phase of the discharges,

	L-mode	H-mode
k_θ^*	$40\,m^{-1}$	$20\,m^{-1}$
Decay $k_\theta < k_\theta^*$	$k_\theta^{-0.7\pm0.1}$	$k_\theta^{0.1\pm0.3}$
Decay $k_\theta > k_\theta^*$	$k_\theta^{-3.7\pm0.4}$	$k_\theta^{-5.5\pm0.6}$

Table 7.1: *Summary of the power law decay of the k_θ spectra for L and H mode. k_θ^* can be interpreted as the scale where the energy enters the system; then the different decay exponents in the two ranges of k_θ are outlined. Data from NSTX*

energy enters the system at $k_\theta^* = 40m^{-1}$; as the slopes of the power law are different from 0 for both $k_\theta < k_\theta^*$ and $k_\theta > k_\theta^*$, there may be two cascades with some structures breaking up toward small scales, and some others growing toward the largest scales. Instead, in the H-mode phase, the energy injection is at $k_\theta^* = 20m^{-1}$; then, since for $k_\theta < k_\theta^*$ the k-spectrum does not exhibit a power-law decay, there is no cascade toward the bigger scales, but only toward the smallest ones. With this interpretation, only in the L-mode there is a build up mechanism toward the larger structures; instead in the H-mode the energy injected in the turbulence flows toward higher wavenumber (and so toward small structures) and it is directly coupled with the global plasma flow [165]. Also in Ref. [166] an explanation of the differences in the k spectrum of the potential fluctuations between L and H-mode in the H-1 experiment were interpreted as different cascade process.

These k-spectra are also in qualitative agreement with the spectra calculated for the edge of tokamaks from plasma turbulence theory [167, 143].
As the edge structures are responsible for the greatest part of the edge transport [28, 114], this picture is in agreement with the better confinement properties of the H-mode plasma.

Deeper analysis are needed to compare systematically the H and L modes and to correlate the edge turbulence and transport to this transition. A comparison of these time series statistics with the 2D motion of the structures as detected with the fast camera is needed for gaining further understanding of these phenomena.

The facts all contribute only to setting the problem,
not to its solution.

L. Wittgenstein, Tractatus Logico-Philosophicus

8 Conclusions and future work

8.1 Conclusions

In this PhD thesis the edge turbulence of three magnetically confined fusion plasma devices has been characterised. The turbulence has been studied with the optical diagnostic named GPI, Langmuir probes and magnetic probes in RFX-mod and TPE-RX reversed field pinch experiments and NSTX spherical tokamak.

The GPI diagnostic measures the fluctuations of the light emitted from the neutral gas in the plasma edge, which are correlated to the local electron density and temperature. The simultaneous measurements of the GPI and floating potential or magnetic field fluctuations allow to study the electric and magnetic structure of the edge turbulence and of the coherent blobs. All these diagnostics allow the characterisation of turbulence at high frequency.

The results obtained can be summarised as follow:

- In TPE-RX I have compared the potential and the emissivity structures using the optical diagnostic and an array of Langmuir probes: peaks in emissivity are located at the center of the dipole pattern of potential. This result is confirmed by evaluating the cross-phase between the two signals which assumes the value of $\pi/2$. These results suggest a curvature driven mode as the driving mechanism for the turbulence in TPE-RX.

- The relation between edge turbulence and the profiles of electron pressure has been demonstrated also for the NSTX tokamak. The intermittency level of edge fluctuations increases moving outward, as both Flatness and Skewness increase. Then the area of the edge plasma occupied by blobs is maximum in the radial position where the logarithmic gradient $\nabla p_e/p_e$ of the electron pressure has its minimum. This analysis is compatible with the generation of blobs near the separatrix, where $\nabla p_e/p_e$ is maximum, and their evolution

toward the lower gradient region occupying a larger area of plasma.

- In the NSTX tokamak the edge turbulence has been characterised in the two confinement regimes, the L-mode and the improved confinement H-mode:

  a) The presence of the H-mode is related to a decrease of the edge turbulence: fluctuation levels decrease and in particular I showed the drastic reduction of the linear density of edge blobs which respect to the standard L-mode. The better confinement regime of the H-mode is correlated with the reduction of edge structures that are considered the main cause of anomalous transport in the plasma edge.

  b) Different perpendicular k-spectra have been observed in the two regimes: only in the L-mode there is a build-up mechanism toward the largest structures, which is not observed in the H-mode.

- I have developed for RFX-mod two tomographic algorithms to obtain from the line-integrated signals of the GPI the 2-dimensional pattern of the edge emissivity. In particular the algorithm based on the 2-dimensional Fourier transform allows to reconstruct the edge coherent structures that move in the plasma edge, obtaining a 2D frame every sampling time, i.e. at 10 MHz. This algorithm is also a useful tool for the data analysis, as it is possible to study the time evolution of the edge fluctuation energy and in particular the time evolution of their perpendicular velocity.

- In RFX-mod I characterised the magnetic structure of the edge turbulence. Fluctuations of the emissivity signal and of magnetic field are well correlated, indicating a link between the two phenomena. Then I showed that the edge blobs are associated with current filaments extending along the magnetic field lines (mainly poloidal in the edge of a RFP device). These current filaments interact with the strong magnetic fluctuations of RFX-mod due to the relaxation of the magnetic field, called Dynamo Relaxation Events.

- The universality of the principal statistical and spectral properties of the edge turbulence has been underlined:

  a) Independently from the plasma condition and magnetic equilibria, the power spectra of the GPI fluctuations in RFX-mod, TPE-RX and NSTX show a power-law decay at high frequency, indicating the presence of an energy exchange process between different scales.

  b) With the conditional average technique I characterised the toroidal profile of the intermittent structures in TPE-RX and RFX-mod. The toroidal dimension of these structures varies from 20 to 80 mm and the dimension is linked to the magnetic boundary condition: in RFX-mod with the active control of the radial magnetic field at the plasma edge the toroidal length of the edge structures is about half that of TPE-RX without magnetic boundary control.

c) I have demonstrated that the edge turbulence in all the three devices is not self-similar: the probability density function of the fluctuations at different time scales depends on the scales themselves. This feature detected in the GPI signals has been recovered also in the floating potential signals measured in TPE-RX. The non self-similarity is due to the presence in the plasma edge of coherent structures that are responsible for the greatest part of the anomalous particle transport in the edge.

d) All the Probability Density Functions (PDFs) of the GPI data collected in RFX-mod can be fitted with a linear combination of two Gamma functions: one is related to the uncorrelated background fluctuations, and the other is related to the coherent part of the fluctuations (the blobs). Even if the amount of data collected in TPE-RX and NSTX is smaller than the ones of RFX-mod, also the PDF of the GPI signals of these experiments can be fitted with the same function. This is a signature of a common mechanism that underlies the edge turbulence.

8.2 Open issues

In all the scientific works the end point is the beginning for new research activities. The universality of edge fluctuations could be extended by applying the same analysis to other magnetic confinement devices and to the measurements of Langmuir probes. In fact there are some differences between the statistical properties of the GPI data and similar measurements made with electrostatic probes in different machines [150, 132, 122].

Then the nature of the driving mechanism of the turbulence has to be better characterised: even if the role of the electron pressure gradient as source of energy for the edge turbulence is almost universally accepted, the physical mechanism is not completely clear. New measurements with both the GPI and the electrostatic probes could reveal some useful hints.

In the NSTX tokamak it is possible to compare the results of the GPI with the ones of the fast CCD camera that allows a direct 2-dimensional image of the plasma edge. In particular the area occupied by the blobs can be measured directly by analysing the frames collected by this camera and comparing the results with the linear array of the GPI. This analysis could confirm the two different types of energy cascades detected in L-mode and H-mode by means of the k-spectrum.

In RFX-mod two improvements of the optical diagnostic have just been carried out: on the one hand, a new fan of lines of sight has been recently installed to measure the light emission in sundry radial positions. This new fan should allow a better tomographic reconstruction of the emissivity, and should give a better radial resolution than the old configuration. On the other hand this new fan will be used also to measure the radial profile of electron temperature and density in the plasma edge with a spatial resolution of 5 mm. This new diagnostic will give some information on the role of the radial profile of the electron pressure also in RFX-mod, with a high spatial and temporal resolution, also for high current discharges ($I_p = 1 \div 1.5\,MA$), when electrostatic probes cannot be used. The installation

and the radial alignement have been done, and now the absolute calibration of the system is needed to provide the measurements

Acknowledgments

I have been lucky, very lucky during these three years of PhD, as I could work with nice and clever people, who introduced me through the physics of plasma turbulence and who helped me to solve the various problems met. They made me love this "work". And now they are for me very good friends. Thank you Paolo, Gianluigi, Roberto and Stewart!

I have to thank Paolo Scarin as he explained me the mysteries of the spectroscopy: I spent very interesting (and many, many ...) hours in the dark laboratory with lamps, fiber optics, photomultipliers spectrographs and lenses. I thank him since he read many times this thesis and for the discussions and suggestions received to better it.

Thank to Stewart Zweben, who gave me hospitality for three months at Princeton Plasma Physics Laboratory: it has been for me a honour to work together with the father of the GPI diagnostic. We had stimulating and interesting discussions that helped me to look at physical problems from different points of view.

And what say about Gianluigi Serianni? He is the one with whom I began my research activity with the degree thesis in 2003: if I'm doing this "work" loving it, this is mainly for him. I worked with Gianluigi for four years, and I think I couldn't find a better one for doing it.

Then I sincerely thank Roberto Cavazzana. He is a great brain: I had the most stimulating discussions about physics with him, even if for Roberto everything seemes so simple!! But he is an inexhaustible source of ideas (sometimes very strange).

These are the four people I want to thank more: they have very different characters, but they are complementary and they helped me to grow up.

During the PhD, in a big laboratory as RFX, I discussed and interacted with many other people: and so I want to thank Nicola Vianello (I'm a little envious of him as his works are, according to me, one of the best in the plasma edge turbulence), Fabio Sattin (I think he knows almost everything about physics since he can answer clearly to almost every question...), Monica Spolaore (I regret to have worked too less with her) and Vanni Antoni for the suggestion abou how to face the writing of a thesis. The discussions made together (also along the corridors and at the coffee machine) stimulated me with new ideas helpful for this thesis.

And before the end of the thesis, I want to thank my traveling companion: we shared these three years, with all the troubles but with many great moments. Thank you to Marco, Fulvio, Cristiano (a kiss to Claudia and one to Anna, their beautiful daughter) and Federica (who standed us and our jokes, especially during the period of thesis writing). They helped me to spend the long days and long afternoons in the office writing this thesis and preparing conferences. I thank them also because without the dinners, coffee-breaks, holidays spent together, these years should have been certainly too much boring.

Thank also to the reader of my thesis, hoping his judgment is not too bad.

M.A.

Bibliography

[1] J. Wesson, *Tokamaks*, Clarendon Press, 1987.

[2] J. Sheffield, Rev. Mod. Phys. **66**, 1015 (1994).

[3] E. Rebhan and G. V. Oost, Fusion Sci. Technol. **45**, S15 (2004).

[4] B. Carreras, IEEE Tran. Plasma Sci. **25**, 1281 (1997).

[5] J. Freidberg, Rev. Mod. Phys. **54**, 801 (1982).

[6] J. Jacquinot and the JET team, Plasma Phys. Controlled Fusion **41**, A13 (1999).

[7] D. V. Houtte et al., Nucl. Fusion **44**, L11 (2004).

[8] H. Zushi et al., Nucl. Fusion **43**, 1600 (2003).

[9] M. Shimada et al., Nucl. Fusion **47**, S1 (2007).

[10] J. Freidberg, *Ideal Magneto-Hydro-Dynamics*, Plenum Press, New York, 1987.

[11] R. Goldstone and P. Rutherford, *Plasma Physics*, Institute of Physics Publishing, London, 2000.

[12] S. Ortolani and D. Schnack, *Magnetohydrodynamic of Plasma Relaxation*, World Scientific, Singapore, 1993.

[13] G. Rostagni, Fusion Eng. Design **25**, 301 (1995).

[14] P. Sonato et al., Fusion Eng. Design **66-68**, 161 (2003).

[15] S. Martini et al., Nucl. Fusion **47**, 783 (2007).

[16] T. Bolzonella, N. Pomaro, G. Serianni, and D. Marcuzzi, Rev. Sci. Instrum. **74**, 1554 (2003).

[17] G. Serianni, W. Baker, and S. D. Bello, Rev. Sci. Instrum. **74**, 1558 (2003).

[18] Y. Yagi et al., Fusion Eng. Design **45**, 421 (1999).

[19] Y. Yagi et al., Plasma Phys. Controlled Fusion **41**, 255 (1999).

[20] C. Neumeyer et al., Fusion Eng. Design **54**, 275 (2001).

[21] V. Gusev, F. Alladio, and A. Morris, Plasma Phys. Controlled Fusion **45**, A59 (2003).

[22] G.E.Menard et al., Nucl. Fusion **47**, S645 (2007).

[23] V. Antoni, Plasma Phys. Controlled Fusion **39**, B223 (1997).

[24] V. Antoni, D. Desideri, E. Martines, G. Serianni, and L. Tramontin, Phys. Rev. Lett. **79**, 4814 (1997).

[25] K. Burrell, Phys. Plasmas **4**, 1499 (1997).

[26] M. Pedrosa et al., Plasma Phys. Controlled Fusion **47**, 777 (2005).

[27] R. Cavazzana, G. Serianni, P. Scarin, M. Agostini and et al., Plasma Phys. Controlled Fusion **49**, 129 (2007).

[28] V. Antoni et al., Phys. Rev. Lett. **87**, 045001 (2001).

[29] M. Endler, J. Nucl. Mater. **266-269**, 84 (1999).

[30] W. Vinen and R. Donnelly, Phys. Today **60**, 43 (2007).

[31] V. Carbone et al., Rivista del Nuovo Cimento **27**, 1 (2004).

[32] R. Bruno and V. Carbone, Living Rev. Solar Phys. **2**, 1 (2005).

[33] U. Frisch, *Turbulence*, Cambridge University Press, 1995.

[34] K. Sreenivasan, Rev. Mod. Phys. **71**, S383 (1999).

[35] A. Wotton et al., Phys. Fluids B **2**, 2879 (1990).

[36] M. Lesieur, *Turbulence in Fluids*, Kluwer Academic Press, 1997.

[37] J. Krommes, Phys. Rep. **360**, 1 (2002).

[38] M. Verma, Phys. Rep. **401**, 229 (2004).

[39] W. McComb, *The Physics of Fluid Turbulence*, Clarendon Press Oxford, 1992.

[40] L. Richardson, *Weather Prediction by Numerical Process*, Cambridge University Press, 1922.

[41] L. Richardson, Proc. R. Soc. Lond. A **110**, 709 (1926).

[42] A. Kolmogorov, Acad. Sci. URSS (NS) **30**, 301 (1941).

[43] A. Kolmogorov, Acad. Sci. URSS (NS) **31**, 538 (1941).

[44] L. Landau and E. Lifshitz, *Fluids Mechanics*, Pergamon Press, 1987.

[45] K. Huang, *Statistichal Mechanics*, John Wiley and Sons, 1987.

[46] K. Wilson and J. Kogut, Phys. Rep. C **12**, 75 (1974).

[47] K. Wilson, Rev. Mod. Pys **3**, 583 (1983).

[48] D. Forster, D. Nelson, and M. Stephen, Phys. Rev. A **16**, 732 (1977).

[49] W. Elsässer, Phys. Rev. Lett **79**, 183 (1950).

[50] D. Biskamp, *Magnetohydrodynamic Turbulence*, Cambridge University Press, 2003.

[51] M. Dobrowonly, A. Mangey, and P. Veltri, Phys. Rev. Lett **45**, 144 (1980).

[52] P. Iroshnikov, Astron. Zh. **40**, 742 (1963).

[53] R. Kraichnan, Phys. Fluids **8**, 1385 (1965).

[54] A. Kolmogorov, Acad. Sci. URSS (NS) **32**, 16 (1941).

[55] L. Sorriso-Valvo, V. Carbone, G. Consolini, R. Bruno, and P. Veltri, Geophys. Res. Lett. **13**, 1801 (1999).

[56] V. Carbone et al., Europhys. Lett. **58**, 349 (2002).

[57] A. Hasegawa and K. Mima, Phys. Fluids **12**, 87 (1978).

[58] A. Yoshizawa, S. Itoh, K. Itoh, and N. Yokoi, Plasma Phys. Controlled Fusion **43**, R1 (2001).

[59] G. Boffetta, F. D. Lillo, and S. Musacchio, Europhys. Lett. **12**, 687 (2002).

[60] V. Antoni et al., Plasma Phys. Control. Fusion **47**, B13 (2005).

[61] B. Scott, Phys. Plasmas **7**, 1845 (2000).

[62] P. Terry, Rev. Mod. Phys. **72**, 109 (2000).

[63] H. Biglari, P. Diamond, and P. Terry, Phys. Fluids B **2**, 1 (1990).

[64] G. Serianni, M. Agostini et al., Plasma Phys. Controlled Fusion **49**, B267 (2007).

[65] D. Stotler, B. LaBombard, J. Terry, and S. Zweben, J. Nucl. Mater **313-316**, 1066 (2003).

[66] D. Stotler et al., Contrib. Plasma Phys. **44**, 294 (2004).

[67] S. Zweben, J. McChesney, and R. Gould, Nucl. Fusion **23**, 825 (1983).

[68] S. Zweben et al., J. Nucl. Mater. **145-147**, 250 (1987).

[69] S. Zweben and S. Madley, Phys. Fluids B **1**, 2058 (1989).

[70] R. Maqueda and G. Wurden, Nucl. Fusion **39**, 629 (1999).

[71] S. Zweben et al., Nucl. Fusion **44**, 134 (2004).

[72] S. Zweben et al., Phys. Plasmas **13**, 056114 (2006).

[73] J. Terry et al., Rev. Sci. Instrum. **75**, 4196 (2004).

[74] R. Maqueda et al., J. Nucl. Mater. **363-365**, 1000 (2007).

[75] J. Alonso et al., Plasma Phys. Controlled Fusion **48**, B465 (2006).

[76] G. Antar, J. Yu, and G. Tynan, Phys. Plasmas **14**, 022301 (2007).

[77] R. Cavazzana, P. Scarin, G. Serianni, M. Agostini and et al., Rev. Sci. Instrum. **75**, 4152 (2004).

[78] M. Zuin, M. Agostini et al., Il Nuovo Cimento C **27**, 449 (2004).

[79] M. Agostini, R. Cavazzana, P. Scarin, and G. Serianni, Rev. Sci. Instrum. **77**, 10E513 (2006).

[80] R. Maqueda et al., Rev. Sci. Instrum. **74**, 2020 (2003).

[81] B. Schweer, G. Mank, and A. Pospieszcyk, J. Nucl. Mater. **196-198**, 174 (1992).

[82] B. Schweer, M. Brix, and M. Lehnen, J. Nucl. Mater. **266-269**, 673 (1999).

[83] L. Carraro, M. Puiatti, F. Sattin, P. Scarin, and M. Valisa, Rev. Sci. Instrum. **72**, 967 (2001).

[84] L. Carraro et al., Plasma Phys. Controlled Fusion **42**, 1 (2000).

[85] M. Brix and B. Schweer, 24^{th} EPS Conference on Plasma Physics, ECE **4**, 1837 (1997, Berchtesgaden , Germany).

[86] G. Jenkis and D. Watts, *Spectral Anlaysis and Its Applications*, Holden-Day, San Francisco, 1969.

[87] S. Mallat, *A Wavelet Tour of Signal Processing*, Academic Press, London, 1998.

[88] M. Farge, Annu. Rev. Fluid Mech. **24**, 395 (1992).

[89] J. Beall, Y. Kim, and E. Powers, J. Appl. Phys. **53**, 3933 (1982).

[90] S. Levinson, J. Beall, E. Powers, and R. Bengstone, Nucl. Fusion **24**, 527 (1984).

[91] C. Torrence and G. Compo, Bull. Am. Meteorol. Soc. **79**, 61 (1998).

[92] R. Maqueda et al., Rev. Sci. Instrum. **72**, 931 (2001).

[93] S. Zweben et al., Phys. Plasmas **9**, 1981 (2002).

[94] G. Serianni, M. Agostini, R. Cavazzana, and P. Scarin, Plasma Phys. Controlled Fusion **49**, 2075 (2007).

[95] G. Serianni, R. Cavazzana, M. Agostini, and P. Scarin, Plasma and Fusion Research **2**, S1119 (2007).

[96] T. Munsat and S. Zweben, Rev. Sci. Instrum. **77**, 103501 (2006).

[97] F. Natterer, *The mathematics of computerized tomography*, Teubner, Stuttgard, 1986.

[98] M. Spolaore et al., Phys. Rev. Lett. **93**, 215003 (2004).

[99] P. Scarin, M. Agostini, R. Cavazzana, F. Sattin, G. Serianni, N. Vianello, J. Nucl. Mater. **363-365**, 669 (2007).

[100] P. Hansen, SIAM J. Sci. Statist. Comput. **11**, 503 (1990).

[101] P. Hansen, SIAM J. Sci. Statist. Comput. **13**, 1142 (1992).

[102] T. D. de Witt, Plasma Phys. Controlled Fusion **37**, 117 (1994).

[103] P. Hansen, SIAM Review **34**, 561 (1992).

[104] P. Hansen and D. O'Leary, SIAM J. Sci. Statist. Comput. **14**, 1487 (1993).

[105] G. Spizzo, *Thermal Properties of Improved Confinament Regimes in RFX*, PhD thesis, University of Padova, Italy, 2000.

[106] P. Franz, L. Marrelli, A. Murari, G. Spizzo, and P. Martin, Nucl. Fusion **41**, 695 (2001).

[107] L. Carraro et al., J. Nucl. Mater. **313-316**, 976 (2003).

[108] R. Cavazzana, P. Scarin, G. Serianni, M. Agostini, and N. Vianello, 32^{nd} EPS Conference on Plasma Physics, ECE **29C**, P1.073 (27 June - 1 July 2005, Tarragona, Spain).

[109] B. Carreras et al., Phys. Plasmas **6**, 4615 (1999).

[110] R. Maingi et al., Nucl. Fusion **43**, 969 (2003).

[111] M. Greenwald et al., Nucl. Fusion **28**, 2199 (1988).

[112] M. Greenwald, Plasma Phys. Controlled Fusion **44**, R27 (2002).

[113] G. Antar, G. Counsell, and J. Ahn, Phys. Plasmas **12**, 082503 (2005).

[114] M. Endler et al., Nucl. Fusion **35**, 1307 (1995).

[115] J. Bleuel et al., New. J. Phys. **4**, 38.1 (2002).

[116] G. Serianni et al., 33^{rd} EPS Conference on Plasma Physics, ECE **30I**, P5.096 (19-23 June 2006, Rome , Italy).

[117] G. Antar, G. Counsell, Y. Yu, B. LaBombard, and P. Devynck, Phys. Plasmas **10**, 419 (2003).

[118] B. van Milligen et al., Phys. Plasmas **12**, 052507 (2005).

[119] J. Graves, J. Horacek, R. Pitts, and K. Hopcraft, Plasma Phys. Controlled Fusion **47**, L1 (2005).

[120] M. Agostini et al., Phys. Plasmas **14**, 102305 (2007).

[121] F. Sattin, P. Scarin, M. Agostini, R. Cavazzana, G. Serianni, M. Spolaore, N. Vianello, Plasma Phys. Controlled Fusion **48**, 1033 (2006).

[122] B. Labit et al., Phys. Rev. Lett. **98**, 255002 (2007).

[123] R. Jha et al., Phys. Rev. Lett. **69**, 1375 (1992).

[124] N. Vianello, *Fenomeni di auto organizzazione e generazione di strutture coerenti indotte da turbolenza elettrostatica in plasmi magnetizzati*, PhD thesis, University of Padova, Italy, 2002.

[125] N. Vianello et al., Plasma Phys. Controlled Fusion **44**, 2513 (2002).

[126] A. Carbone, L. Sorriso-Valvo, E. Martines, V. Antoni, and P. Veltri, Phys. Rev. E **62**, R49 (2000).

[127] M. Farge, K. Schneider, and P. Devynck, Phys. Plasmas **13**, 042304 (2006).

[128] M. Onorato, R. Camussi, and R. Iuso, Phys. Rev. E **61**, 1447 (2000).

[129] V. Antoni et al., Europhys. Lett. **54**, 51 (2001).

[130] P. Devynck, P. Ghendrih, and Y. Sarazin, Phys. Plasmas **12**, 050702 (2005).

[131] G. Antar et al., Phys. Rev. Lett. **87**, 065001 (2001).

[132] T. Carter, Phys. Plasmas **13**, 010701 (2006).

[133] A. Fasoli et al., Phys. Plasmas **13**, 055902 (2006).

[134] T. Windisch, O. Grulke, and T. Klinger, Phys. Plasmas **13**, 122303 (2006).

[135] N. Vianello, private communication, 2007.

[136] O. Grulke, T. Klinger, M. Endler, A. Piel, and the W7-AS Team, Phys. Plasmas **8**, 5171 (2001).

[137] E. Martines et al., Czech. J. Phys. **52**, D13 (2002).

[138] V. Antoni et al., Contr. Plasma Phys. **44**, 458 (2004).

[139] O. Grulke, J. Terry, B. LaBombard, and S. Zweben, Phys. Plasmas **13**, 012306 (2006).

[140] I. Teliban, D. Block, A. Piel, and F. Greiner, Plasma Phys. Controlled Fusion **49**, 485 (2007).

[141] L. Marrelli and The RFX-mod Team, Plasma Phys. Controlled Fusion **49**, B359 (2007).

[142] E. Martines, V. Antoni, D. Desideri, S. Serianni, and L. Tramontin, Nucl. Fusion **39**, 581 (1999).

[143] B. Scott, Phys. Plasmas **12**, 062314 (2005).

[144] C. Lechte, S. Niedner, and U. Stroth, New. J. Phys. **4**, 34.1 (2002).

[145] O. Grulke, S. Ullrich, T. Windisch, and T. Klinger, Plasma Phys. Controlled Fusion **49**, B247 (2007).

[146] O. E. Garcia et al., Plasma Phys. Controlled Fusion **48**, L1 (2006).

[147] O. Grulke and T. Klinger, New. J. Phys. **4**, 67.1 (2002).

[148] B. LeBlanc et al., Rev. Sci. Instrum. **74**, 1659 (2003).

[149] B. Carreras, V. Lynch, and B. LaBombard, Phys. Plasmas **8**, 3702 (2001).

[150] J. Boedo et al., Phys. Plasmas **10**, 1670 (2003).

[151] J. Boedo et al., Phys. Plasmas **8**, 4826 (2001).

[152] P. Devynck et al., Phys. Plasmas **13**, 102505 (2006).

[153] J. Myra et al., Phys. Plasmas **13**, 092509 (2006).

[154] H. Park et al., Phys. Plasmas **13**, 055907 (2006).

[155] G. Serianni et al., Rev. Sci. Instrum. **75**, 4338 (2004).

[156] M. Zuin et al., 34^{th} EPS Conference on Plasma Physics, ECE **31I**, P1.118 (2-6 July 2007, Warsaw , Poland).

[157] J. Myra, Phys. Plasmas **14**, 102314 (2007).

[158] M. Spolaore et al., 33^{rd} EPS Conference on Plasma Physics, ECE **30I**, P5.097 (19-23 June 2006, Rome , Italy).

[159] J. Connor and H. R. Wilson, Plasma Phys. Controlled Fusion **42**, R1 (2000).

[160] E. Doyle et al., Nucl. Fusion **47**, S18 (2007).

[161] F. Wagner, Plasma Phys. Controlled Fusion **49**, B1 (2007).

[162] F. Wagner et al., Phys. Rev. Lett. **49**, 1408 (1982).

[163] E. Gkioulekas and K. Tung, Discrete Contin. Dyn. Syst. Ser. B **5**, 79 (2005).

[164] E. Gkioulekas and K. Tung, Discrete Contin. Dyn. Syst. Ser. B **5**, 103 (2005).

[165] A. Dyachenko, S. Nazarenko, and V. Zakharov, Phys. Lett. A **165**, 330 (1992).

[166] M. Shats, H. Xia, and H. Punzmann, Phys. Rev. E **71**, 046409 (2005).

[167] J. Terry et al., Phys. Plasmas **10**, 1739 (2003).